

INFORMATION TO USERS

This manuscript has been reproduced from the microfilm master. UMI films the text directly from the original or copy submitted. Thus, some thesis and dissertation copies are in typewriter face, while others may be from any type of computer printer.

The quality of this reproduction is dependent upon the quality of the copy submitted. Broken or indistinct print, colored or poor quality illustrations and photographs, print bleedthrough, substandard margins, and improper alignment can adversely affect reproduction.

In the unlikely event that the author did not send UMI a complete manuscript and there are missing pages, these will be noted. Also, if unauthorized copyright material had to be removed, a note will indicate the deletion.

Oversize materials (e.g., maps, drawings, charts) are reproduced by sectioning the original, beginning at the upper left-hand corner and continuing from left to right in equal sections with small overlaps.

Photographs included in the original manuscript have been reproduced xerographically in this copy. Higher quality 6" x 9" black and white photographic prints are available for any photographs or illustrations appearing in this copy for an additional charge. Contact UMI directly to order.

ProQuest Information and Learning
300 North Zeeb Road, Ann Arbor, MI 48106-1346 USA
800-521-0600

UMI[®]

University of Alberta

**A Modification to Rutherford Scattering Theory in a
High Intensity, Laser Heated Plasma**

by

Charles J. Kirkby ©

A thesis submitted to the Faculty of Graduate Studies and Research in partial
fulfillment of the requirements for the degree of Master of Science

Department of Physics

Edmonton, Alberta

Fall 2000



National Library
of Canada

Acquisitions and
Bibliographic Services

395 Wellington Street
Ottawa ON K1A 0N4
Canada

Bibliothèque nationale
du Canada

Acquisitions et
services bibliographiques

395, rue Wellington
Ottawa ON K1A 0N4
Canada

Your file *Votre référence*

Our file *Notre référence*

The author has granted a non-exclusive licence allowing the National Library of Canada to reproduce, loan, distribute or sell copies of this thesis in microform, paper or electronic formats.

The author retains ownership of the copyright in this thesis. Neither the thesis nor substantial extracts from it may be printed or otherwise reproduced without the author's permission.

L'auteur a accordé une licence non exclusive permettant à la Bibliothèque nationale du Canada de reproduire, prêter, distribuer ou vendre des copies de cette thèse sous la forme de microfiche/film, de reproduction sur papier ou sur format électronique.

L'auteur conserve la propriété du droit d'auteur qui protège cette thèse. Ni la thèse ni des extraits substantiels de celle-ci ne doivent être imprimés ou autrement reproduits sans son autorisation.

0-612-59825-X

Canada

University of Alberta

Library Release Form

NAME OF AUTHOR: Charles J. Kirkby

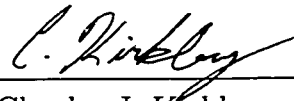
TITLE OF THESIS: A Modification to Rutherford Scattering Theory in a High Intensity, Laser Heated Plasma

DEGREE: Master of Science

YEAR THIS DEGREE GRANTED: 2000

Permission is hereby granted to the University of Alberta Library to reproduce single copies of this thesis and to lend or sell such copies for private, scholarly or scientific research purposes only.

The author reserves all other publication and other rights in association with the copyright in the thesis, and except as hereinbefore provided neither the thesis nor any substantial portion thereof may be printed or otherwise reproduced in any material form whatever without the author's prior written permission.



Charles J. Kirkby
741 Ascot Ave.
Oshawa Ontario L1G 1X3
CANADA

Sept. 28, 2000

If possible, try to find a way to come downstairs that doesn't involve going bump, bump, bump on the back of your head.

A.A. Milne from *Pooh's Little Instruction Book*

Abstract

The effect of an intense laser field on the Rutherford scattering problem and its relation to the inverse bremsstrahlung heating of the electron distribution function in a plasma is examined. A study of the dissipation of particle velocity by elastic collisions yields a modification to the differential transport cross section in the high intensity regime. Also an investigation of inelastic collisions reveals a modification to the inverse bremsstrahlung heating rate. A kinetic particle code is developed and the modified transport cross section is incorporated into the scattering algorithm.

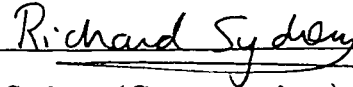
University of Alberta

Faculty of Graduate Studies and Research

The undersigned certify that they have read, and recommend to the Faculty of Graduate Studies and Research for acceptance, a thesis entitled **A Modification to Rutherford Scattering Theory in a High Intensity, Laser Heated Plasma** submitted by **Charles J. Kirkby** in partial fulfillment of the requirements for the degree of Master of Science.



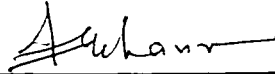
W. Rozmus (Supervisor)



R. Sydora (Co-supervisor)



C. Capjack (External)



F. Khanna (Member)

DATE: *Sept 8, 2000*

To

To Nick and Luke

Acknowledgements

I would like to thank my supervisors Wojciech Rozmus and Richard Sydora for the opportunity to conduct this project, and for their guidance and efforts through all aspects of its development.

A special thanks goes to Eugene Fourkal for his efforts in this study, many hours of discussion and insight. I would like to thank Andrei Maximov as well for his advice and guidance. Also I thank the members of the laser plasma group at the Theoretical Physics Institute, as well as the members of my thesis committee.

I would like to thank all of my friends and colleagues for their support. And finally I thank my family for putting up with me living so far away to pursue my goals.

Table of Contents

Abstract

Acknowledgements

Table of Contents

List of Tables

List of Figures

1	Introduction	1
1.1	Boltzmann Equation	2
1.2	The Landau Collision Operator	8
1.3	The Rutherford Cross Section	14
2	Microscopic Electron-Ion Collisions	16
2.1	Background	16
2.3	The Algorithm	20
2.4	Testing the Classical Results	21
2.5	Individual Collisions	23
2.6	Chaotic Scattering	27

TABLE OF CONTENTS

3	Transport Cross Section	30
3.1	Determining the Transport Cross Section	30
3.2	The Case of the Parallel Launch	34
3.3	The Case of the Perpendicular Launch	39
3.4	Large Angle Contribution	45
3.5	Transport Cross Section	46
4	Effective Cross Section	55
4.1	Energy Conservation	55
4.2	Inverse Bremsstrahlung Heating	57
4.3	Results	59
4.3.1	Effective Cross Section Modification	64
4.3.2	Modification to the IB Heating Rate	68
5	The Particle-Simulation Model	72
5.1	Introduction	72
5.2	Model	73
5.2.1	Pairing the Particles	74
5.2.2	Details of the Collision	77
5.2.3	Changes in Velocity	82
5.3	General Results of Standard Tests	84
5.3.1	Drift Velocity Slowing	84
5.3.2	Thermal Isotropization	86
5.3.3	Temperature Relaxation	88
5.3.4	Entropy	89
5.4	Notes on the Parallel Set Up	91
5.5	Heating Runs	93
6	Summary and Conclusions	98

List of Tables

3.1	The coefficients found that gave the best fit approximation to the curve transport cross section curve.	50
4.1	This table indicates the different parameters examined for the effective cross section, and the associated values for $g(u)$ after averaging the results over a Maxwellian distribution for the $T = 100$ eV case. Note the increase in $g(u)$ above unity.	69
4.2	The results averaged over Maxwellians with $T = 80$ and 200 eV. .	70
5.1	This table demonstrates the technique used to randomly order the particles in in a particular cell. The actual numbers used are the identification numbers of the particles in the entire system and for simplicity they are aligned in ascending numerical order on the left. The right columns correspond to their positions after the randomization process. The particles are then paired with their horizontal neighbours. Note that there is a good possibility that there will be an unequal total number of particles from each species.	76

List of Figures

1.1	A sketch of a two body collision. The interaction sphere is defined at a radius R_c , the cutoff range of the potential.	3
1.2	A sketch of a collision in the centre of mass frame. The incident particle approaches with velocity \vec{g} and is elastically scattered by interaction with the potential $V(r)$, resulting in a final velocity of $g\vec{e}$, at an angle χ to \vec{g}	5
1.3	An annulus beam of incident particles with uniform initial velocity at a specific impact parameter ρ will scatter into the angle χ in time Δt	6
2.1	The conformation of the output of the simulation to the analytical expression in equation 2.21 is a clear demonstration of the accuracy of the algorithm.	22
2.2	An example of small angle scattering for an electron launched with an initial velocity of v_E and an impact parameter of $2r_E$ inside an electric field oriented along the z axis, parallel to the initial drift velocity. The Rutherford trajectory is superimposed under the trajectory in the presence of the external field. Most analytical work assumes that such trajectories dominate the collisions. Note the reduction of the scattering angle in the presence of the field. .	24

LIST OF FIGURES

2.3	The same collision as shown in projection in figure 2.2. The axes have been rotated as to give the best qualitative picture possible and illustrate the end path difference for the case including the field.	25
2.4	An example of trapping under conditions similar to those in Fig.(2.2). The external laser field as been oriented parallel to the launch direction (along the z axis). Note the chaotic orbit of the electron before it finally escapes into the fourth quadrant (inset).	26
2.5	An example of correlated collisions where the external field is again oriented parallel to the launch velocity, along the z axis. This effect naturally becomes more important as the strength of the field is increased which is why we illustrate here the $\Omega = 0.5$ case. For an impact parameter of $5r_E$ and initial velocity of v_E we can see a significant deviation of the trajectory for a system exposed to the field.	27
2.6	An example of the sensitivity of the final scattering angle to the initial phase of the laser field. 240 launches were performed with the parameters: $\nu = 0.5$, $\Omega = 0.3$, and impact parameter $\rho = 0.2$. Orientations of the laser field both parallel and perpendicular to the incident launch velocity are depicted. Notice that there are regions where the scattering angle is reasonably stable, and regions where it is chaotic.	28
3.1	This figure illustrates the coordinate system used, as well as the concept of the launching grid. In general the diagram is not to perfect scale. The ion interaction sphere is defined by a Debye length as its radius.	31
3.2	The resulting transport cross section for parallel launching schemes and the no field case.	36

LIST OF FIGURES

- 3.3 An example of how our simulation conformed to Shvets' analytical result in 3.16. There are deviations of up to 50 percent. 37
- 3.4 A decrease in the transport cross section when the dipole field is aligned perpendicular to the initial launch velocity. Note that this is in contrast with the increase observed about v_{osc} for the parallel launch case. This figure depicts trials with the dimensionless frequency set at $\Omega = 0.3$ 40
- 3.5 This graph illustrates an example of the observed average scattering angle as a function of impact parameter for a field orientation similar to that discussed in figure 2.2. This particular case considered only particles with an incident drift velocity of v_E . Note how the simple assumption of the modified impact parameter greatly reduces the predicted scattering angle. 42
- 3.6 This is an example of an event where the amplitude of oscillation (defined by $\Omega = 0.3$ is greater than the impact parameter itself at $5r_E$. Thus for specific initial phases of the field, there is a significant probability that the electron will only experience a minimal deflection, effectively "missing" the ion. 43
- 3.7 Just as the oscillations from the field can cause the electron to miss the ion, the case also exists where the electron can be thrust straight towards the ion. The parameters here are exactly the same as those outlined for figure 3.6 with the field offset by $\pi/2$ 45

LIST OF FIGURES

3.8	The transport cross section as calculated for a parallel launch (above) and where the field is oriented at an angle of $\frac{3\pi}{10}$ (below). The contribution from large angle electrons is given by the solid lines. For velocities lower than ν_{osc} ($4\nu_E$ in these examples) the large angle electrons make a significant contribution to the transport cross section. The significance is strongest in the parallel launch case.	47
3.9	A series of curves plotting the transport cross section as a function of velocity. Recall that our dimensionless frequency Ω is defined such that intensity goes to infinity as Ω goes to zero. Thus it is apparent that there is a decrease in the transport cross section for increasing laser intensity.	48
3.10	Fit for the $\Omega = 0.5$ run.	52
3.11	Fit for the $\Omega = 0.3$ run.	52
3.12	Fit for the $\Omega = 0.25$ run.	53
3.13	Fit for the $\Omega = 0.2$ run.	53
3.14	Fit for the $\Omega = 0.1$ run.	54
4.1	The result of a run where the laser field was turned off and the energy difference before and after the collision was measured over the velocity range we investigated. The increasing fluctuations with velocity are due to the relatively large, time step assumed in the algorithm. The velocities in each case are normalized to v_E which set small enough that the effects of the field are inconsequential. .	57

LIST OF FIGURES

4.2	As the angle between the drift launch velocity and the polarized field increases from the parallel launch condition, a negative energy gain region is observed for small values of the angle confirming the reports of Fraiman <i>et al.</i> [12]. This negative region was generally observed as v approached v_{osc}	60
4.3	The resulting effective cross section for a run with $\Omega = 2.0$	61
4.4	The results of the effective cross section investigation for increasing field intensities. The dotted line represents $\sigma_{eff,L}$. As can be seen there is an obvious decrease in the energy gain as the dimensionless frequency Ω (and thus intensity) is increased for low velocities. . .	63
4.5	An example of a Maxwellian velocity distribution for a $T = 100\text{eV}$ plasma as it changes in our intensity dependent velocity range. . .	64
4.6	$\Omega = 0.5$ run curve fit.	66
4.7	$\Omega = 0.3$ run curve fit.	66
4.8	$\Omega = 0.2$ run curve fit.	67
4.9	The results for $g(u)$ plotted against a simple approximation.	70
5.1	This sketch illustrates the Lorentz model rotation of the total velocity vector in velocity space as a result of the collision between the electron and ion. The polar angle ϕ obeys a uniform distribution whereas the scattering angle θ is restricted to a Gaussian distribution.	78
5.2	This figure is an example of the velocity relaxation for a shifted Maxwellian initial distribution. This particular run looked at an initial parameter of ϵ/T_{e0} of 0.5, with a collision frequency $\nu_0 = 0.05$. The system was run until the drift velocity reached $1/e^3$ of its initial value. The resulting curve conforms well to the expected logarithmic decay.	85

LIST OF FIGURES

5.3 Slowing tests were performed for $x = 0.5$ through 1.5 using both collision frequencies of 0.05 and $0.005 \omega_{pe}$. The resulting points came within six percent at maximum of the analytical result. . . . 86

5.4 In this run the code was initialized with $T_{\parallel}/T_{\perp} = 2$. Again we examined the run for 51200 particles at a collision frequency of $\nu_0 = 0.05 \omega_{pe}$. The curve came within five percent of the analytical prediction. 87

5.5 This graph illustrates a typical 5120 particle run where the initial temperatures were established such that $T_{e0}/T_{i0} = 2$. Again the result conformed well to the analytical prediction for ν_{ei} with a deviation of only six percent. 89

5.6 This figure depicts the x direction velocity distribution evolving from its initial state where all particles were issued a velocity equivalent to the thermal velocity down to a roughly Maxwellian distribution. The entropy in this case should increase until the system comes into equilibrium where it should level off to an approximately constant value. 90

5.7 The entropy in units of k_B for both electrons, ions and the total of the system is plotted against time as the system is allowed to evolve from a constant velocity distribution to a rough Maxwellian as depicted above. The change in entropy over time is always positive and very quickly reaches a constant state in this 51200 particle test run. 91

LIST OF FIGURES

5.8 Evolution of the electron temperature over time due to IB heating. The laser intensity is defined by the parameter $v_{osc}/v_{th}(0) = 1.2$ (graph a) and 12.0 (graph b). Both graphs show curves with the modified transport cross section (1) and the original Rutherford cross section (2) implementing in the scattering algorithm. The inset graph presents the initial heating rate as depicted by the dashed tangent line, which significantly exceeds the usual one. 96

5.9 The electron distribution function at $t\omega_{pe} = 100$, for $v_{osc}/v_{th} = 0.17$ (graph a) and 12.0 (graph b). Again the curve 1 on each graph represents the function obtained with the modified cross section while curve 2 displays the classical form. It is apparent that very quickly after the laser is turned on, the modified algorithm shows a redistribution from the initial Maxwellian to a shifted state greatly depleting the low velocity electrons. 97

Chapter 1

Introduction

The goal of this study is to obtain an accurate solution to the Rutherford scattering problem using a theoretical description of the microscopic dynamics of a binary collision between an electron and an ion in the presence of an intense, linearly polarized oscillating electric field. The kinetic model proposed is free of any assumptions about the general behavior of the collision (*i.e.* does not assume small angle collisional dominance) and modifies long-standing theories of the inverse bremsstrahlung heating of a plasma and collision transport processes.

For a plasma kinetic system dominated by electron-electron collisions, the electron distribution function (EDF) can be approximated by a Maxwellian distribution. This then allows reduction of the kinetic theory to hydrodynamical models that solve many problems in plasma physics. However, in a high Z , fully ionized plasma it has been established that there exists a large region of parameter space where electron-ion collisions dominate and govern the behavior of the EDF [1]. Further, Langdon [2] has shown that in this region, because of electron heating due to the electron-ion collisions in the high-frequency field, the EDF is highly non-Maxwellian. Thus it is essential that in order to describe the EDF in this region, the dynamics of the electron ion collisions be fully understood.

This study numerically solves the equation of motion for an electron scattering with an ion in the presence of an intense, high frequency dipole electric field. Our results indicate that the laser field can induce chaotic orbits where the electron is effectively trapped or experiences a series of correlated collisions, both of which lead to large angle scattering. We investigate the transport cross section of the interaction and show deviations of up to fifty percent from the Born approximation predictions of Shvets and Fisch [9] for the parallel launch condition. Further we propose a modification to the Rutherford cross section for elastic collisions in the presence of a high frequency field. Our investigation into inverse bremsstrahlung (IB) energy gain yields an expression for the effective cross section for $v < v_{osc}$. We also propose an increase in the IB heating rate for temperatures on the order of 100 eV. Preliminary particle simulations that incorporate our modified transport cross section show evidence of an increased heating rate as well as a flash redistribution of a Maxwellian velocity distribution resulting in a hole at low velocities.

1.1 Boltzmann Equation

I shall begin by deriving the Boltzmann kinetic equation generally following the arguments put fourth originally in 1872 [3, 4] and adapted by Balescu [27]. In doing so I will demonstrate where the work of this study fits in the realm of kinetic theory. Consider a neutral gas of like classical point particles of equal mass that interact through a short range potential $V(r)$. They are described by a distribution function $f_1(\vec{x}, \vec{v}, t)$. Boltzmann then describes the evolution of this distribution in time. The evolution can be separated into two categories: (i) free motion of the particles and (ii) the interaction processes that occur as a series of discrete binary collisions happening over a limited region of space (established by the effective range of the potential) and over a short period of time.

Accounting first for the free motion, it is assumed that outside of the collisions, the particles follow linear trajectories and therefore the evolution of $f_1(\vec{x}, \vec{v}, t)$ must satisfy the continuity equation

$$\frac{\partial}{\partial t} f_1(\vec{x}, \vec{v}, t) + \vec{v} \cdot \vec{\nabla} f_1(\vec{x}, \vec{v}, t) = 0. \quad (1.1)$$

To account for the collision consider the group of particles in phase space about \vec{x} and \vec{v} in the volume defined by d^3x, d^3v . For this group, the effect of the collisions can be modeled as gains determined by the operator G and losses determined by the operator L , to the number of particles in this phase point vicinity. Hence

$$\frac{\partial}{\partial t} f_1 + \vec{v} \cdot \vec{\nabla} f_1 = G - L, \quad (1.2)$$

where I have dropped the phase space variables and time to conserve space.

An elastic collision between two particles is depicted in Fig. (1.1).

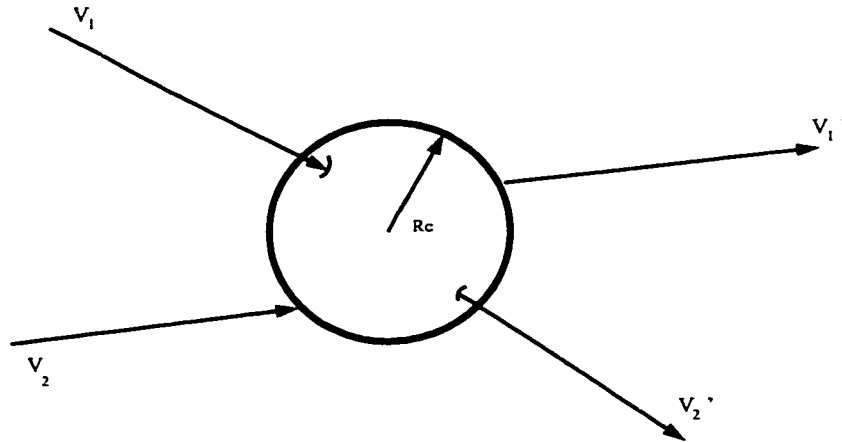


Figure 1.1: A sketch of a two body collision. The interaction sphere is defined at a radius R_c , the cutoff range of the potential.

A pair of particles with initial velocities \vec{v}_1 and \vec{v}_2 interact within the sphere of radius R_c which is defined by the cutoff range of the interaction potential.

The outcome of the collision results in velocities \vec{v}'_1 , and \vec{v}'_2 .

By conservation of momentum (recall each particle has the same mass) we know

$$\vec{v}_1 + \vec{v}_2 = \vec{v}'_1 + \vec{v}'_2. \quad (1.3)$$

And by conservation of energy,

$$v_1^2 + v_2^2 = v_1'^2 + v_2'^2. \quad (1.4)$$

The final velocities are then given by

$$\vec{v}'_1 = \frac{1}{2}(\vec{v}_1 + \vec{v}_2 + g\vec{\epsilon}) \quad (1.5)$$

$$\vec{v}'_2 = \frac{1}{2}(\vec{v}_1 + \vec{v}_2 - g\vec{\epsilon}), \quad (1.6)$$

where

$$\vec{g} = \vec{v}_1 - \vec{v}_2 \quad (1.7)$$

$$g\vec{\epsilon} = \vec{v}'_1 - \vec{v}'_2. \quad (1.8)$$

In an elastic collision, the magnitude of \vec{g} (the initial relative velocity) does not change, rather it experiences a rotation in velocity space to a new coordinate defined by $\vec{\epsilon}$. If we consider now Fig. (1.2), the scattering angle in the centre of mass frame can be seen as χ . To determine this, it is noted that

$$\chi = \pi - 2\theta, \quad (1.9)$$

where θ is the angle between the initial velocity and the vector position of closest approach (\vec{R}_{min}). θ is given [17] by the equation

$$\theta = \int_{R_{min}}^{\infty} dr \frac{\frac{\rho}{r^2}}{\sqrt{1 - \left(\frac{\rho}{r}\right)^2 - \frac{4V(r)}{g^2}}}. \quad (1.10)$$

Knowing the solution to the two-body interaction problem, the goal is now to estimate G and L. In a gas we are not concerned with the deflection of a single

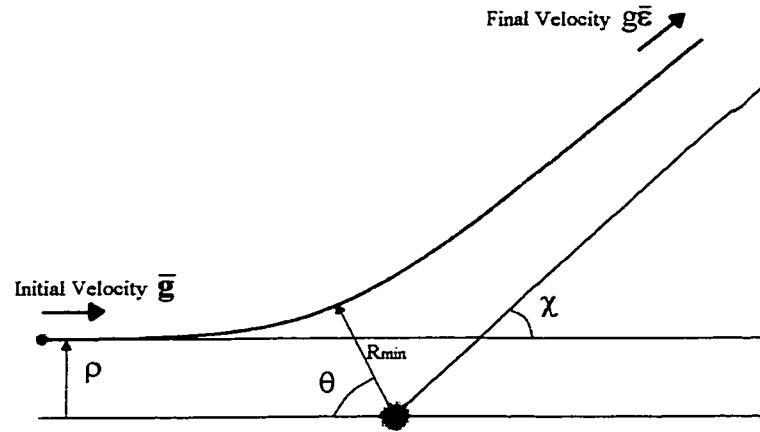


Figure 1.2: A sketch of a collision in the centre of mass frame. The incident particle approaches with velocity \vec{g} and is elastically scattered by interaction with the potential $V(r)$, resulting in a final velocity of $g\vec{e}$, at an angle χ to \vec{g} .

particle, but the scattering of a beam of incident particles all with a specified initial velocity. Obviously because of the different impact parameters the particles will be scattered into different angles χ . This is expressed in Fig.(1.3). Here we fix a reference frame on an individual particle at \vec{x} with velocity \vec{v}_1 at time t . Recalling that we have established the outer range of the potential as R_c , any particle that comes within this distance of the fixed body will then scatter. We then define a time period Δt that is a) much larger than the collision time T_c , and b) shorter than the relaxation time, *i.e.* the time for any change in the distribution function to occur. A cylindrical shell defined by the radii ρ and $\rho + d\rho$ and length $g\Delta t$ would then contain all the particles that will scatter into angle

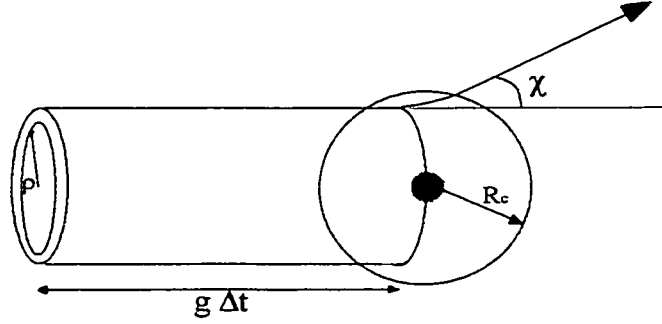


Figure 1.3: An annulus beam of incident particles with uniform initial velocity at a specific impact parameter ρ will scatter into the angle χ in time Δt .

χ . (Assuming of course that $\rho \leq R_c$.) Over the period Δt this number is

$$n = f(\vec{x}, \vec{v}_2, t) d^3 v_2 2\pi \rho d\rho g \Delta t. \quad (1.11)$$

The total number of collisions that involve the test particle over this time period per unit volume can be found by multiplying n by the number of particles at \vec{x} with a velocity of \vec{v}_1 . Integrating this expression over \vec{v}_2 we find an expression for the loss term L because these particles will change velocity from \vec{v}_1 .

$$\int d^3 v_2 f(\vec{x}, \vec{v}_2, t) f(\vec{x}, \vec{v}_1, t) d^3 v_1 2\pi \rho d\rho g \Delta t = L d^3 v_1 \Delta t \quad (1.12)$$

If we then consider the reverse symmetry of the problem, we would see collisions between particles with velocities of \vec{v}'_1 and \vec{v}'_2 and ending with \vec{v}_1 and \vec{v}_2

adding to this region of phase space, yielding the gain term G .

$$\int d^3v'_2 f(\vec{x}, \vec{v}'_2, t) f(\vec{x}, \vec{v}'_1, t) d^3v'_1 2\pi\rho d\rho g\Delta t = G d^3v'_1 \Delta t \quad (1.13)$$

The initial and final velocities here are related by a canonical transformation. Examining the Liouville theorem applied specifically to this two body problem where the collisions can be considered well-separated events in space and time, Balescu [27] notes that we can observe the equality

$$d^3v_1 d^3v_2 = d^3v'_1 d^3v'_2. \quad (1.14)$$

Thus, now having derived expressions for G and L , we can write the Boltzmann equation in its most basic form as

$$\frac{\partial}{\partial t} f(\vec{x}, \vec{v}_1, t) + \vec{v} \cdot \vec{\nabla} f(\vec{x}, \vec{v}_1, t) = \int d^3v_2 d\rho 2\pi\rho g [f(\vec{x}, \vec{v}'_1, t) f(\vec{x}, \vec{v}'_2, t) - f(\vec{x}, \vec{v}_2, t) f(\vec{x}, \vec{v}_1, t)]. \quad (1.15)$$

At this point I should introduce the differential cross section. Considering our model above, the differential cross section is defined as

$$d\sigma = \frac{dN}{n}, \quad (1.16)$$

where dN is the number of particles that scatter through angles between χ and $\chi + d\chi$ per unit time, and n is the total number of particles passing in unit time through unit area of the beam cross section. It is assumed that the beam is uniform over its cross section. From Fig. (1.3) it is apparent that all incident particles that pass through the cross section annulus defined by ρ and $\rho + d\rho$ will scatter as required, therefore this area to that of the unit beam cross section then defines the differential cross section, or

$$d\sigma = 2\pi\rho d\rho. \quad (1.17)$$

To relate $d\sigma$ to the scattering angle, we simply rewrite Eq.(1.17) as

$$d\sigma = 2\pi\rho(\chi) \left| \frac{d\rho(\chi)}{d\chi} \right| d\chi. \quad (1.18)$$

From here we can extend our definition from the plane angle element $d\chi$ to the solid angle element $d\Omega = 2\pi \sin(\chi)d\chi$. We then arrive at the expression

$$d\sigma = \sigma_d d\Omega, \quad (1.19)$$

where

$$d\sigma_d = \frac{d\rho(\chi)}{\sin(\chi)} \left| \frac{d\rho(\chi)}{d\chi} \right| d\chi. \quad (1.20)$$

Thus, the Boltzmann kinetic equation becomes

$$\frac{\partial}{\partial t} f(\vec{x}, \vec{v}_1, t) + \vec{v} \cdot \vec{\nabla} f(\vec{x}, \vec{v}_1, t) = C_B(f, f), \quad (1.21)$$

where

$$C_B(f, f) = \int d^3v_2 d\Omega g \sigma_d [f(\vec{x}, \vec{v}_1, t) f(\vec{x}, \vec{v}_2, t) - f(\vec{x}, \vec{v}_2, t) f(\vec{x}, \vec{v}_1, t)]. \quad (1.22)$$

Note that the notation is simplified such that $f(\vec{x}, \vec{v}_1, t) = f_1(\vec{x}, \vec{v}_1, t)$.

As a historical note, Boltzmann introduced the assumption that $f_2 = f_1 f_1$ or that there are no correlations before or after the collision which has come to be known as Boltzmann's *Stosszahlansatz*. The Boltzmann equation is a closed, nonlinear equation for the one-particle distribution function. Subsequently, many approximation techniques have been developed in search of its solutions.

1.2 The Landau Collision Operator

It is well known that the Boltzmann equation (1.22) can be solved ($C_B(f_M, f_M) = 0$) with a Maxwellian distribution of the form

$$f_M(\vec{x}, \vec{v}, t) = \left(\frac{m}{2\pi T(\vec{x}, t)} \right)^{\frac{3}{2}} e^{-\frac{m}{2T(\vec{x}, t)} (\vec{v} - \vec{u}(\vec{x}, t))^2}, \quad (1.23)$$

where $T(\vec{x}, t)$ is the temperature and $\vec{u}(\vec{x}, t)$ is the drift velocity.

We are however more interested in finding solutions that evolve outside of an equilibrium state (where the system is exposed to a heat source for example.) Here I present a derivation of the Landau collision operator as proposed by Landau in 1936 [5] to describe collisions between weakly interacting charged particles.

In deriving the Landau equation we assume that the collisions that occur between the particles in our system are a simple superposition of many small angle deflections with associated small changes in momentum.

Going back to the Boltzmann equation, Eq.(1.22), we can interpret $\sigma_d g$ as the probability density of a collision transforming the velocities \vec{v}_1 and \vec{v}_2 into \vec{v}'_1 and \vec{v}'_2 , thus

$$\sigma_d g \equiv w(\vec{v}_1, \vec{v}_2; \vec{v}'_1, \vec{v}'_2). \quad (1.24)$$

Also, equations 1.5 and 1.6 can be simplified by the introduction of the vector $\vec{\Delta}$ where

$$\vec{\Delta} = -\frac{1}{2}(\vec{g} - g\vec{e}), \quad (1.25)$$

so that now,

$$\begin{aligned} \vec{v}'_1 &= \vec{v}_1 + \vec{\Delta} \\ \vec{v}'_2 &= \vec{v}_2 - \vec{\Delta}. \end{aligned} \quad (1.26)$$

With this in mind, we can switch to the centre of mass frame and express the probability density in terms of new variables

$$\begin{aligned} w(\vec{v}_1, \vec{v}_2; \vec{v}'_1, \vec{v}'_2) &\rightarrow w\left[\frac{1}{2}(\vec{v}_1 + \vec{v}'_1), \frac{1}{2}(\vec{v}_2 + \vec{v}'_2); \vec{v}'_1 - \vec{v}_1, \vec{v}'_2 - \vec{v}_1\right] \\ &= w\left[\vec{v}_1 + \frac{1}{2}\vec{\Delta}, \vec{v}_2 - \frac{1}{2}\vec{\Delta}; \vec{\Delta}, -\vec{\Delta}\right] \\ &\equiv w\left[\vec{v}_1 + \frac{1}{2}\vec{\Delta}, \vec{v}_2 - \frac{1}{2}\vec{\Delta}; \vec{\Delta}\right]. \end{aligned} \quad (1.27)$$

This follows from the fact that the probability densities of the direct and inverse collisions are equal. Thus w is an even function in Δ .

$$w[\vec{v}_1 + \frac{1}{2}\vec{\Delta}, \vec{v}_2 - \frac{1}{2}\vec{\Delta}; \vec{\Delta}] = w[\vec{v}_1 + \frac{1}{2}\vec{\Delta}, \vec{v}_2 - \frac{1}{2}\vec{\Delta}; -\vec{\Delta}]. \quad (1.28)$$

The Boltzmann collision operator can then be expressed as

$$C_B(f, f) = \int d^3v_2 d\Omega w[\vec{v}_1 + \frac{1}{2}\vec{\Delta}, \vec{v}_2 - \frac{1}{2}\vec{\Delta}; \vec{\Delta}] [f(\vec{v}_2 - \vec{\Delta})f(\vec{v}_1 + \vec{\Delta}) - f(\vec{v}_1)f(\vec{v}_2)], \quad (1.29)$$

where the \vec{x} and t variables have been omitted to simplify the expression.

From this point it is necessary to assume that the interactions between particles are weak which means $\vec{\Delta}$ must be small compared to the velocities of our particles

$$\vec{\Delta} \ll \vec{v}_1 \quad ; \quad \vec{\Delta} \ll \vec{v}_2. \quad (1.30)$$

Under this assumption, the functions above can be approximated using Taylor series expansions

$$w[\vec{v}_1 + \frac{1}{2}\vec{\Delta}, \vec{v}_2 - \frac{1}{2}\vec{\Delta}; \vec{\Delta}] \simeq w[\vec{v}_1, \vec{v}_2; \vec{\Delta}] + \frac{1}{2}\Delta_r \left[\frac{\partial w[\vec{v}_1, \vec{v}_2; \vec{\Delta}]}{\partial v_{1r}} - \frac{\partial w[\vec{v}_1, \vec{v}_2; \vec{\Delta}]}{\partial v_{2r}} \right] + \dots \quad (1.31)$$

$$f(\vec{v}_1 + \vec{\Delta}) \simeq f(\vec{v}_1) + \Delta_r \frac{\partial f(\vec{v}_1)}{\partial v_{1r}} + \frac{1}{2}\Delta_r \Delta_s \frac{\partial^2 f(\vec{v}_1)}{\partial v_{1r} \partial v_{1s}} + \dots \quad (1.32)$$

The expansion for $f(\vec{v}_2 - \vec{\Delta})$ follows in a similar fashion. The indexes r and s are the three dimensional components of the vectors, *i.e.* $r, s = (x, y, z)$.

When the expanded terms are inserted into Eq.(1.29) we arrive at a new expression for the collisional operator

$$\begin{aligned} C_B(f, f) &\simeq \int d^3v_2 d\Omega \left[w[\vec{v}_1, \vec{v}_2; \vec{\Delta}] \left(f(\vec{v}_2) \frac{\partial f(\vec{v}_1)}{\partial v_{1r}} - f(\vec{v}_1) \frac{\partial f(\vec{v}_2)}{\partial v_{2r}} \right) \Delta_r \right. \\ &+ \frac{1}{2}\Delta_r \left(\frac{\partial w[\vec{v}_1, \vec{v}_2; \vec{\Delta}]}{\partial v_{1r}} - \frac{\partial w[\vec{v}_1, \vec{v}_2; \vec{\Delta}]}{\partial v_{2r}} \right) \Delta_s \left(f(\vec{v}_2) \frac{\partial f(\vec{v}_1)}{\partial v_{1s}} - f(\vec{v}_1) \frac{\partial f(\vec{v}_2)}{\partial v_{2s}} \right) \\ &+ w[\vec{v}_1, \vec{v}_2; \vec{\Delta}] \left(\frac{1}{2} \frac{\partial^2 f(\vec{v}_2)}{\partial v_{2r} \partial v_{2s}} f(\vec{v}_1) + \frac{1}{2} f(\vec{v}_2) \frac{\partial^2 f(\vec{v}_1)}{\partial v_{1r} \partial v_{1s}} - \frac{\partial f(\vec{v}_2)}{\partial v_{2r}} \frac{\partial f(\vec{v}_1)}{\partial v_{1s}} \right) \Delta_r \Delta_s \\ &+ \dots \left. \right] \quad (1.33) \end{aligned}$$

Recalling that $w[\vec{v}_1, \vec{v}_2, \vec{\Delta}]$ is an even function of $\vec{\Delta}$, the first order terms in the equation above vanish identically. Next, we perform an integration by parts with respect to \vec{v}_1 on the last two terms containing $\frac{\partial w}{\partial v_{2r}}$. The result is

$$\begin{aligned} C_B(f, f) &\simeq \int d^3v_2 d\Omega \frac{1}{2} \Delta_r \Delta_s \left[w[\vec{v}_1, \vec{v}_2; \vec{\Delta}] \left(-\frac{\partial f(\vec{v}_2)}{\partial v_{2r}} \frac{\partial f(\vec{v}_1)}{\partial v_{1s}} + f(\vec{v}_2) \frac{\partial^2 f(\vec{v}_1)}{\partial v_{1r} \partial v_{1s}} \right) \right. \\ &\quad \left. + \frac{\partial w[\vec{v}_1, \vec{v}_2; \vec{\Delta}]}{\partial v_{1r}} \left(\frac{\partial f(\vec{v}_1)}{\partial v_{1s}} f(\vec{v}_2) - f(\vec{v}_1) \frac{\partial f(\vec{v}_2)}{\partial v_{2s}} \right) \right] \\ C_B(f, f) &= \int d^3v_2 d\Omega \frac{1}{2} \Delta_r \Delta_s \left[w[\vec{v}_1, \vec{v}_2; \vec{\Delta}] \frac{\partial}{\partial v_{1r}} \left(f(\vec{v}_2) \frac{\partial f(\vec{v}_1)}{\partial v_{1s}} - f(\vec{v}_1) \frac{\partial f(\vec{v}_2)}{\partial v_{2s}} \right) \right. \\ &\quad \left. + \frac{\partial w[\vec{v}_1, \vec{v}_2; \vec{\Delta}]}{\partial v_{1r}} \left(\frac{\partial f(\vec{v}_1)}{\partial v_{1s}} f(\vec{v}_2) - f(\vec{v}_1) \frac{\partial f(\vec{v}_2)}{\partial v_{2s}} \right) \right]. \end{aligned}$$

This can then be written in the form

$$C_B(f, f) = \int d^3v_2 \frac{\partial}{\partial v_{1r}} G^{rs} \left(\frac{\partial}{\partial v_{1s}} - \frac{\partial}{\partial v_{2s}} \right) f(\vec{v}_1) f(\vec{v}_2) \quad (1.34)$$

where

$$G^{rs} = \frac{1}{2} \int d\Omega w[\vec{v}_1, \vec{v}_2; \vec{\Delta}] \Delta_r \Delta_s. \quad (1.35)$$

To place this equation into a more practical form, the next step is to express the tensor G^{rs} in terms of the interaction potential between the particles. Going back to our test collision, it can be seen that the velocity increment of the first particle $\vec{\Delta}$ can be expressed as the time integral of the force due to the second particle or

$$\vec{\Delta} = \frac{1}{m} \int_{-\infty}^{\infty} dt \left[-\frac{\partial V(\vec{x}_1(t) - \vec{x}_2(t))}{\partial \vec{x}_1(t)} \right]. \quad (1.36)$$

Again recalling that we are under the assumption that in this regime, the particles experience only weak coupling, we can infer the following approximation for the coordinate $r(\vec{t})$.

$$r(\vec{t}) \equiv x_1(\vec{t}) - x_2(\vec{t})$$

$$\begin{aligned}
&= \vec{x}_1 - \vec{x}_2|_{\text{initial}} + \int_0^t \vec{g}(t') dt' \\
&\simeq \vec{a} + \vec{g}t
\end{aligned} \tag{1.37}$$

Thus $r(\vec{t})$ is approximately defined by a free trajectory during the collision.

We next examine the potential in Fourier space, noting the Fourier transform

$$V(\vec{r}) = \int d\vec{k} V_k e^{i\vec{k}\cdot\vec{r}}. \tag{1.38}$$

Hence we observe

$$\begin{aligned}
\vec{\Delta} &= -\frac{1}{m} \int_{-\infty}^{\infty} dt \int \frac{d^3k}{(2\pi)^3} i\vec{k} V_k e^{i\vec{k}\cdot\vec{r}(\vec{t})} \\
&\simeq -\frac{1}{m} \int_{-\infty}^{\infty} dt \int \frac{d^3k}{(2\pi)^3} i\vec{k} V_k e^{i\vec{k}\cdot(\vec{a}+\vec{g}t)}.
\end{aligned} \tag{1.39}$$

It should also be noted that in cylindrical geometry

$$w[\vec{v}_1, \vec{v}_2; \vec{\Delta}] d\Omega = \sigma_d g d\Omega = 2\pi g \rho d\rho \tag{1.40}$$

Plugging these into the expression for G^{rs} , Eq.(1.35) we find

$$G^{rs} = \frac{1}{2m^2} \int_0^{2\pi} d\phi \int_0^{\infty} d\rho g \rho \int_{-\infty}^{\infty} dt_1 \int_{-\infty}^{\infty} dt_2 \int \frac{d^3k_1}{(2\pi)^3} \int \frac{d^3k_2}{(2\pi)^3} i k_{1r} i k_{2s} V_{k_1} V_{k_2} e^{i[\vec{k}_1\cdot\vec{r}(t_1)+\vec{k}_2\cdot\vec{r}(t_2)]} \tag{1.41}$$

To further simplify this expression, we recall the approximation Eq.(1.37) which allows us to say

$$e^{i[\vec{k}_1\cdot\vec{r}(t_1)+\vec{k}_2\cdot\vec{r}(t_2)]} = e^{i(\vec{k}_1+\vec{k}_2)\cdot(\vec{a}+\vec{g}t_1)} e^{i\vec{k}_2\cdot(\vec{g}t_2-\vec{g}t_1)}. \tag{1.42}$$

Also, we can take advantage of the cylindrical geometry and define the volume element $d^3r(t_1)$

$$\int d^3\vec{r}(t_1) \equiv \int_0^{2\pi} d\phi \int_0^{\infty} d\rho \rho \int_{-\infty}^{\infty} dt_1 g. \tag{1.43}$$

If we then introduce the variable $\tau = t_1 - t_2$, Eq.(1.41) reduces to

$$G^{rs} = \frac{1}{2m^2} \int d^3r(t_1) \int_{-\infty}^{\infty} d\tau \int \frac{d^3k_1}{(2\pi)^3} \int \frac{d^3k_2}{(2\pi)^3} e^{i(\vec{k}_1 + \vec{k}_2) \cdot \vec{r}(t_1)} i k_{1r} i k_{2s} V_{k_1} V_{k_2} e^{i\vec{k}_2 \cdot \vec{g}\tau}. \quad (1.44)$$

Recalling then the relation

$$\int d^3r(t_1) e^{i(\vec{k}_1 + \vec{k}_2) \cdot \vec{r}(t_1)} = (2\pi)^3 \delta(\vec{k}_1 + \vec{k}_2), \quad (1.45)$$

the tensor expression finally reduces to

$$G^{rs} = \frac{1}{m^2} \frac{1}{8\pi^3} \int d^3k_1 k_{1r} k_{1s} |V(\vec{k}_1)|^2 \delta(\vec{k}_1 \cdot \vec{g}). \quad (1.46)$$

Inserting this back into Eq.(1.34) we finally arrive at Landau's collision operator

$$C_L(f, f) = \frac{1}{8\pi^2 m^2} \int d^3v_2 \int d^3k_1 |V(\vec{k}_1)|^2 \times \vec{k}_1 \cdot \frac{\partial}{\partial \vec{v}_1} \left[\delta(\vec{k}_1 \cdot (\vec{v}_1 - \vec{v}_2)) \vec{k}_1 \cdot \left(\frac{\partial}{\partial \vec{v}_1} - \frac{\partial}{\partial \vec{v}_2} \right) f(\vec{v}_1) f(\vec{v}_2) \right]. \quad (1.47)$$

To take this one step further we recall that for a Coulomb gas the potential in Fourier space is given by

$$V(k_1) = \frac{4\pi Z e^2}{k_1^2}. \quad (1.48)$$

In this situation the Landau collision operator takes the form

$$C_L(f, f) = \frac{2Z^2 e^4}{m^2} \frac{\partial}{\partial \vec{v}_1} \int d^3v_2 \int d^3k_1 \frac{\vec{k}_1 \vec{k}_1}{k_1^4} \delta(\vec{k}_1 \cdot (\vec{v}_1 - \vec{v}_2)) \cdot \left(\frac{\partial}{\partial \vec{v}_1} - \frac{\partial}{\partial \vec{v}_2} \right) f(\vec{v}_1) f(\vec{v}_2). \quad (1.49)$$

This then gives us the famous *Landau equation* as proposed in 1936 [5], or the kinetic equation for a weakly coupled plasma. I shall return to this in subsequent chapters to explain where the assumptions fundamental to its derivation break down in the presence of a strong oscillating field. In a similar manner to the Boltzmann equation, Eq.(1.22), the Landau equation remains nonlinear in f .

1.3 The Rutherford Cross Section

Before I go on to talk about the specifics of the research in laser-plasma interactions, this thesis would not be complete without a classical derivation of the Rutherford scattering cross section. If we once again refer to Fig.(1.2), the binary collision in the centre of mass frame, the Rutherford scattering cross section corresponds to a two body interaction with the Coulomb potential as $V(r)$. Recall Eq.(1.10). Replacing $V(r)$, the potential energy of the system with $\frac{Ze^2}{r}$

$$\theta = \int_{R_{min}}^{\infty} dr \frac{\frac{\rho}{r^2}}{\sqrt{1 - \left(\frac{\rho}{r}\right)^2 - \frac{4Ze^2}{\mu r g^2}}}. \quad (1.50)$$

Note that the reduced mass of the system, $\mu = \frac{m_1 m_2}{m_1 + m_2}$, is used so that we are no longer confined to the assumption of identical mass particles. In effect this is because electron ion collisions are examined later where the masses are not equal. In this frame μ will reduce to approximately the mass of the electron. Performing the integration in Eq.(1.50) we find

$$\theta = \cos^{-1} \frac{\frac{Ze^2}{\mu g^2 \rho}}{\sqrt{1 + \left(\frac{Ze^2}{\mu g^2 \rho}\right)^2}}, \quad (1.51)$$

which can be expressed in the form

$$\tan^2 \theta = \frac{\mu^2 g^4 \rho^2}{Z^2 e^4}. \quad (1.52)$$

From the relation of θ to the scattering angle χ Eq. (1.9), one obtains

$$\cot^2 \frac{\chi}{2} = \frac{\mu^2 g^4 \rho^2}{Z^2 e^4}. \quad (1.53)$$

This can be differentiated with respect to χ , yielding on the left hand side $\frac{\cos \chi/2}{\sin^3 \chi/2} d\chi$, while on the right hand side we end up with a factor of $2\rho d\rho$. The latter allows us to use Eq. (1.18) to introduce the scattering cross section $d\sigma$.

Thus we see

$$\frac{\cos \chi/2}{\sin \chi/2} d\chi = \frac{\mu^2 g^4}{Z^2 e^4} \frac{d\sigma}{\pi}. \quad (1.54)$$

Using the definition $d\Omega = 2\pi \sin\chi d\chi$, we get the classical expression for the differential cross section

$$\frac{d\sigma}{d\Omega} = \frac{Z^2 e^4}{4\mu^2 g^4} \frac{1}{\sin^4 \chi/2}, \quad (1.55)$$

which is the Rutherford formula.

The classical transport cross section σ_{tr} , or the cross section for momentum transfer can then be calculated by integrating this expression over the solid angle sphere with the weighting function $1 - \cos \chi$, which represents the fractional change of momentum due to scattering. Choosing χ_{min} as the lower limit for the integration over χ gives us

$$\begin{aligned} \sigma_{tr} &= \int_{\chi_{min}}^{\pi} d\chi 2\pi \sin \chi (1 - \cos \chi) \frac{Z^2 e^4}{4\mu^2 g^4} \frac{1}{\sin^4 \chi/2} \\ &= 4\pi \frac{Z^2 e^4}{\mu^2 g^4} \ln \left[\frac{1}{\sin \chi_{min}/2} \right]. \end{aligned} \quad (1.56)$$

The cross section(1.56) diverges as χ_{min} approaches zero which is a consequence of the long range Coulomb potential of interaction. In the specific treatment of the electron-ion collision, the reduced mass is well approximated by that of the electron, and because of the large mass difference, the ions are generally considered stationary objects, thus the relative velocity \vec{g} reduces to the velocity of the electron alone.

$$\sigma_{tr} = 4\pi \frac{Z^2 e^4}{m_e^2 v^4} \ln \left[\frac{1}{\sin \chi_{min}/2} \right] \quad (1.57)$$

Chapter 2

Microscopic Electron-Ion Collisions

2.1 Background

The dynamics of the binary electron-ion collision in a plasma in the presence of a strong laser field are of fundamental importance in predicting the inverse bremsstrahlung absorption of electromagnetic radiation and transport processes. With the recent development of terawatt lasers, this issue has received a great deal of attention [6]- [13]. The standard approximation involves a small-angle scattering model where the electrons are assumed to obey linear trajectories with the effects of collisions occurring as first order perturbations [8-10]. Such a model is limited, however, to cases where the impact parameter is large versus the quiver distance $r_{osc} = eE/m\omega_0^2$, and the drift velocity is large versus the quiver velocity

Formally, our system is described as follows. We consider an electron-ion collision in the centre of mass frame in the limit where the ion of charge Ze is stationary. An electron of charge e is assumed to be launched with a drift velocity parallel to

the z axis. We model the laser's electric field as a linearly polarized wave given by the equation

$$\vec{E}(\vec{R}, t) = E\vec{n} \sin(\omega t + \theta). \quad (2.1)$$

Here \vec{n} is a unit vector that defines the arbitrary orientation of the field while ω is the frequency of the laser. For reasons discussed below \vec{n} is defined by an angle with respect to the z axis. Because we investigate the high frequency regime it is assumed that $\omega > \omega_{pe}$ (where ω_{pe} is the plasma frequency), thus assuring that the laser field will propagate in the plasma. Such a model can be used locally to approximate the field in laser produced plasmas at high, close to critical, densities, where the laser wavelength is long compared to the distance scales involved in the collision process. The magnetic field exerts on the particles a Lorentz force that will have a maximum on the order of $\frac{v_{osc}}{c}$ which, even for the most extreme intensities we investigate, will be under ten percent. Thus, all relativistic effects are neglected.

To define the equation of motion of the electron we need the potential due to the ion. Ideally this would be given by the $1/R$ Coulomb potential however, in order to more closely model a plasma system we have incorporated both a large and small scale limit to this potential. First, the Debye screening limits the long range at the Debye length λ_D . Second, the quantum diffraction effects, limit the ion's potential at its deBroglie wavelength $\lambda_H = h/m_i v_{th}$. Hence we arrive at a potential given by

$$V(R) = \frac{Ze}{R}(1 - e^{-R/\lambda_H})e^{-R/\lambda_D}. \quad (2.2)$$

Shvets [9] invokes a few different schemes for reducing the potential at the Coulomb singularity, but this was done specifically to avoid large angle scattering. The systems investigated by Fraiman *et al.* [12, 13] and Wiesenfeld [11] simply invoke an unmodified Coulomb potential. With the potential above, the equation

of motion for the electron becomes

$$\begin{aligned}\ddot{\vec{R}} &= -\frac{Ze^2 \vec{R}}{mR^3} e^{-R/\lambda_D} \left(1 + \frac{R}{\lambda_D}\right) \\ &+ \frac{Ze^2 \vec{R}}{mR^3} e^{-R(1/\lambda_D + 1/\lambda_H)} \left(1 + R\left(\frac{1}{\lambda_D} + \frac{1}{\lambda_H}\right)\right) \\ &+ \frac{eE}{m} \vec{n} \sin(\omega t).\end{aligned}\quad (2.3)$$

The equation of motion is normalized using $\vec{R}' = \frac{\vec{R}}{r_E}$ and $t' = \omega_E t$, where the characteristic variables are established from the Keplerian orbit problem

$$r_E = \sqrt{\frac{eZ}{E}}, \quad \omega_E = \sqrt[4]{\frac{eE^3}{m^2 Z}}, \quad \nu_E = \sqrt[4]{\frac{Ze^3 E}{m^2}}.\quad (2.4)$$

These are arrived at by setting r_E as the distance from the ion where a regular Coulomb field Ze/r_E^2 is equal to the magnitude of the field E . Thus ω_E is then the frequency of a Keplerian orbit around the ion. Further, for reference, it can be shown that

$$r_E = \Omega^2 r_{osc}, \quad \nu_E = \Omega \nu_{osc},\quad (2.5)$$

where

$$r_{osc} = \frac{eE}{m\omega_0^2}, \quad \nu_{osc} = \frac{eE}{m\omega_0}, \quad ,\quad (2.6)$$

and

$$\Omega = \frac{\omega_0}{\omega_E} = \omega_0 \left(\frac{m^2 Z}{eE^3}\right)^{\frac{1}{4}}.\quad (2.7)$$

Hence in the new variables our equation of motion reduces to

$$\ddot{\vec{R}} = -\frac{\vec{R}}{R^3} e^{-R/\lambda_D} \left(1 + \frac{R}{\lambda_D}\right)$$

$$\begin{aligned}
& + \frac{\vec{R}}{R^3} e^{-R(1/\lambda_D + 1/\lambda_H)} \left(1 + R \left(\frac{1}{\lambda_D} + \frac{1}{\lambda_H} \right) \right) \\
& + \vec{n} \sin(\Omega t).
\end{aligned} \tag{2.8}$$

We will solve Eq.(2.8) for the trajectory of an electron using the symplectic integration algorithm defined below for chosen ranges of impact parameters, initial velocities, and phase of the laser field. From the trajectories we are able to measure the pitch angle scattering with a collision angle ϕ as well as the kinetic energy of the electron both before and after the collision. The angle itself is calculated by examining the ratio of the z component of the final drift velocity after the collision, to the total drift velocity after the collision (with the oscillations due to the field subtracted from the motion of the electron).

$$\cos \phi = \frac{\vec{v}_{z,out}}{\vec{v}_{tot,out}} \tag{2.9}$$

To incorporate the incident phase into the initial conditions, we divided our general coordinates $(\vec{R}(t), \vec{V}(t))$ into oscillatory and drift components

$$\vec{R}(t) = \vec{r}(t) - \vec{r}_{osc} \sin(\Omega t), \quad \vec{r}_{osc} = \frac{1}{\Omega^2} \vec{n} \tag{2.10}$$

$$\vec{V}(t) = \vec{v}(t) - \vec{v}_{osc} \cos(\Omega t), \quad \vec{v}_{osc} = \frac{-1}{\Omega} \vec{n}. \tag{2.11}$$

All launches are initiated with the spatial drift coordinate $(\vec{r}(t=0))$ on the launching grid and the initial drift velocity $(\vec{v}(t=0))$ along the z axis. The phase θ then modifies the initial conditions by adding a phase, or oscillatory component. The initial conditions are given by

$$\vec{R}(t=0) = \vec{r}(t=0) - \vec{r}_{osc} \sin(\theta), \tag{2.12}$$

$$\vec{V}(t=0) = \vec{v}(t=0) + \vec{v}_{osc} \cos(\theta). \tag{2.13}$$

The offset due to the phase of the field is then averaged over by repeating each launch with the same drift coordinates and varying θ from 0 to 2π .

2.3 The Algorithm

Numerical simulation of the problem is carried out using the fourth order algorithm for symplectic integration outlined by Candy and Rozmus [14, 15]. This algorithm offered a simple scheme for a Δt time-step integration of a system with a separable Hamiltonian. Essentially the symplectic technique has been developed to conserve volume in phase space during the numerical integration. Thus, it preserves the hierarchy of global invariants in the system such as energy and momentum. The results of our initial investigations into this problem are compared to typical Runge-Kutta trials on a straight forward Rutherford scattering system and are seen to demonstrate significantly less discrepancy from analytical predictions for the final scattering angles.

The fourth order symplectic integration algorithm (SIA) described the evolution of a system with a separable Hamiltonian in the general form

$$H(p, q, t) = \frac{p^2}{2m} + V(q, t), \quad (2.14)$$

coupled with the initial conditions $(\vec{q}_0, \vec{p}_0, t_0)$. Hamilton's equations of motion can then be generated to yield the forces and velocities necessary to perform the time step integration according to a cycled loop for $i= 1$ to 4

$$\vec{p}_i = \vec{p}_{i-1} + b_i \vec{F}(\vec{q}_{i-1}, t_{i-1}) \Delta t, \quad (2.15)$$

$$\vec{q}_i = \vec{q}_{i-1} + a_i \vec{P}(\vec{p}_i) \Delta t, \quad (2.16)$$

$$t_i = t_{i-1} + a_i \Delta t. \quad (2.17)$$

This results in the new coordinates (\vec{q}_n, \vec{p}_n) at $t = t_0 + \Delta t$. The constants (a_i, b_i) are defined in [14] as

$$\begin{aligned} a_1 = a_4 &= \frac{1}{6}(2 + 2^{1/3} + 2^{-1/3}), \\ a_2 = a_3 &= \frac{1}{6}(1 - 2^{1/3} + 2^{-1/3}), \end{aligned}$$

$$\begin{aligned}
b_1 &= 0, \\
b_2 = b_4 &= \frac{1}{2 - 2^{1/3}}, \\
b_3 &= \frac{1}{1 - 2^{2/3}}.
\end{aligned}
\tag{2.18}$$

The actual forces in our problem are determined from the Hamiltonian

$$H(R, \dot{R}) = \frac{\dot{R}^2}{2} - \frac{Ze}{R}(1 - e^{-R/\lambda_H})e^{-R/\lambda_D} - R \sin(\Omega t), \tag{2.19}$$

resulting in the force expression shown in Eq.(2.8).

The only significant problem presented by this algorithm is the choice of the time step Δt . It is obvious that if this is chosen too large, we would not be able to resolve the motion of the electron near the Coulomb singularity since its kinetic energy drastically increases in this region. Conversely, if chosen too small, the simulation would place unnecessary constraints on memory and computation time. Fraiman *et al.* [12, 13] introduced a time transformation to help resolve this issue, however in the interest of simplicity we introduce a cascading test condition that set the appropriate timestep to use based on the location of the particle at the beginning of each integration cycle. This algorithmic solution proves successful in resolving the motion of the particle in all valid regions.

2.4 Testing the Classical Results

Before going on to investigate the effects of the dipole field on the scattering we demonstrate that this algorithm can generate acceptable results for a known case. The best possible situation to model is the classical Rutherford scattering case where the external field is turned off. Recall that the differential transport cross section derived in chapter 1 is given by Eq. (1.57)

$$\sigma_{tr}(v) = \frac{4\pi Z^2 e^4}{m^2 v^4} \ln \Lambda_0 \tag{2.20}$$

where $\ln \Lambda_0$ is the Coulomb logarithm [16]. In the unit convention established above, this reduces simply to

$$\sigma_{tr}(v) = \frac{4\pi}{v^4} \ln 5v^2. \quad (2.21)$$

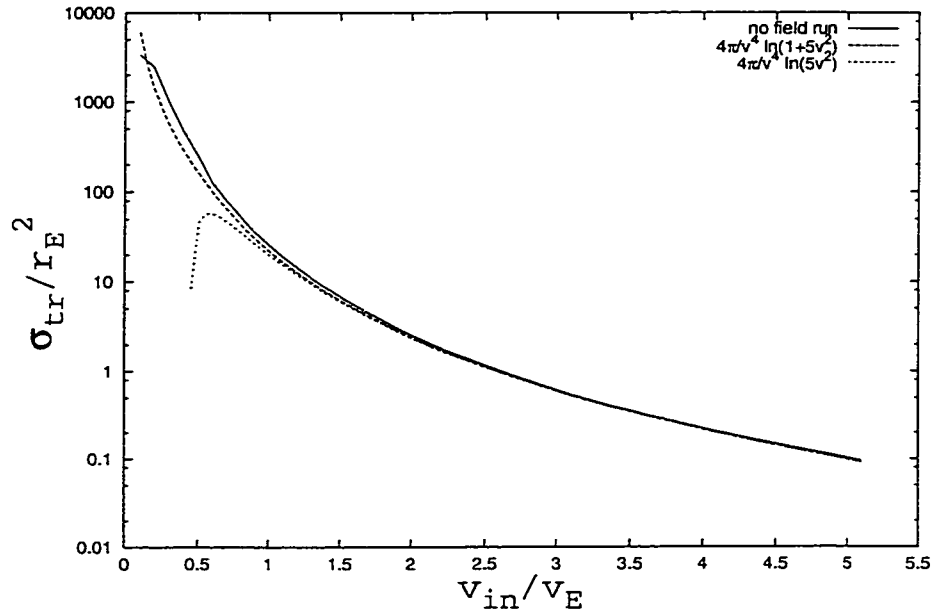


Figure 2.1: The conformation of the output of the simulation to the analytical expression in equation 2.21 is a clear demonstration of the accuracy of the algorithm.

A more detailed discussion of this formulation, in particular the reduction of the Coulomb logarithm to $5v^2$ is done in section 3.2. The output of this expression is listed in Fig.(2.1) and superimposed on the data obtained for the no field run. As is apparent, the code and the analytical expression agree within logarithmic, numerical accuracy, with a deviation only for small velocities. This evidence suggests the code is able to accurately describe the collisions it was intended to simulate. It was found that the logarithmic divergence seen in small

velocities can be safely removed by altering the argument of the logarithm to $1 + 5v^2$.

2.5 Individual Collisions

The overall object of this study is to examine the effects of the oscillating dipole electric field on the scattering and through averaging gain insight into the effects of the inverse bremsstrahlung energy gain. We have been able to resolve behaviors that result in large angle scattering. Interestingly enough, we find that on average the scattering angle is reduced as compared with the Rutherford case. The following figures are included to represent the different observed trajectories.

Fig.(2.2) shows the electron trajectory scattering plane with the ion located at the origin. If we define a small angle as any angle less than $\frac{\pi}{3}$, then the scattering observed without the field represents a typical case of small angle scattering in the system. It is this small angle scattering that is assumed to dominate the collisions during the heating of plasmas by an oscillatory field.

Here the electron is launched parallel to the z axis with an initial velocity equivalent to v_E and an impact parameter of $2r_E$ along the x axis. In this case the electric field is oriented along the y axis so the displacement in the y direction arises from the oscillations of the electron in the field, however as this figure is a projection on the scattering plane, this is not resolved here. The intensity of the field is incorporated into the dimensionless frequency $\Omega = 1$, which corresponds to about $10^{15} \frac{W}{cm^2}$. It should be noted that at this intensity $r_E = r_{osc}$ and $v_E = v_{osc}$ from Eq.(2.5). The trajectory is superimposed over a classical Rutherford scattering (no external field) trajectory. It is widely accepted [8–10] that this small angle change which follows the Rutherford trajectory prediction makes up a strong majority of the collisions that are seen in weakly coupled plasmas.

Figure 2.3 illustrates the same collision as in figure 2.2 only in three dimen-

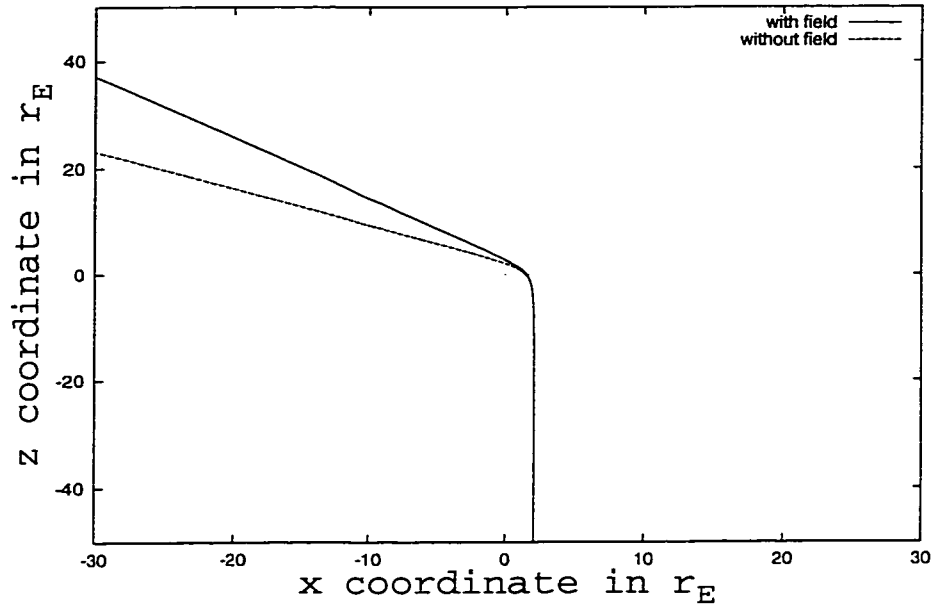


Figure 2.2: An example of small angle scattering for an electron launched with an initial velocity of v_E and an impact parameter of $2r_E$ inside an electric field oriented along the z axis, parallel to the initial drift velocity. The Rutherford trajectory is superimposed under the trajectory in the presence of the external field. Most analytical work assumes that such trajectories dominate the collisions. Note the reduction of the scattering angle in the presence of the field.

sions. This view allows for the resolution of the oscillations in the electron's trajectory and provides an overall description of the collision. It is rotated such that the electron is incident on the ion from the top left in order to give a clear view of the path difference after the collision has occurred.

The essence of this study is to observe the overall effect of the laser field on the collisions at the microscopic level. It is clear that for a field orientation perpendicular to the scattering plane, the resultant scattering angle of the electron's trajectory is reduced. This angle reduction however, is not always observed. As mentioned, the work of Fraiman *et al.* [12, 13] identified cases where the laser

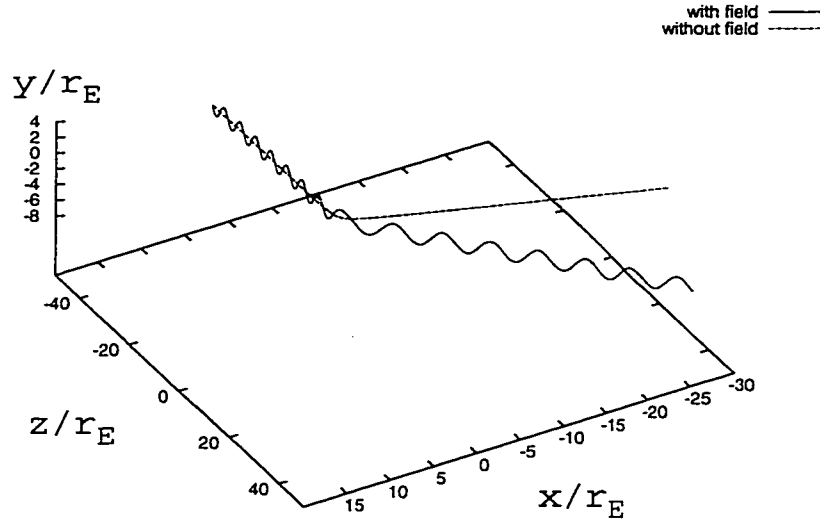


Figure 2.3: The same collision as shown in projection in figure 2.2. The axes have been rotated as to give the best qualitative picture possible and illustrate the end path difference for the case including the field.

field induces large angle scattering. Two processes have been identified as the culprits responsible for this behavior.

Fig.(2.4) illustrates an example of a large angle scattering case that occurs in our model. Here we describe the trajectory of a particle in the same field magnitude ($\Omega = 1$), with the same initial velocity and impact parameter as that in Eq.(2.2). Here however the external field is oriented along the z axis parallel to the incident launch velocity, and in this case its initial phase is set at $\frac{\pi}{2}$. It is obvious here that once the electron enters the ion field, it becomes trapped in a chaotic orbit. The end result is a final velocity in the fourth quadrant, well outside of the small angle regime established at $\frac{\pi}{3}$.

Obviously such events will contribute to an increase in the pitch angle scattering of the electrons in the kinetic model. The number of electrons experiencing

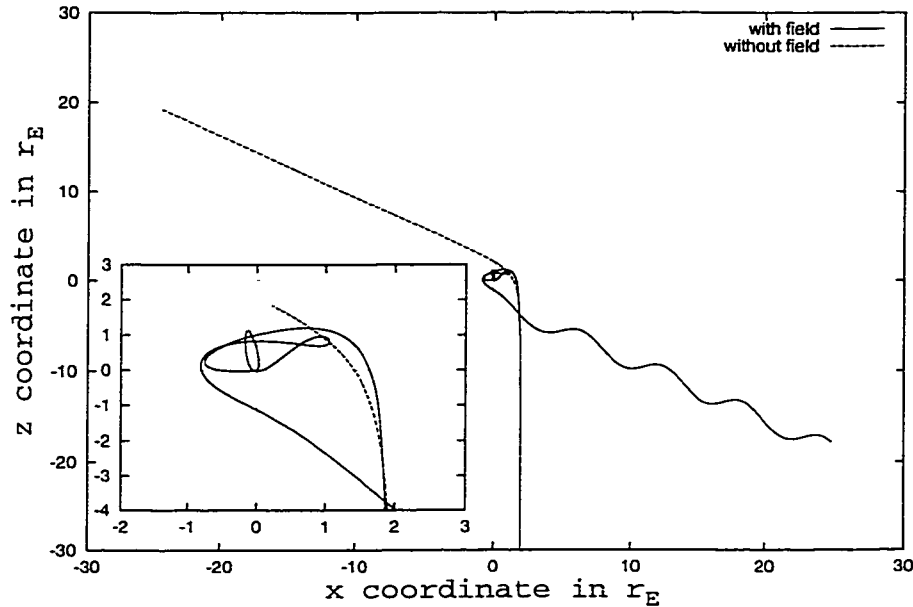


Figure 2.4: An example of trapping under conditions similar to those in Fig.(2.2). The external laser field has been oriented parallel to the launch direction (along the z axis). Note the chaotic orbit of the electron before it finally escapes into the fourth quadrant (inset).

such events is small and generally confined to those with smaller velocities.

Additionally, we also see an event where the electron experiences multiple deflections. This effect naturally becomes more pronounced for higher field intensities (which translates to lower values for our dimensionless frequency.) This behavior, suggested in [8], which occurs when the electron oscillates in and out of the interaction sphere, is depicted in Fig.(2.5). Here the frequency is set at $\Omega = 0.5$. It is apparent that the multiple collisions are the reason for the deviation of the electron's drift coordinate from that suggested by the no external field case superimposed below.

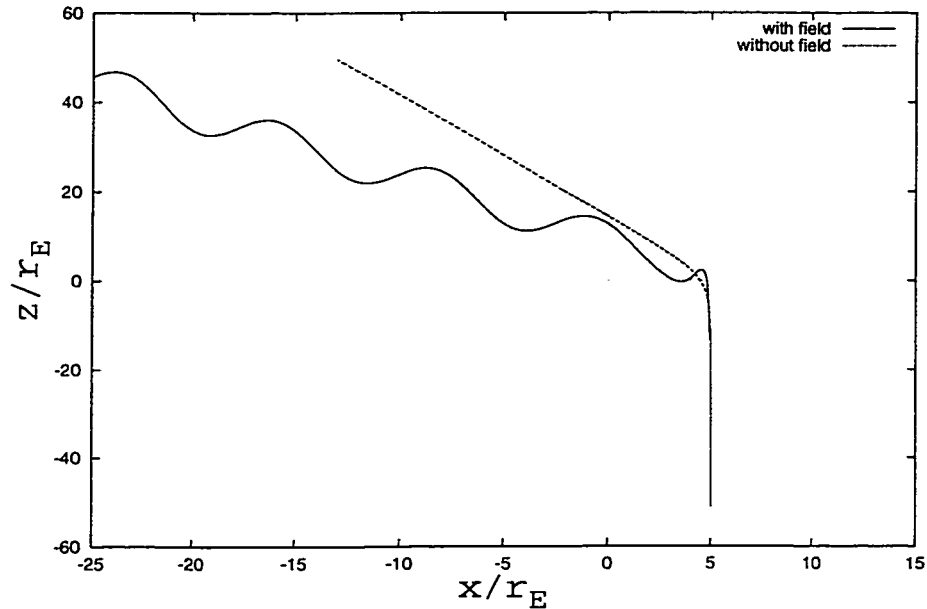


Figure 2.5: An example of correlated collisions where the external field is again oriented parallel to the launch velocity, along the z axis. This effect naturally becomes more important as the strength of the field is increased which is why we illustrate here the $\Omega = 0.5$ case. For an impact parameter of $5r_E$ and initial velocity of v_E we can see a significant deviation of the trajectory for a system exposed to the field.

2.6 Chaotic Scattering

Before continuing to the next chapter where I will explain the details of the transport cross section investigation, I should mention that the outcome of the scattering process is no longer determined by a straight forward relation as in the classical Rutherford case. The introduction of the laser field to the problem yields a system with extreme sensitivity to the initial conditions or launch parameters.

Wiesenfeld [11] presented a similar two dimensional (four dimensional phase space) study that looked at the inelastic scattering of an electron by an un-screened Coulomb potential. He showed that for low drift velocities and impact

parameters lower than τ_{osc} , the electron undergoes chaotic motion.

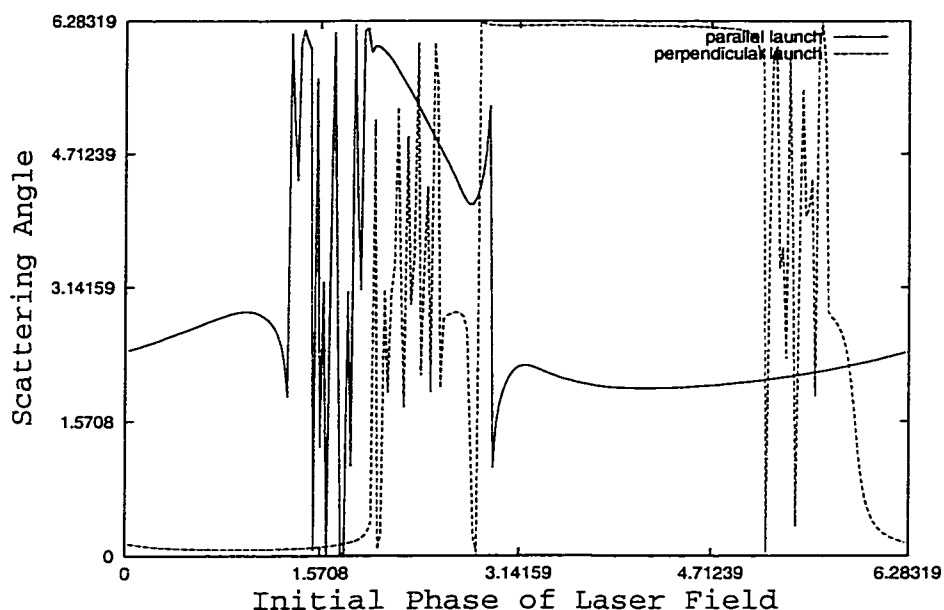


Figure 2.6: An example of the sensitivity of the final scattering angle to the initial phase of the laser field. 240 launches were performed with the parameters: $\nu = 0.5$, $\Omega = 0.3$, and impact parameter $\rho = 0.2$. Orientations of the laser field both parallel and perpendicular to the incident launch velocity are depicted. Notice that there are regions where the scattering angle is reasonably stable, and regions where it is chaotic.

Our simulations confirmed that the resulting scattering angle as well as the electron IB energy absorption do in fact have an extreme sensitivity to the initial phase of the laser field. Consider Fig.(2.6), which illustrates the resulting scattering angles for an electron launched with the parameters $\nu = 0.5$, $\Omega = 0.3$, and impact parameter $\rho = 0.2$ in both a parallel and perpendicular field alignment. The figure clearly shows both regions of reasonably stable and chaotic scattering angles. Because of the high magnitude of the electric field when $\Omega = 0.3$, the oscillations are large enough that for the right initial phase the electron has a

chance to circumvent the ion without traveling excessively close, thus avoiding the trapping scenarios resulting in a stable scattering angle. However, if the initial phase is altered such that the laser field then forces the electron to return to the ion after an initial pass, or simply pushes it very close to the ion centre, both the trapping and correlated collisional cases occur, resulting in chaotic motion often including large angle scattering.

Chapter 3

Transport Cross Section

3.1 Determining the Transport Cross Section

In order to determine the significance of the different trajectories observed in the previous chapter on the transport cross section we commence a series of tests launching millions of electrons at our ion target all with different initial conditions of field phase, position on the launching grid (impact parameter), velocity and orientation of the laser field. The theoretical system is illustrated by the cartoon in Fig.(3.1).

The loss of directed particle velocity is characterized by the rate of pitch angle scattering, which is in turn described by the transport collision frequency ν_{tr} . After scattering through an angle ϕ , the loss of initial velocity is $v_{in}(1 - \cos \phi)$. Thus the transport collision frequency is defined as

$$\nu_{tr} = n_i v_{in} \int \int \langle 1 - \cos \phi \rangle d^2 \rho. \quad (3.1)$$

From this point we are able to arrive at an expression for the transport cross section.

$$\sigma_{tr}(v) = \int \int \langle 1 - \cos \phi \rangle d^2 \rho \quad (3.2)$$

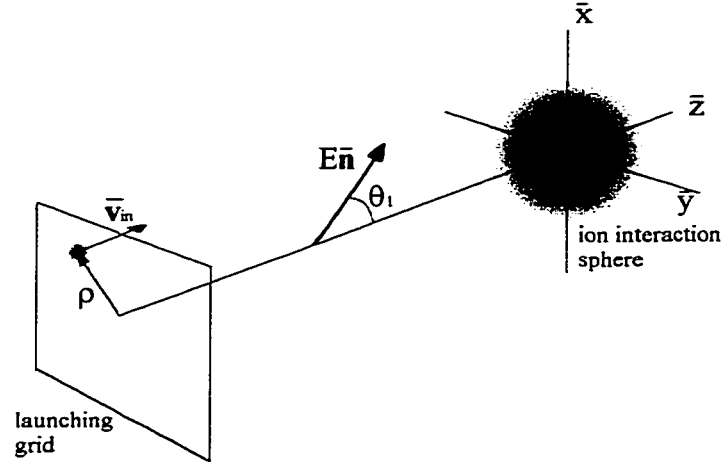


Figure 3.1: This figure illustrates the coordinate system used, as well as the concept of the launching grid. In general the diagram is not to perfect scale. The ion interaction sphere is defined by a Debye length as its radius.

Again this is given in the normalized units outlined in the previous chapter. The square brackets indicate averaging over the initial phase of the laser field. A more common practical formulation of the transport cross section is

$$\sigma_{tr}(v) = \int_0^{\infty} \langle 1 - \cos\phi \rangle 2\pi\rho d\rho. \quad (3.3)$$

This expression is commonly adopted for the classical analysis of the problem. However, implicit in this formulation is the assumption of cylindrical symmetry, which after careful inspection, is invalid in our problem. Going back to the original definition, we define our cross section as the ratio of the flux of electrons scattered into the solid angle $d\Omega$ to the total number of particles that pass in

unit time and through unit area incident on the ion.

$$d\sigma = \frac{dN}{N} \quad (3.4)$$

To consider the total compliment of incident particles, one needs simply to integrate over the annulus defined by $2\pi\rho$ for all values of ρ pertinent to the problem. The problem is that because we have inserted a laser field with a component aligned perpendicular to the z axis, an electron with its initial position at one point in the azimuthal angle will have a different equation of motion than one with a different value. Thus the cylindrical symmetry of the problem is destroyed and we revert our expression for the cross section back to that given in Eq.(3.2).

Particles at infinitely far distances will contribute nothing to this problem. The parameter ρ_{max} is introduced as a limit of integration. It is defined as the maximum impact parameter at which the electron will feel any significant perturbation to an otherwise linear trajectory. Generally this depends on the density of the plasma and must satisfy the restriction:

$$\frac{4\pi}{3}\rho_{max}^3 n_i = 1 \quad (3.5)$$

By this definition ρ_{max} becomes the average distance between ions in the plasma. Should the integration exceed this maximum value, we would be forced to abandon the binary collision model all together as we would then be considering a many body problem. Taking a density of $10^{21}cm^{-3}$ and a temperature of 1keV (10^7K) we find that the average distance between ions in a high Z plasma is approximately a Debye length, λ_D . Thus for these parameters, we are easily confined to a binary problem.

$$\sigma_{tr}(v) = \int_{-\rho_{max}}^{\rho_{max}} \int_{-\rho_{max}}^{\rho_{max}} \langle 1 - \cos\phi \rangle dx dy \quad (3.6)$$

The averaging procedures are performed numerically. The number of points over which to average all subsequent parameters are chosen using the criterion that all observed behavior had to be resolved. Thus in order to account for the stochastic nature of the scattering outlined in the previous chapter, when averaging over the initial phase of the laser field, a minimum of sixty points between 0 and 2π are used. As velocity increases it is found that up to a thousand points are necessary. Further, 92 points are taken for the launch coordinates in both the x and y directions for a total of 8464 points. Finally the velocities are examined from $\nu = 0.1-8.0 \nu_E$ (sometimes even higher) for a total of at least 80 points.

Each transport cross section produced by this definition is found for a given field intensity defined by the dimensionless frequency. Through this investigation, we examine six different intensity cases of $\Omega = 0.50, 0.30, 0.25, 0.20, 0.10$ and the no field situation. This range corresponds to field intensities of $10^{16} W/cm^2$ to over $10^{17} W/cm^2$ and obviously the zero intensity case. It should be mentioned that the trials of $\Omega = 0.10$ are included to examine the upper range of laser intensity, however, these have to be taken as academic results only. At such a high intensity, the oscillation displacement τ_{osc} is so large that we would be required to expand the formulation of our system beyond the binary collision problem.

The transport cross section, expressed as a function of initial drift velocity and field magnitude and frequency, allows us to determine the electron ion transport collision frequency as indicated by Eq. (3.1) by the simple relation

$$\nu_{tr} = \sigma_{tr} n_i \nu_{drift}, \quad (3.7)$$

which can then be assimilated into a particle code for further investigations such as the inverse bremsstrahlung heating of the plasma which incorporates such large angle collisions. (See chapter 5.) However this only gives a pitch angle

contribution to the scattering rate for elastic collisions. Inelastic effects are not included here.

The process requires one additional step. In order to obtain a complete expression for the transport cross section, we must average over all possible orientations of the field. However, before those results are presented, it is important to discuss the initial results that were obtained from a more simple situation where the external laser field was set parallel to the launch direction along the z axis.

3.2 The Case of the Parallel Launch

This particular situation has been the object of previous investigations [9, 12, 13], and in particular Shvets *et al.* [9] has obtained an analytical result based on the Born approximation which I shall use for comparison. It should be noted that Shvets explicitly assumed the dominance of small angle collisions.

To consider this particular case, it was assumed that the impact parameter is aligned such that $\vec{\rho} = \vec{e}_x \rho$ thus establishing x-z to be the collisional plane. Further, the drift velocity of the electron is initially set along the z axis. And finally, the electric field is oriented along the z-axis as well.

Given these initial conditions, Shvets managed to analytically predict the average deflection angle (denoted as $\delta\theta$ in reference [9], but referred to here as ϕ). From this and the definition of pitch angle scattering, he obtained the rate of pitch angle scattering ν_{tr} , which in conjunction with Eq.(5.43) yields the expression

$$\sigma_{tr} = \frac{A}{v^4} \ln(k_{max} \lambda_D) + \sum_{n=1}^{n=\infty} 2J_n^2 \left(\frac{n\omega r_{osc}}{v} \right) \left[\left(\frac{1}{2} + \frac{n^2 \omega^2}{k_{max}^2 v^2} \right) \ln \left(1 + \frac{k_{max}^2 v^2}{n^2 \omega^2} \right) - 1 \right] \quad (3.8)$$

Note that

$$A = \frac{4\pi Z^2 e^4}{m^2}, \quad (3.9)$$

and the term k_{max} is defined as

$$k_{max} = \frac{mv^2}{2Ze^2}, \quad (3.10)$$

the distance of closest approach for like particles.

As I will be coming back to it later, it is worth mentioning here that the first term recovers the classical expression for the transport cross section in the absence of an external laser field 2.21. It was pointed out by Shvets that this term corresponds to the $n=0$ case which described the elastic component of the collision (all terms with $n \geq 1$ were shown to have dependence on the initial phase of the field and therefore had some inelastic contribution). Thus by the first term, the classical expression

$$\sigma_{tr}(v) = \frac{A}{v^4} \ln \Lambda_0 \quad (3.11)$$

is recovered where $\ln \Lambda_0 = \ln k_{max} \lambda_D$ is the Coulomb logarithm.

As a brief aside, in our units k_{max} can be written,

$$k_{max} = \frac{mv'^2 v_E^2}{2Ze^2}. \quad (3.12)$$

In our system we are taking the inter-ion distance (ρ_{max}) to be approximately $10r_E$, which is the approximate value for a plasma with a temperature on the order of 10^7 K, or 1keV. Coupled together, this makes

$$k_{max} \rho_{max} = \frac{mv'^2 v_E^2}{2Ze^2} 10r_E, \quad (3.13)$$

which then reduces to

$$k_{max} \rho_{max} = 5v^2, \quad (3.14)$$

in our units. Therefore leaving us with the normalized expression for the transport cross section of

$$\sigma_{tr}(v) = \frac{4\pi}{v^4} \ln(1 + 5v^2). \quad (3.15)$$

The extra term in the logarithm has been inserted to avoid the logarithmic divergence for small velocities.

Converting equation 3.8 into the unit convention established above

$$\sigma_{tr} = \frac{4\pi}{v^4} \ln(5v^2) + \sum_{n=1}^{n=\infty} 2J_n^2 \left(\frac{n}{\Omega v} \right) \left[\left(\frac{1}{2} + \left(\frac{2n\omega}{v^3} \right)^2 \right) \ln \left(1 + \left(\frac{v^3}{2n\omega} \right)^2 \right) - 1 \right]. \quad (3.16)$$

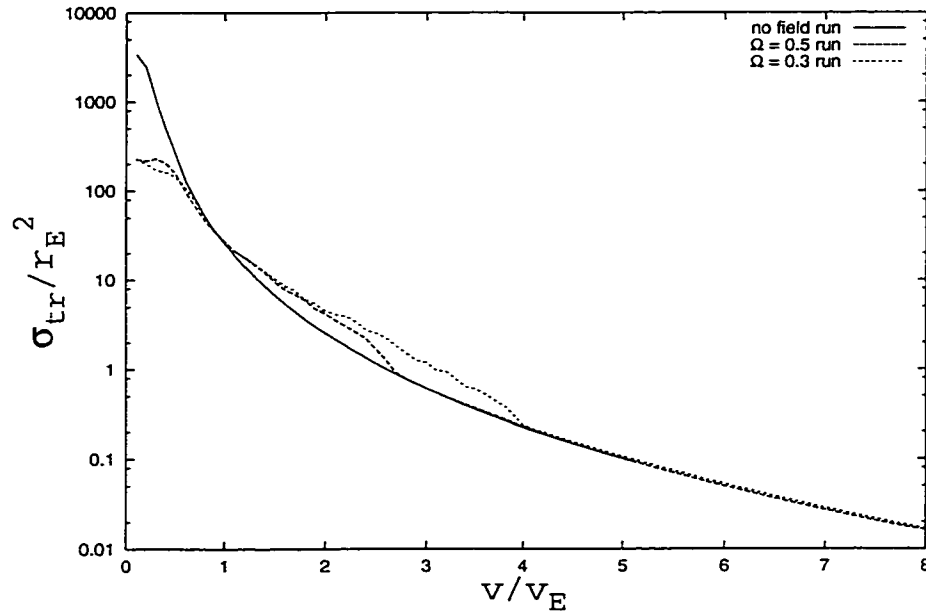


Figure 3.2: The resulting transport cross section for parallel launching schemes and the no field case.

Before going any further it is important to illustrate just how this particular case conformed to the resulting output of the simulations. Fig. (3.2) shows the transport cross section as calculated by the code (in accordance with Eq. (3.6)). Here, the solid line represents the case where the collisions were simulated in the

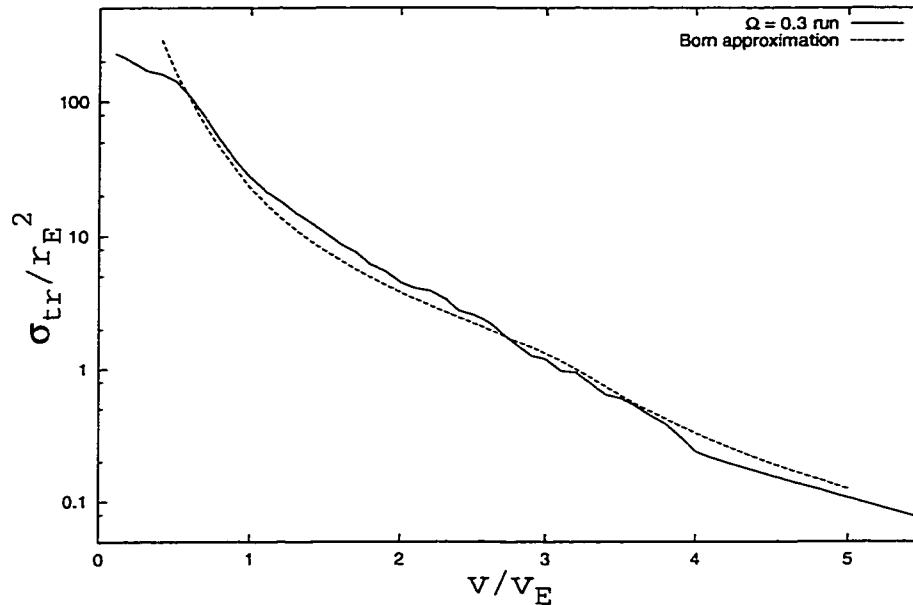


Figure 3.3: An example of how our simulation conformed to Shvets' analytical result in 3.16. There are deviations of up to 50 percent.

absence of the external field. The other two runs correspond to different field intensities, one at 10^{16} W/cm^2 ($\Omega = 0.5$) and the established upper limit of 10^{17} W/cm^2 ($\Omega = 0.3$). If one recalls Eq.(2.5) which relates v_E to v_{osc} , it becomes apparent that for velocities on the order of v_{osc} the transport cross section displays a considerable increase as compared to that from the Rutherford case. As is also apparent, the deviation grows with increasing intensity. In the limit of high velocity, σ_{tr} reduces to the classical case, for all values of laser intensity.

Fig.(3.3) presents the more visibly apparent deviation from the classical curve in the case of $\Omega = 0.3$. We observe a maximum deviation of approximately 50 percent between our results and Eq.(3.16).

Decker *et al.* [8] have suggested that the collision frequency would experience an increase from the analytically obtained Dawson-Oberman model due to multiple (or correlated) collisions of the test electron with the same scattering

ion. The correction factor is roughly the number of oscillations an electron makes while passing the domain of interaction, found to be $C \approx \omega_0/\omega_p$. [8].

Shvets *et al.* however refute this proposal citing that Eq.(3.16) taken in the limit of small velocities does not display this increased behavior. They note that Decker *et al.* are correct in their assumption that the electron will repeatedly pass the ion, however there had been no account for the factor that the time of interaction will be decreased. Analytically, the increase can be accounted for by the behavior of the Bessel functions in Eq.(3.16) ($J_n^2(\frac{n}{\Omega v})$ achieve their maxima for $v \approx 1$). Physically, Shvets *et al.* argue that the increase in the collision frequency results from the stagnation points where the total speed of the electron is zero. When $v \approx v_{osc}$ one can predict that for specific phases of the laser field the time an electron spends inside of the interaction sphere will increase dramatically should such a stagnation point (or multiples thereof) occur inside the sphere. This argument is further supported by the restriction that this increase in collision frequency can only occur for a parallel orientation between the electron's initial drift velocity and the electric field. As I shall show below, there is actually a decrease in collision frequency for a perpendicular orientation.

It is clear from Fig.(2.5) that such behavior is resolved by our simulations. It is however worth noting that in particular cases (small impact parameters for example,) these stagnation points can give rise to a substantial increase in scattering angle, violating the small angle collision assumption. The result obtained in Fig.(2.4) provide a proof of this violation since the parallel field induces a large angle scattering effect.

The deviation between the curves in Fig.(3.3) suggests that the Born approximation and small angle scattering assumptions are violated in this problem.

3.3 The Case of the Perpendicular Launch

As mentioned above, the particular case of the parallel launch orientation is unique and does not describe the full picture when one is interested in observing the macroscopic effects of a laser field interaction with a plasma. This was only one of an infinite number of possible orientations. Before going on to observe the net effects from all orientations, the next logical step is to consider the launch where the field is oriented perpendicular to the launch velocity.

There are many possible conditions under which the dipole field can be oriented perpendicular to an electron launched parallel to the z axis. The field direction (defined by \vec{n}) must lie in the x - y plane. Because the technique we have adopted launches the electrons from an x - y planar grid we immediately introduce here the first phase of the averaging procedure. If we define angle θ_1 as seen in Fig.(3.1) to be the angle between \vec{n} and the z axis then the field's orientation with respect to the x - y plane is irrelevant. Consider a dipole field oriented along the y axis ($\vec{n} = \vec{e}_y$). Then consider two separate particles to be launched from our launching grid, one on the y axis, the other on the x axis, both with the same resulting impact parameter. Both particles experience a field orientation perpendicular to their drift motion, however the electron launched from the y axis will oscillate in such a manner that it can drop deeper into the interaction sphere or further away depending on its initial phase offset. The other electron, will only oscillate perpendicular to the scattering plane during its collision. It should then be apparent that an orientation with $\vec{n} = \vec{e}_x$ would simply switch the behavior of these particles. Such a reflection of properties would then lead to the conclusion that for a grid of incident particles any single orientation in the x - y plane of the dipole field will result in an average of behaviors for particles launched along a particular arbitrary axis. This then is the argument for simply placing the perpendicular component of of the dipole field only along the y

axis. For future purposes the angle θ_1 will be used to describe field orientations between the parallel and perpendicular case, but for this section one can simply assume that $\theta_1 = \pi/2$.

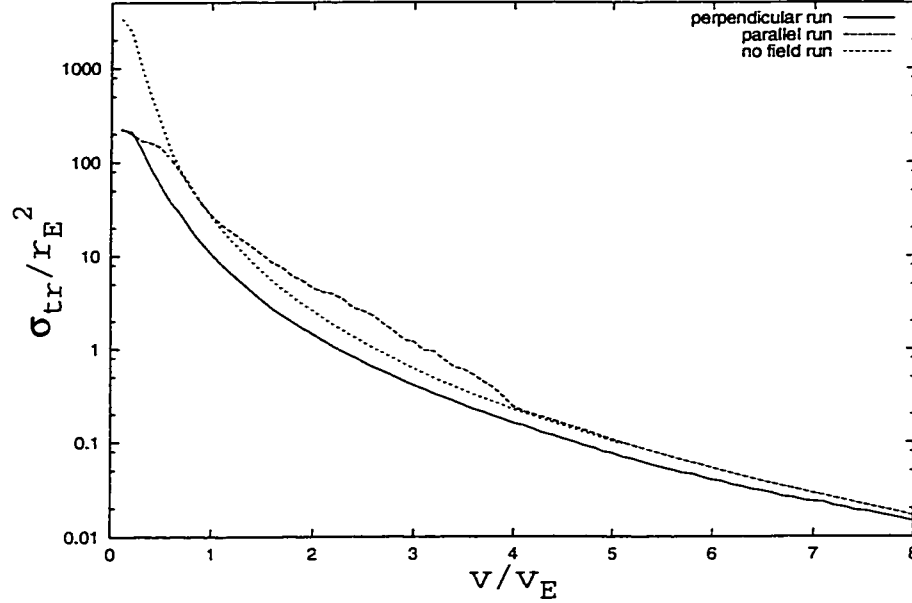


Figure 3.4: A decrease in the transport cross section when the dipole field is aligned perpendicular to the initial launch velocity. Note that this is in contrast with the increase observed about v_{osc} for the parallel launch case. This figure depicts trials with the dimensionless frequency set at $\Omega = 0.3$.

I have included in Fig.(3.4) the resulting transport cross sections for both parallel ($\theta_1 = 0$) and perpendicular ($\theta_1 = \pi/2$) trials with $\Omega = 0.3$ superimposed on the no field result. This case is representative of the general trend observed in the case of the perpendicular launch, i.e. the transport cross section experiences a decrease from the no field situation.

It is clear that the large angle scattering responsible for the hump in the case of the parallel launch is insignificant here. The dominant behavior is a net decrease in scattering angle. The physical reason for this reveals itself when one

considers the mechanics of the problem.

Consider the classical Rutherford scattering problem for an electron and ion pair without the external field. It is well known that the scattering angle is predicted by the relation

$$\cot\left(\frac{\phi}{2}\right) = \rho v^2, \quad (3.17)$$

in our normalized units. Thus we can see that as the impact parameter ρ increases, the scattering angle ϕ decreases.

At the fundamental level, the application of the dipole field causes a deviation from the classical case by altering two aspects of the problem: the impact parameter and the time for the collision. By examining how the field affects the impact parameter alone, we can develop a qualitative understanding for the reduction in the scattering angle.

Consider the collision depicted in Figs.(2.2) and (2.3) where the laser field is aligned along the y axis, perpendicular to the drift velocity of the particle. Now recall that we are not interested in the behavior of such a particular collision, but the behavior of all such collisions when averaged over the incident phase of the laser field. Although the deviation from the drift coordinates due to the external field is small (as this particular example illustrates a low intensity run), after averaging over all incident field phases, the impact parameter is greater than 2ρ . The oscillations from the laser field increase the average distance of the electron from the z axis thus creating an effectively larger impact parameter ρ' . When the electron and field are set up as in this case, the new impact parameter could be expressed as

$$\rho' = \sqrt{\rho^2 + \left(\frac{2}{\pi\Omega^2}\right)^2}. \quad (3.18)$$

Note here that the new term is simply the average distance added in the x direction due to the r_{osc} term in our normalized notation. If this term were to be inserted into Eq.(3.17), one can then see how the scattering angle would

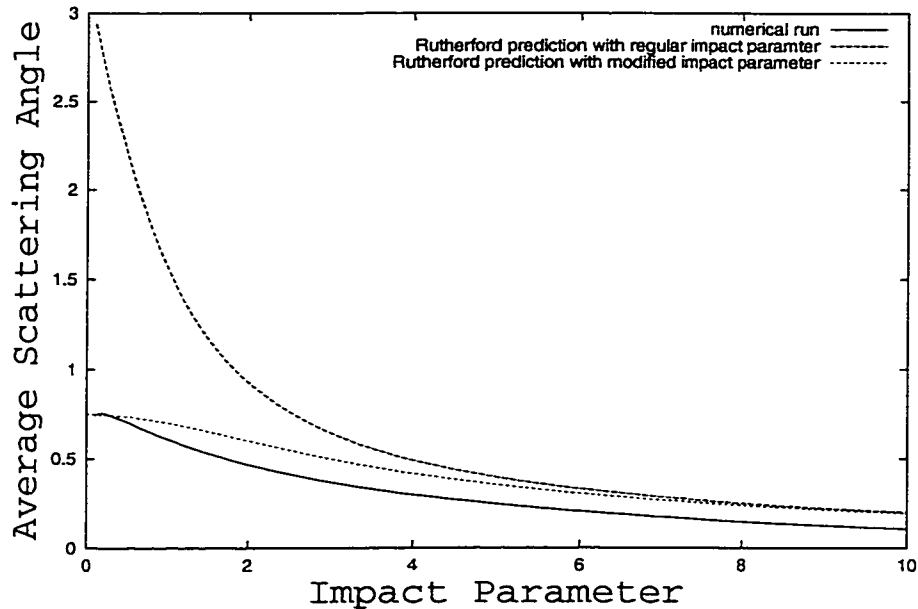


Figure 3.5: This graph illustrates an example of the observed average scattering angle as a function of impact parameter for a field orientation similar to that discussed in figure 2.2. This particular case considered only particles with an incident drift velocity of v_E . Note how the simple assumption of the modified impact parameter greatly reduces the predicted scattering angle.

decrease. Naturally this result is an oversimplification. I have yet to account for the contribution of v_{osc} to the picture although I believe that because the particle's speed is at a maximum when the additional distance is at a minimum, this would only increase the effective impact parameter, further decreasing the scattering angle.

Fig.(3.5) depicts a specific example of how the modified impact parameter in Eq.(3.18) establishes a better prediction for the average scattering angle. This case specifically examined particles with an initial velocity of v_E with a dimensionless frequency of $\Omega = 0.5$. Note that in this case the particles were launched from a point on the x axis only with the dipole field aligned perpendicular, along

the y axis. This clearly illustrates the reduction in scattering angle compared to the classical prediction.

To complete the discussion of the perpendicular field alignment we must now account for all the possible field orientations in the xy plane that are mutually perpendicular to the launch. Obviously by rotating the field in this direction the extra dimension to the effective impact parameter above will be reduced, however, it will still remain larger than that predicted in the classical case. It could be further argued that this process would involve averaging over these orientations introducing another $\frac{2}{\pi}$ factor to the additional dimension. Pursuit of this however is simply meant to provide an element of quantity to a qualitative description. To fully consider what occurs two extremes need to be discussed.

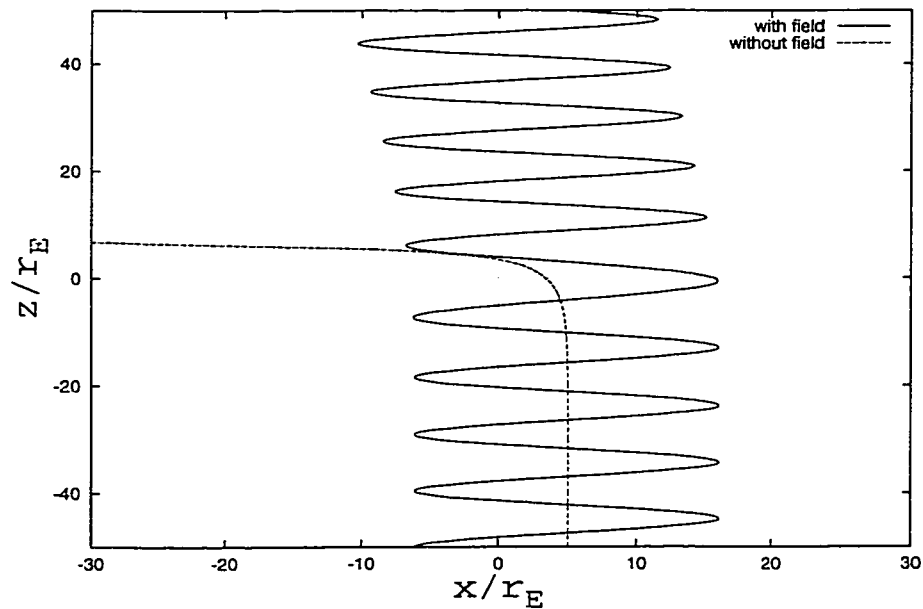


Figure 3.6: This is an example of an event where the amplitude of oscillation (defined by $\Omega = 0.3$ is greater than the impact parameter itself at $5r_E$. Thus for specific initial phases of the field, there is a significant probability that the electron will only experience a minimal deflection, effectively “missing” the ion.

The first of which can be thought of as an extension of the impact parameter argument. If we investigate larger Ω values that still lie within our established physical parameters, the radius of oscillation can actually grow larger than the impact parameter itself. When this happens events can occur where the electron almost entirely misses the ion, experiencing only a very small deflection from its drift path. In Fig.(3.6) I have launched the particle with an impact parameter of $5r_E$ and given it an initial velocity of $0.5v_E$ inside of a field characterized with $\Omega = 0.3$. The Rutherford result, obtained by turning off the field shows a very sharp scattering event, however with the application of the field, an electron under the same initial conditions experiences only a very minor relative perturbation in its trajectory.

However, it is also apparent that when the field is oriented along the same line that connects the initial position of the particle and the z axis, the oscillations average to the initial classical impact parameter. However, just as there exists a possibility of missing the ion, such an orientation permits the possibility of an interaction such as the one defined in Fig.(3.7).

Here I have included a diagram of a collision that occurred with the same parameters as those outline for Fig.(3.6) only the initial phase of the field has been displaced by a factor of $\pi/2$. Obviously such events can lead to another case of large angle scattering. It should be noted however that for such an event to occur a specific alignment of the field is required and so when averaging over all possible cases, such an event is relatively improbable.

Thus going back to Fig.(3.5) it is apparent that the dominant behavior for the perpendicular launch is described by collisions where the field has increased the effective impact parameter, decreased the time of interaction, and in extreme cases resulting in a significant portion of electrons practically missing the ion. Obviously this behavior decreases with decreasing field intensity. For example

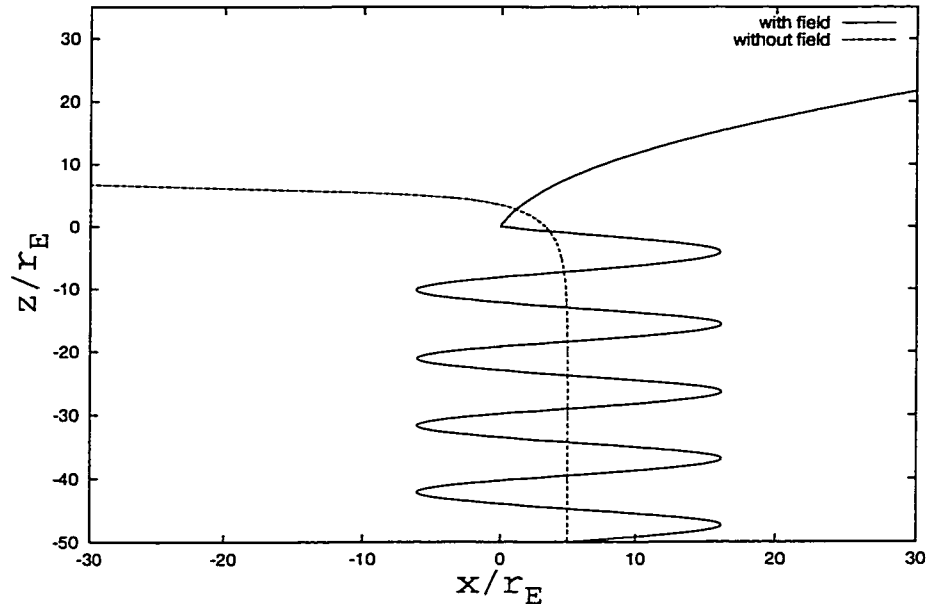


Figure 3.7: Just as the oscillations from the field can cause the electron to miss the ion, the case also exists where the electron can be thrust straight towards the ion. The parameters here are exactly the same as those outlined for figure 3.6 with the field offset by $\pi/2$.

as the value of Ω gets larger (recalling the no field case is given by $\Omega = \infty$), the second term in the square root in equation 3.18 goes to zero. Hence the reasoning for the decrease in scattering angle disappears and leaves us with the classical Rutherford scattering case.

3.4 Large Angle Contribution

As mentioned above one factor in this work that separates it from standard investigations is the fact that it allows for large angle scattering to occur, thus eliminating any errors that arise from the assumption that the system is dominated by small angle collisions. A plot of the transport cross section as it is

evaluated over different values of Ω is presented below. However, before I go into detail about the observed cross section itself, the statistical contribution of the large angle scattering particles to the transport cross section should be addressed. For the sake of argument I shall assume that a “large” angle is any scattering angle greater than $\frac{\pi}{3}$.

Fig.(3.8) provides two examples of the transport cross section evaluated for $\Omega = 0.25$, with field orientations of $\theta_1 = 0$, and $\frac{3\pi}{10}$ respectively. Superimposed on these, are the cross sections as calculated using only the electrons that scattered at angle larger than $\frac{\pi}{3}$. Noting that in the above example the scale is logarithmic, it remains apparent that for velocities below ν_{osc} the contribution from such electrons is very large. In the parallel cases it was often as much as fifty percent or more. The contribution was seen to drop off rapidly however at higher drift velocities.

3.5 Transport Cross Section

Now that we have discussed both the straight forward cases of the parallel and perpendicular launches, the discussion of the electron ion collisions needs to be extended to the general case where the resulting transport cross section is found after averaging over all possible orientations of the the field. As outlined in the preceding section, with our grid launch system the need to average over field orientations in the xy plane has already been gratified. Thus in order to complete the averaging procedure we consider a series of five steps in θ_1 . Here the field is increased from $\theta_1 = 0$ (the parallel launch case) to $\theta_1 = \frac{\pi}{2}$ (the perpendicular case) in steps of $\frac{\pi}{10}$. Then the transport cross section returned is averaged over all such cases.

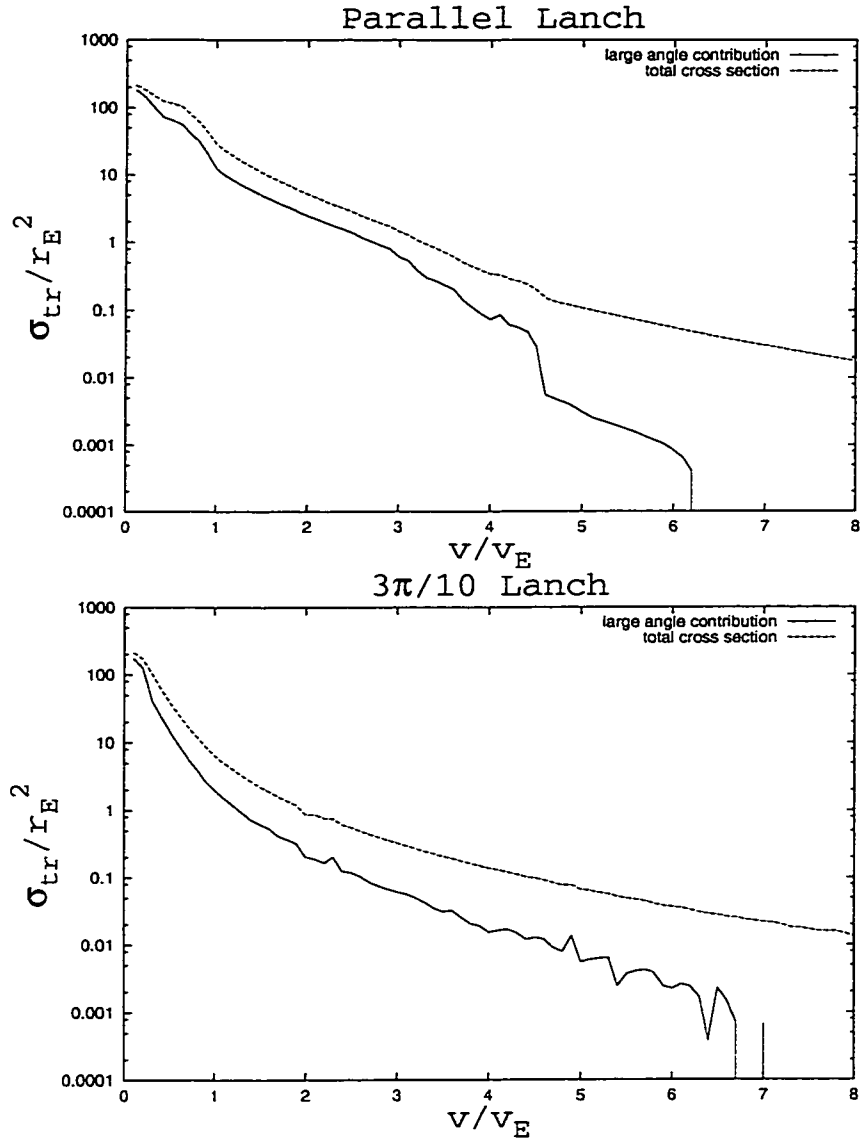


Figure 3.8: The transport cross section as calculated for a parallel launch (above) and where the field is oriented at an angle of $\frac{3\pi}{10}$ (below). The contribution from large angle electrons is given by the solid lines. For velocities lower than ν_{osc} ($4\nu_E$ in these examples) the large angle electrons make a significant contribution to the transport cross section. The significance is strongest in the parallel launch case.

$$\sigma_{tr}(v) = \int_0^{\frac{\pi}{2}} \int_{-\rho_{max}}^{\rho_{max}} \int_{-\rho_{max}}^{\rho_{max}} \langle 1 - \cos\phi \rangle dx dy \sin(\theta_1) d\theta_1 \quad (3.19)$$

Because of its importance in the formulation of the particle-in-cell scattering algorithm, any deviation in the transport cross section from the established Rutherford model (used in the previous chapter) will have significant consequences on the resulting heating rate. Therefore it is imperative that we use the information from this study to develop an expression for this cross section and hence the electron ion collision frequency as a function of both velocity and the field frequency and intensity as contained in Ω .

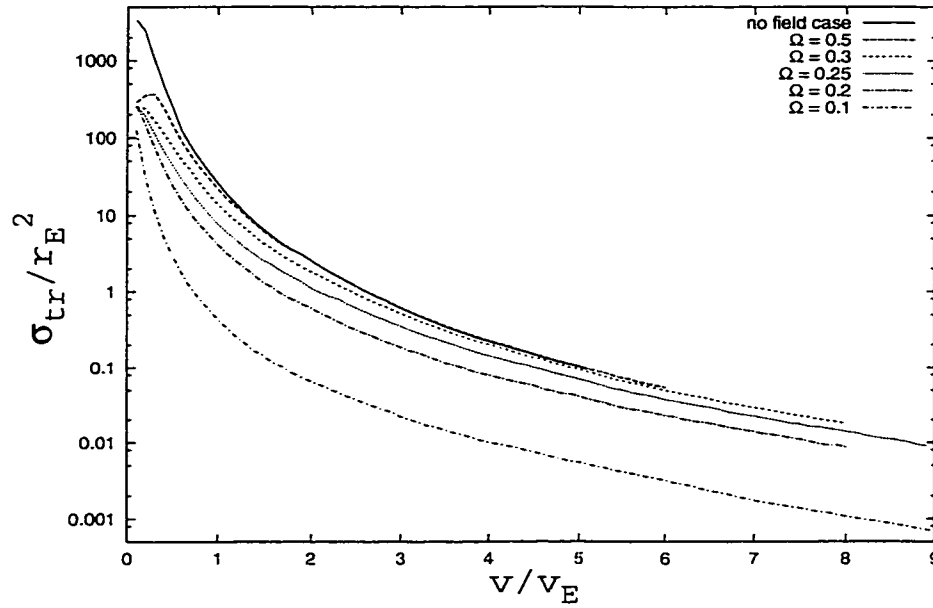


Figure 3.9: A series of curves plotting the transport cross section as a function of velocity. Recall that our dimensionless frequency Ω is defined such that intensity goes to infinity as Ω goes to zero. Thus it is apparent that there is a decrease in the transport cross section for increasing laser intensity.

Fig.(3.9) graphs the resulting cross sections as evolved for cases of $\Omega = 0.5$, 0.3, 0.25, 0.2, 0.1 and the case of no field. It is apparent that for increasing

intensities the transport cross section decreases and therefore we wish to establish an analytical fit to these points that incorporates the Ω parameter.

We know that as the field establish drops to zero, and as the test electron's velocity becomes much greater than is oscillatory velocity ($v \gg v_{osc}$), the expression for the transport cross section must reduce to that given in Eq.(3.11).

$$\sigma_{tr}(v) = \frac{4\pi}{v^4} \ln(1 + 5v^2). \quad (3.20)$$

Further Fraiman *et al.* [12] proposed a modification to this expression of the form

$$\sigma_{tr}(v, \Omega) = \frac{4\pi \ln(1 + 5v^2)}{v^2(v^2 + \Delta(v, \Omega))}, \quad (3.21)$$

where $\Delta(v, \Omega)$ is the correction term essential when $v \leq \Omega$. It appeared that Fraiman left out the logarithmic factor in this expression. After numerous attempts at fitting different forms to the curve, most of which involved adding a subsequent term to the right hand side of expression 3.20 or insertion of a term into the logarithm, it was found that equation 3.21 held the best form to fit the curves in Fig.(3.9).

The big step was to determine the form of $\Delta(v, \Omega)$. Starting with the obvious knowledge of the behavior in the limits, we proposed a several different logical forms. In the end the best fit to the curves was given by

$$\Delta(v, \Omega) = \alpha(\Omega)v^{\beta(\Omega)} \left[\frac{\frac{1}{\Omega^4}}{\frac{1}{\Omega^2} + v^2} \right]. \quad (3.22)$$

The coefficients $\alpha(\Omega)$ and $\beta(\Omega)$ were then determined specifically by an analysis of data points. A method of least squares iteration program was used to evaluate the coefficients that yielded the best possible fit. We were successful in producing five points in addition to the no field situation on which to propose possible expressions for these coefficients. The data points available are given below.

Ω	$\alpha(\Omega)$	$\beta(\Omega)$
0.10	0.382	1.900
0.20	0.182	1.688
0.25	0.124	1.545
0.30	0.060	1.350
0.50	0.008	1.100

Table 3.1: The coefficients found that gave the best fit approximation to the curve transport cross section curve.

These points were analyzed and found to conform to the following two expressions.

$$\alpha(\Omega) = 1.21e^{-9.89\Omega} \quad (3.23)$$

$$\beta(\Omega) = 2.00e^{-0.706\Omega^2 - 0.8744\Omega} \quad (3.24)$$

For a sixth point we can also observe the known behavior of the classical no field case. Because both α and β are decaying terms with increasing Ω and the boxed term in Eq.(3.22) falls off as $\frac{1}{\Omega^2}$ we see that the $\Delta(v, \Omega)$ term vanishes in the limit of $\Omega \rightarrow \infty$. Further, for $v \gg v_{osc}$ the $\Delta(v, \Omega)$ term vanishes, as even for an Ω value of zero the β term approaches 2 from below.

For application in the particle code later on it will be necessary to write Eq.(3.21) without the Keplerian velocity. It is impractical to get rid of the dimensionless frequency Ω , but to this end the equation can be written in the form

$$\sigma_{tr}(v, \Omega) = \frac{\sigma_R}{\left(1 + \alpha(\Omega) \left[\frac{v}{\Omega v_{osc}}\right]^{\beta(\Omega)-2} \left[\frac{v_{osc}^2}{\Omega^2(v_{osc}^2 + v^2)}\right]\right)}, \quad (3.25)$$

where v and v_{osc} have dimensions of velocity. Here σ_R is the Rutherford cross section while $\alpha(\Omega)$ and $\beta(\Omega)$ have the same form as above, and one can recall that the dimensionless frequency is given by equation 2.7

$$\Omega = \frac{\omega_0}{\omega_E} = \omega_0 \left(\frac{rn^2 Z}{eE^3} \right)^{\frac{1}{4}}.$$

To confirm the validity of this expression we observe that the Rutherford expression is recovered in the limit as Ω goes to infinity (field intensity drops to zero).

$$\sigma_{tr}(v, \Omega \rightarrow \infty) = \frac{A \ln(1 + k_{max} \rho_{max})}{v^4} \quad (3.26)$$

We can further extrapolate this data and gain insight as to how the cross section behaves at even larger intensities by allowing Ω to drop to zero. It should be noted however that as Ω drops below 0.1, v_{osc} becomes relativistic and thus this classical model breaks down. There is also the binary collision limit problem discussed earlier which also forces the model to break down at this point. However, it is important to note that we recover an expression in the high field limit that scales like $\frac{v_{osc}^2}{v_E^2}$ which corresponds to $I^{3/4}$.

$$\sigma_{tr}(v, \Omega \rightarrow \infty) = \frac{A \ln(1 + k_{max} \rho_{max})}{v^4 \frac{v_{osc}^2}{v_E^2}} \quad (3.27)$$

To conclude this chapter I have included the results of this curve fitted onto our original data sets as shown in Figs.(3.10) through (3.14)). The resulting expression returns curves consistent to within a 10 percent deviation from the data.

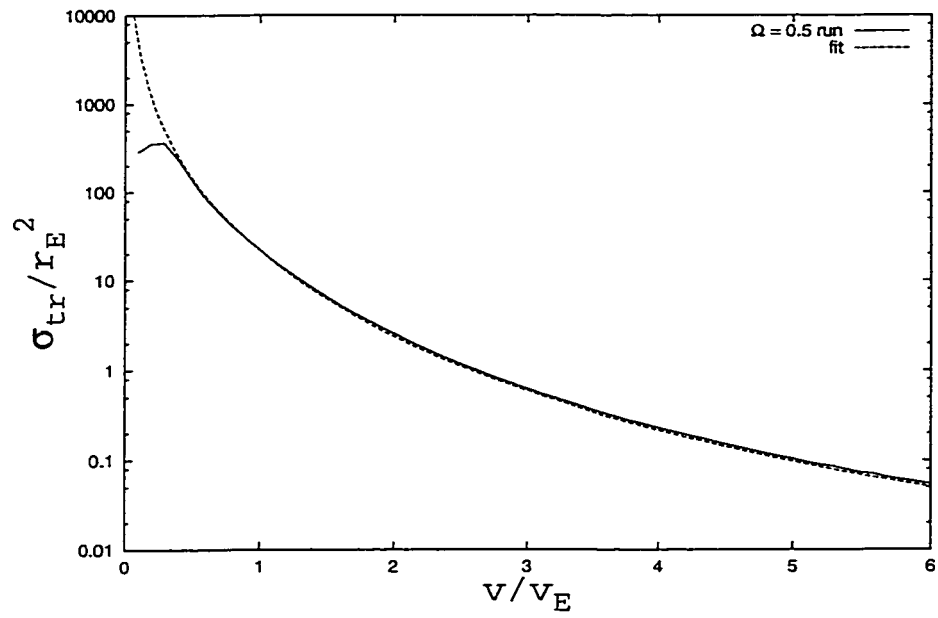


Figure 3.10: Fit for the $\Omega = 0.5$ run.

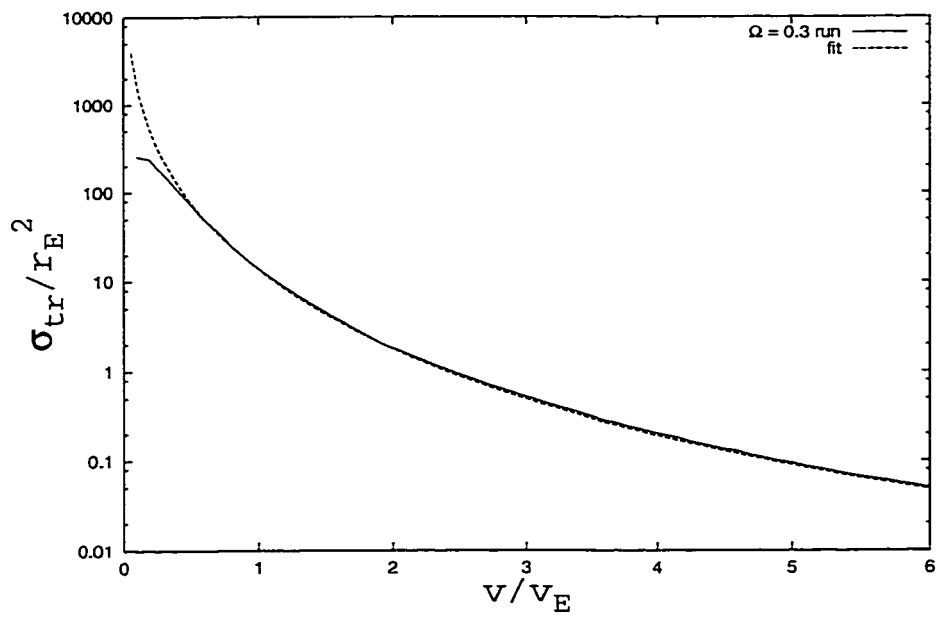


Figure 3.11: Fit for the $\Omega = 0.3$ run.

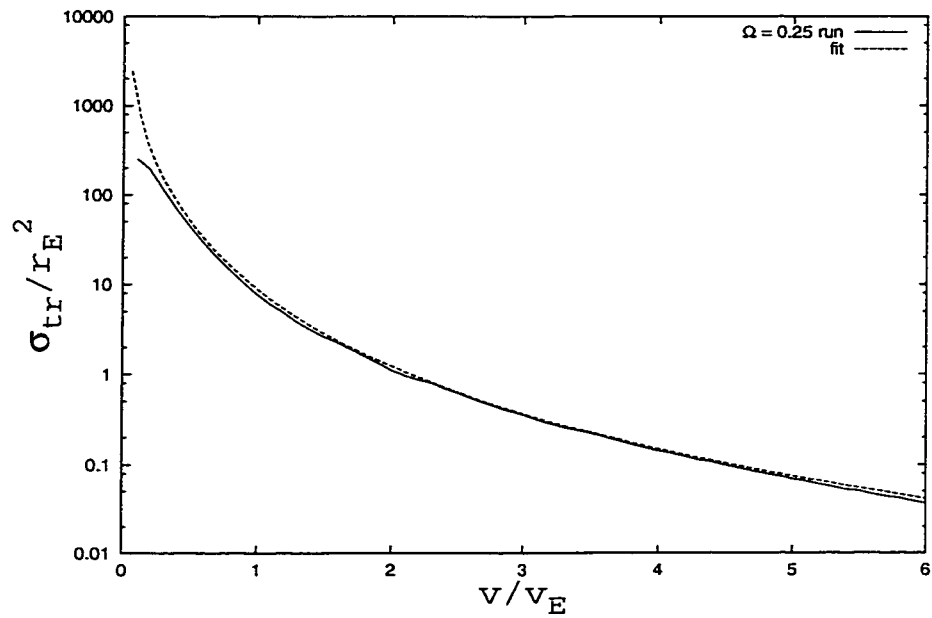


Figure 3.12: Fit for the $\Omega = 0.25$ run.

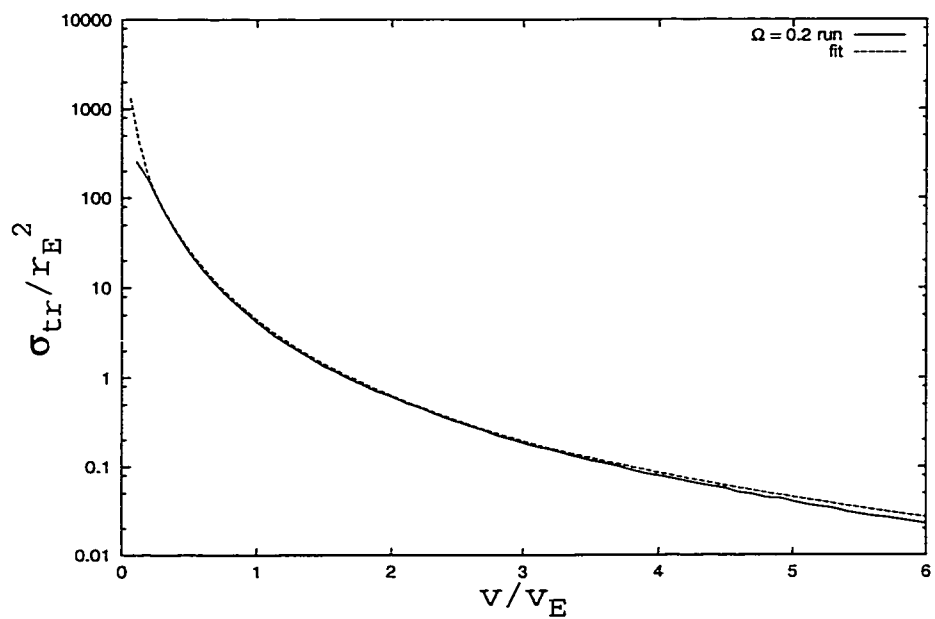
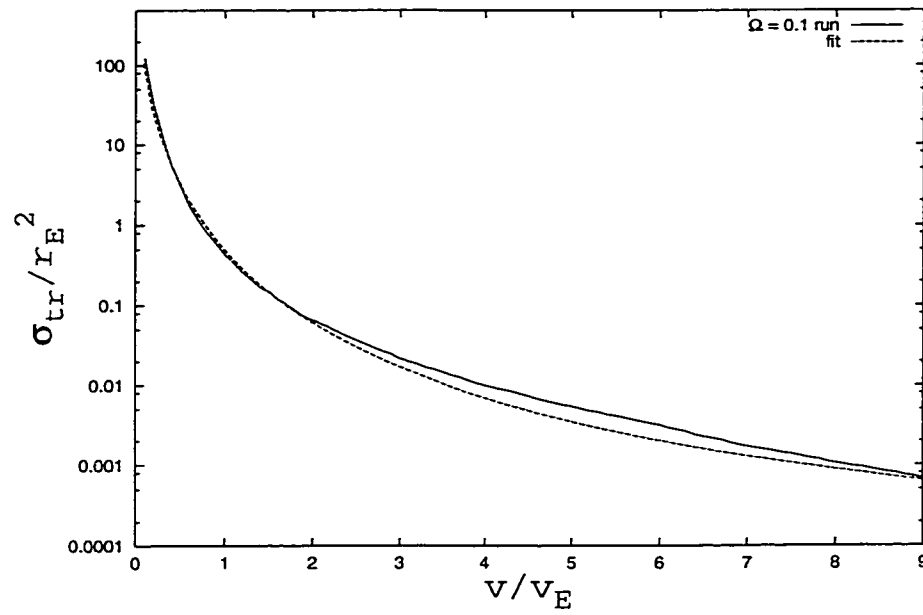


Figure 3.13: Fit for the $\Omega = 0.2$ run.

Figure 3.14: Fit for the $\Omega = 0.1$ run.

Chapter 4

Effective Cross Section

4.1 Energy Conservation

The newly presented model for the transport cross section is used in the definition of the collision operator in the kinetic particle code presented in chapter 5. Therefore, our new theory of the cross section modifies all collisional processes, including inverse bremsstrahlung (IB) heating of electrons. In order to verify the results of particle code simulations we will examine the energy gained on the microscopic level due to inelastic electron-ion collisions.

Consider a change in the energy over time of the external field in a physically small volume. This will result in a change of the average drift kinetic energy of the electrons which can be described as

$$\frac{\partial \langle \epsilon \rangle}{\partial t} = \frac{1}{2} m v_{osc}^2 n_e \nu_{ei}, \quad (4.1)$$

where ν_{ei} is the electron ion collision frequency and again the angled brackets indicate an average over the oscillating field. The collision frequency is then related to the effective cross section by

$$\nu_{ei} = \sigma_{eff} n_i v_{in}, \quad (4.2)$$

where v_{in} is the initial drift velocity of the electron and n_i is the ion density. The electrons gain an average energy during the e-i scattering process only [12], thus

$$\frac{1}{2}mv_{osc}^2 n_e \nu_{ei} = n_i v_{in} n_e \frac{1}{2} m \int_{-\infty}^{\infty} \langle v_{out}^2 - v_{in}^2 \rangle d^2 \rho. \quad (4.3)$$

where v_{out} is the electron's drift velocity after the collision. Combining Eqs.(4.2) and (4.3) gives a definition for the effective cross section,

$$\sigma_{eff}(v) = \int_{-\infty}^{\infty} \frac{2}{v_{osc}^2} \langle v_{out}^2 - v_{in}^2 \rangle d^2 \rho. \quad (4.4)$$

The factor of 2 is included in order to be consistent with the definition proposed by Fraiman *et al.* [12].

First we check the numerical accuracy of our code for the classical Rutherford scattering case. It is well known that in the absence of a laser field, an electron scattering off an ion must have the same kinetic energy before and after the collision. The results of this test are outlined in Fig.(4.1).

As this figure indicates, we are only concerned with the kinetic energy difference before (in) and after (out) the collision and are measured outside the interaction sphere. To investigate the no field case we decreased the intensity of the field by setting $\Omega = 20000$ so that its effects on the collision would be insignificant. The errors show a maximum divergence of 1.3×10^{-5} (normalized to v_{in}^2 which is on the order of 1.) The increasing deviation can be attributed to the structure of the algorithm. The system stops analyzing an event after the electron's spatial drift coordinate is found to be greater than its original drift coordinate as measured radially from the scattering centre. At higher velocities the displacement is subject to larger variation because the time step remains constant. A reduced time step at high velocities would solve this problem. Although the error is insignificant compared to the minimum energy variation we will proceed with $\Delta t = 0.05/\omega_E$ outside of the interaction sphere and reduce this

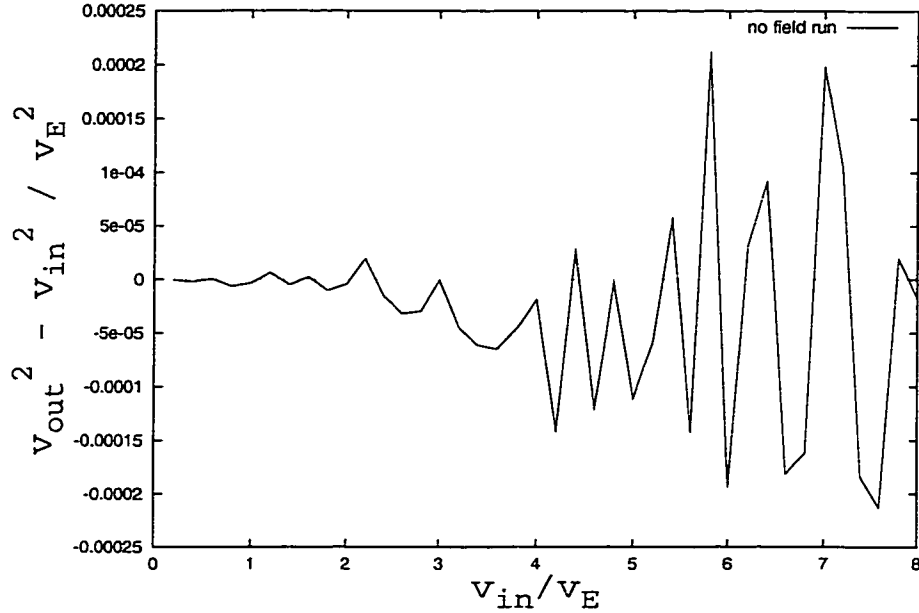


Figure 4.1: The result of a run where the laser field was turned off and the energy difference before and after the collision was measured over the velocity range we investigated. The increasing fluctuations with velocity are due to the relatively large, time step assumed in the algorithm. The velocities in each case are normalized to v_E which set small enough that the effects of the field are inconsequential.

to $\Delta t = 0.001/\omega_E$ for the radial drift coordinate $r(t) = 50.0 \pm 1.0r_E$. Therefore the algorithm conserves energy in the no field scenario.

4.2 Inverse Bremsstrahlung Heating

The role of various laser absorption mechanisms remains a crucial issue in all laser pulse interaction experiments. Our theory allows for an investigation into inverse bremsstrahlung (IB) heating at high laser intensities. For the case of weak laser fields where $v_{osc} \ll v_{th}$, the IB heating rate is well known [21, 31].

Then Eq. (4.1) reduces to

$$\frac{\partial \langle \epsilon \rangle}{\partial t} = KI, \quad (4.5)$$

which relates the rate of change in energy per unit volume (ϵ) to the laser intensity I , with

$$K = \frac{\omega_p^2 \nu_{ei}}{c \omega_0^2}. \quad (4.6)$$

Here ω_p is the plasma frequency. The electron-ion collision frequency is given by

$$\nu_{ei} = \frac{4\sqrt{2\pi}}{3} \frac{Z^2 e^4 n_i \ln \Lambda}{m^2 v_{th}^3}, \quad (4.7)$$

where again $\ln \Lambda$ is the Coulomb logarithm and $v_{th} = \sqrt{T/m}$ is the thermal velocity.

It has been suggested by Vick [23] that the treatment of the problem in the high intensity regime is to express the dependence of the collision frequency on a parameter $u = v_{osc}/v_{th}$ as a multiplier which can be applied to the weak field result

$$\nu_{ei}^u = g(u) \nu_{ei}. \quad (4.8)$$

I shall later illustrate how the results of this study compare to some of the predictions for $g(u)$.

The tests here begin with a system similar to that outlined for the transport cross section. The difference being that here, the outcome of each collision reports a value for output kinetic energy of the electron which is in turn inserted into Eq.(4.4.) The averaging process is the same as that outlined for the transport cross section. The only exception being that in order to average over the initial phase of the electric field, the number of points used was increased from sixty at lower velocities ($v < v_{osc}$) to one thousand for those in the higher range.

The output velocity (v_{out}) is calculated in the following manner. The launch coordinates of the electron are recorded at $t = 0$ and used to calculate the radial starting distance (R_{st}) from the ion. We set this at $R_{st} \approx 50r_E$. After the

electron travels through its trajectory, its final velocity is recorded when its drift coordinates again place it at R_{st} . Note that the drift coordinates do not include the displacement due to the oscillation from the laser field. Because the launching grid is planar and not spherical, R_{st} varies up to a maximum of two percent for each run. The value of R_{st} is established much larger than the Debye length cut off range of the ionic potential.

This microscopic study allows us to observe the mechanism by which the electron gains energy in the presence of a strong laser field. The electron enters the ionic field while the laser field holds a particular phase. The electrons that experience some degree of the trapping outlined in chapter 2 would then not feel the effects from the electric field as their trajectories are dominated by the field from the ion. Such electrons emerge from the ionic field while the laser field is in a different phase and exerting a larger force on the electron. In fact often the condition of a laser field phase giving the electron a higher kinetic energy is a condition required for the electron to escape. Thus the electron emerges with a higher energy level, accounting for the energy gain in the free - free transition.

4.3 Results

As with the transport cross section, runs were performed for five different orientations of the field corresponding to $\theta_1 = n\pi/10$ where $n = 1..5$. (Recall that θ_1 is defined as the angle between the initial launch velocity $v_{in}^{\vec{}}$ which lies along the z axis and the laser field polarization vector $E\vec{n}$).

The dependence of the effective cross section on the angle of laser field polarization for a run with $v/v_E = 2$ and $\Omega = 0.5$ is shown in Fig.(4.2). Note that the line depicted here actually shows ten points to present an idea of the variance in energy difference across the angles studied. For some of the smaller

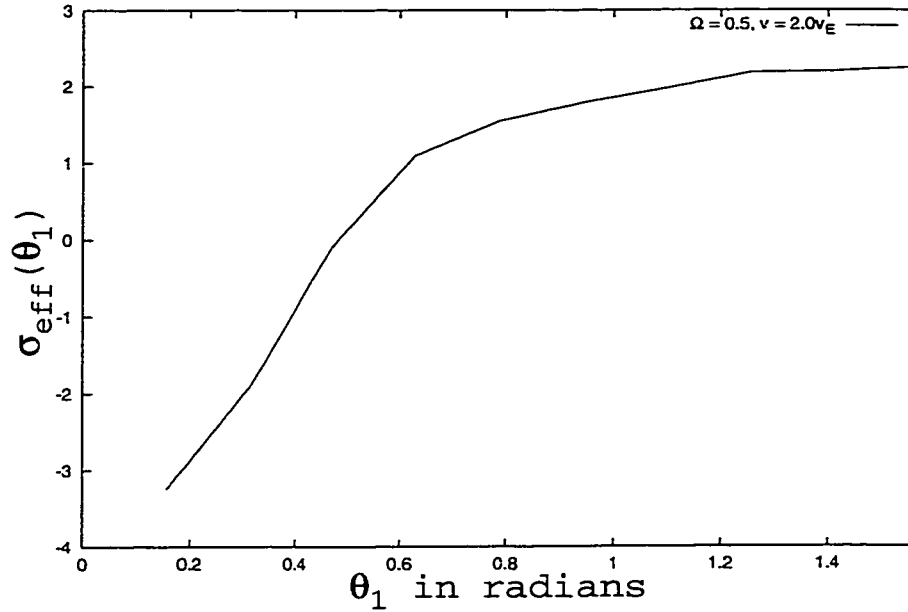


Figure 4.2: As the angle between the drift launch velocity and the polarized field increases from the parallel launch condition, a negative energy gain region is observed for small values of the angle confirming the reports of Fraiman *et al.* [12]. This negative region was generally observed as v approached v_{osc} .

angles (those close to the parallel launch case) there does in fact exist a region of negative energy gain. However, after averaging over θ_1 , the effective cross section always ends up positive. What this does present however, is an averaging problem. At this time it was only feasible to perform these calculations based on the results of five angles and therefore care was taken that each angle was averaged over enough phase points to ensure that the results were accurate. Because there is a region where these points approach zero it is feasible that small numerical discrepancies can influence the output results. However the angles were weighted with a $\sin \theta_1$ probability distribution accounting for the three dimensional nature of the angle orientations. Thus the influence of the negative energy gain region is not as significant as it may at first appear. It should also be noted that this

negative energy gain region confirms the observations presented by Fraiman *et al.* [13].

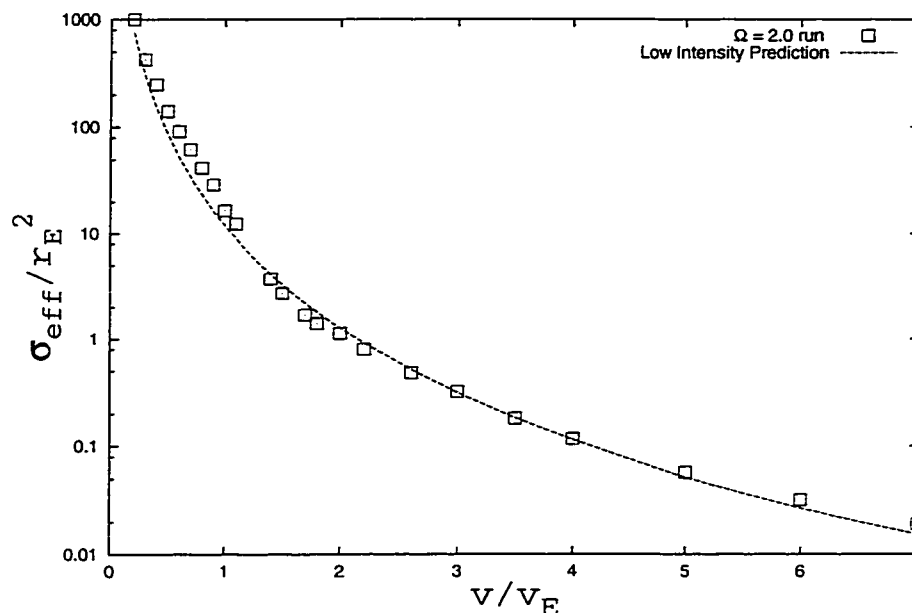


Figure 4.3: The resulting effective cross section for a run with $\Omega = 2.0$.

We next predict the low field behaviour of the effective cross section. Fig.(4.3) shows the results of the $\Omega = 2.0$ run which corresponds to a laser intensity of $2.25 \times 10^{14} W/cm^2$ after they have been averaged over all five orientations of the laser field. A good approximation for these results is found when Eq.(4.7) is combined with Eq.(4.2). If the thermal velocity is then replaced with the drift velocity and we transform into our Keplerian coordinates we arrive at the expression

$$\sigma_{eff,L} = \frac{8\sqrt{2\pi}}{3v^4} \ln(1 + 5v^2), \quad (4.9)$$

which is shown in Fig(4.3). The factor of two increase is due to the normalization of σ_{eff} to $\frac{1}{2}v_{osc}^2$ rather than v_{osc}^2 .

To check this result against the low field result, we average it over a Maxwellian

velocity distribution,

$$\nu_{ei} = n_i v_E r_E^2 \int_0^\infty v' \frac{1}{2} \sigma_{eff}(v', \Omega = 2) \frac{v'^2}{v'_{th}{}^3} e^{-\frac{v'^2}{2v'_{th}{}^2}} dv'. \quad (4.10)$$

Here v' and v'_{th} are the initial drift and thermal velocities normalized to v_E respectively. The factor of 1/2 that precedes the effective cross section has been introduced to account for the 2 in Eq. (4.4). The integration was performed numerically on the data points. Linear extrapolations were used to fill in unknown points such that the quadrature could be performed over even intervals in dv . The resulting expression is

$$\nu_{ei} \approx 11.6 \frac{n_i Z^2 e^4}{m^2 v_{th}^3}. \quad (4.11)$$

The evaluation of Eq.(4.7) yields

$$\nu_{ei} \approx 3.3 \frac{n_i Z^2 e^4}{m^2 v_{th}^3} \ln \Lambda. \quad (4.12)$$

Thus the confirmation of our result to the low intensity run depends on the evaluation of the Coulomb logarithm. Substituting v'_{th} which holds a value of 2.03 for a 100 eV plasma into the logarithm in Eq.(4.9) results in

$$\nu_{ei} \approx 10.3 \frac{n_i Z^2 e^4}{m^2 v_{th}^3}. \quad (4.13)$$

A more careful analysis using the modification suggested by Pert [22] with $\Lambda = v_{th}/\omega_0 b_{min}$ for high frequency absorption calculations gives

$$\nu_{ei} \approx 12.9 \frac{n_i Z^2 e^4}{m^2 v_{th}^3}. \quad (4.14)$$

Comparing the coefficients shows that we are roughly within a ten percent error margin of the desired result, and therefore confirms our low field result with well known IB theory.

Consider Fig.(4.4) which details the results for the effective cross section after averaging over all angles. The individual points are superimposed on the

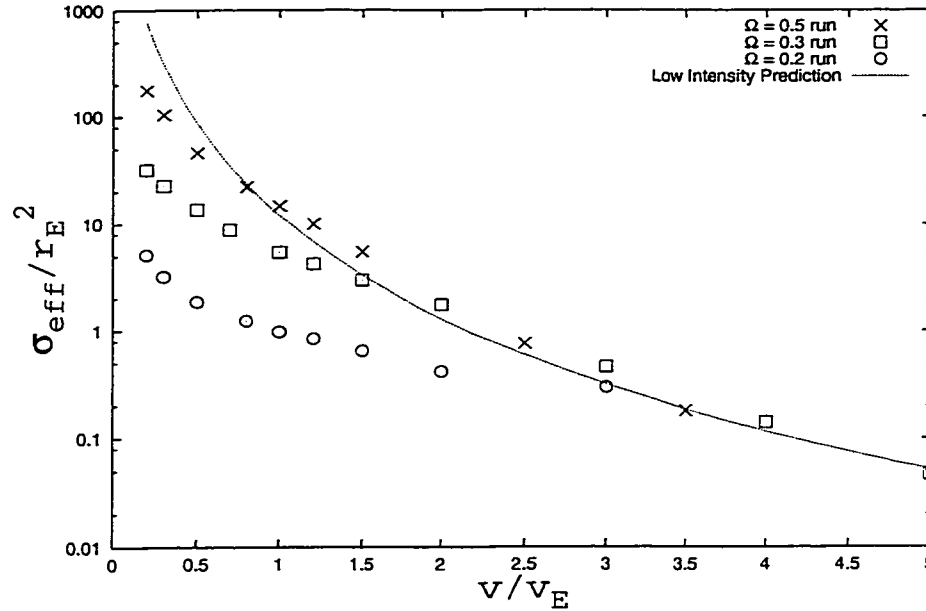


Figure 4.4: The results of the effective cross section investigation for increasing field intensities. The dotted line represents $\sigma_{eff,L}$. As can be seen there is an obvious decrease in the energy gain as the dimensionless frequency Ω (and thus intensity) is increased for low velocities.

dotted line which corresponds again to $\sigma_{eff,L}$, our fit for the low field data. The different series of points each correspond to a different laser intensity. As the dimensionless frequency was decreased (corresponding to an increase in laser intensity from $10^{16}W/cm^2$ up to $10^{17}W/cm^2$) the effective cross section clearly decreases in the region of lower velocities. One may recall that $v_{osc}/v_E = 1/\Omega$ in order to gain an idea of where these velocities lie relative to v_{osc} .

With respect to the $\Omega = 0.3$ case as an example, (the points marked with an x), it can be seen that as the velocity increased the resulting points crossed over the low field fit and indicate a brief region where the effective cross section is higher than the low field fit. The data then appears to conform with it for the highest velocities. This region of higher than expected effective cross section

values is responsible for the increase in the IB heating rate that will be apparent below.

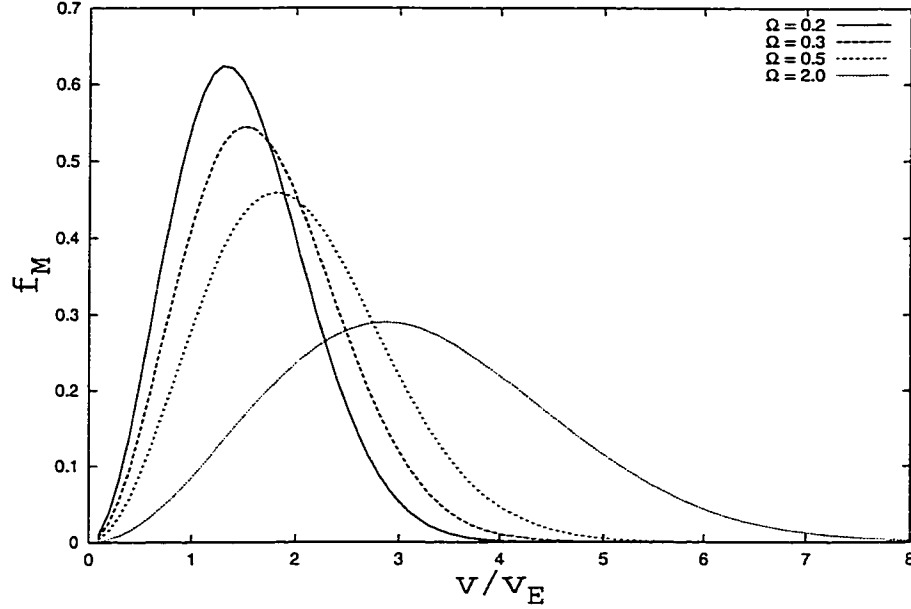


Figure 4.5: An example of a Maxwellian velocity distribution for a $T = 100\text{eV}$ plasma as it changes in our intensity dependent velocity range.

I have included Fig.(4.5) to illustrate the behavior of a Maxwellian velocity distribution $\frac{4\pi}{2\pi^{3/2}} \frac{v^2}{v_{th}^3} e^{-\frac{v^2}{2v_{th}^2}}$ as it varies over our intensity dependent velocity range. The velocity v is normalized to $v_E = \sqrt[4]{\frac{Ze^3E}{m^2}}$ and therefore varies as $E^{1/4}$ as indicated in Eq.(2.4). A significant portion of electrons exist in the velocity space where $v < v_{osc}$ for a plasma at $T = 100\text{ eV}$. It is this region of electron velocities that contributes to IB absorption [19].

4.3.1 Effective Cross Section Modification

As in the preceding chapter, the observed deviation of the effective cross section from the low field prediction prompts a proposal for a fit to the numerically observed curves. The following fit was determined specifically for the velocity

region $v < 1/\Omega$, or $v < v_{osc}$. In the limit of high velocities it is expected that fit for the low intensity run $\sigma_{eff,L}$ will provide a sufficient description of the cross section.

Beginning with the very low velocities the points are numerically differentiated and it is shown that they exhibited roughly a $1/v$ dependence which became the starting point for constructing the numerical fit.

It has been argued by Fraiman *et al.* [12] that for an arbitrary incidence angle the effective cross section should have a dependence like $1/v^2$ for low velocities and later revert back to a $1/v^4$ dependence. In particular it was suggested that the curve behave as

$$\sigma_{eff} = \frac{\Omega^2}{v^2} f_1(\Omega v, \cos^2 \theta_1) + \Omega^2 f_2(\Omega v, \cos^2 \theta_1), \quad (4.15)$$

where f_1 and f_2 were not specifically described. It was specified however that in the limit of high Ω the result should reduce to the low field prediction. Attempts were made to fit the data to an expression of this form, however no suitable curves for f_1 and f_2 were found that agree to any reasonable approximation to the data.

It is then proposed that for the velocity space $v < 1/\Omega$ the effective cross section takes the form

$$\sigma_{eff} = \frac{4\sqrt{2\pi}}{3} 5 \frac{1}{(\alpha(\Omega)v + v^2)}, \quad (4.16)$$

where the expression for $\alpha(\Omega)$ is found to conform best to an exponential decay. Through a linear regression analysis performed on the three high intensity runs the coefficients of this expression were determined and it was found that $\alpha(\Omega)$ behaves like

$$\alpha(\Omega) = 0.0087 \Omega^{-14/3}. \quad (4.17)$$

The predictions made using this formula can be seen in Figs.(??). The coefficient was chosen so as to be an integer multiple of the coefficient seen in front of the

collision frequency Eq.(4.7).

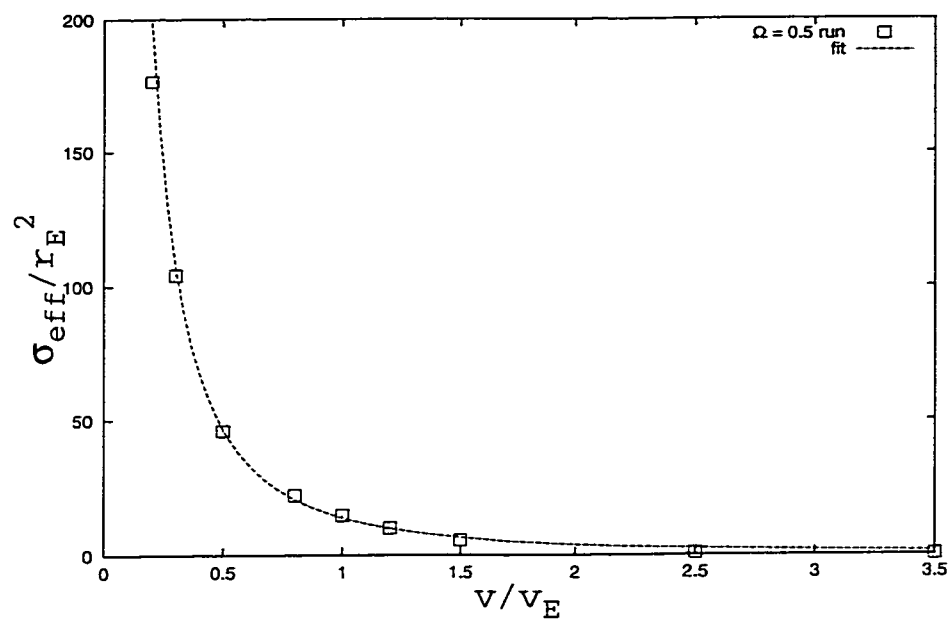


Figure 4.6: $\Omega = 0.5$ run curve fit.

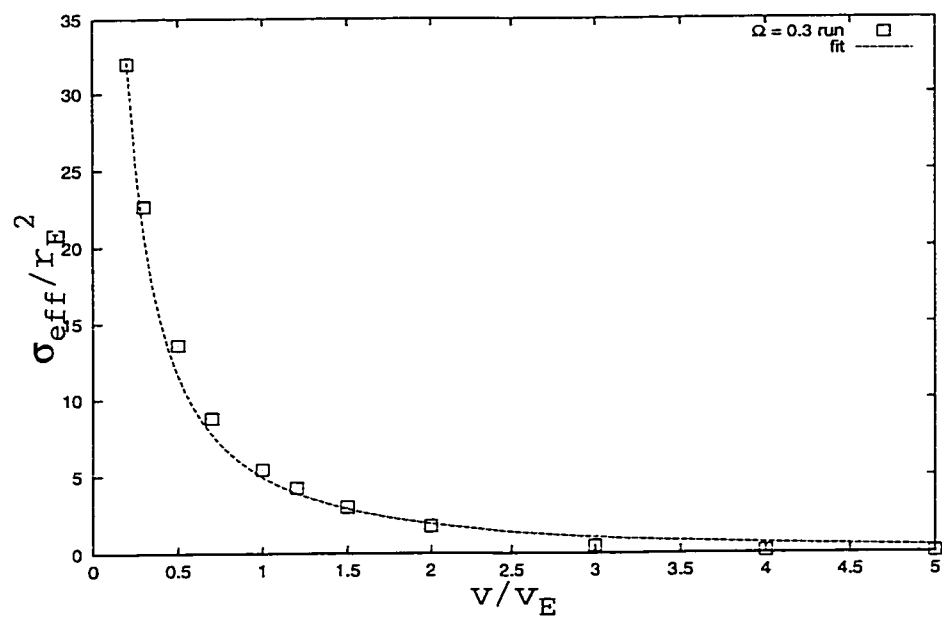
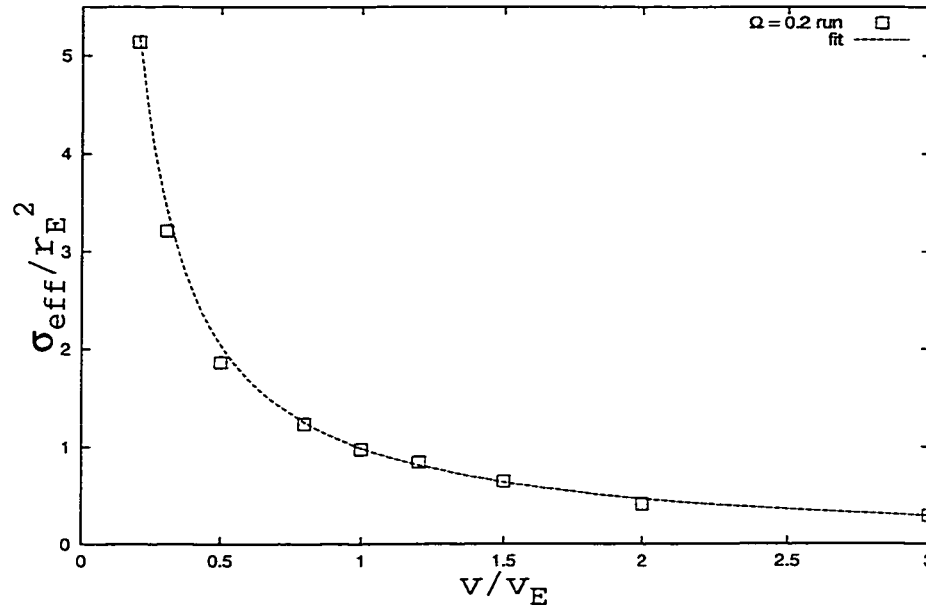


Figure 4.7: $\Omega = 0.3$ run curve fit.

Figure 4.8: $\Omega = 0.2$ run curve fit.

As indicated above, a curve of this form deviates substantially from the values obtained in the simulation when $v > 1/\Omega$. In this region the effective cross section returns to the value predicted by the low intensity result. In order to obtain an accurate theoretical model, one must incorporate a smoothing function to pass from $\sigma_{eff}(v < v_{osc})$ to $\sigma_{eff}(v > v_{osc}) = \sigma_{eff,L}$.

Because of the decaying form of α , Eq.(4.16) will quickly lose its dependence on $1/v$ as laser intensity is decreased and behave as $1/v^2$ at low intensities. Expanding the logarithm in equation 4.9 shows that for low velocities this expression also has a $1/v^2$ dependence. In the end this is not different from the suggestion of Fraiman *et al.* mentioned above.

Because of the strong dependence on the dimensionless frequency it can be proposed that as the laser intensity increases the effective cross section will behave as $1/v$. Recalling that the effective collision frequency is related to the effective cross section by a factor of $n_i v$, we see that the collision frequency would

approach a constant value in this space defined simply by $1/\alpha(\Omega)$. Physically speaking this would make sense in that when $v \ll v_{osc}$, the collision frequency should only be a factor of the field intensity rather than the drift velocities of each particle. This result is supported by Silin [7]. With the dependence on α as expressed in Eq.(4.17) the collision frequency would then scale with the laser field magnitude as $E^{-7/2}$.

4.3.2 Modification to the IB Heating Rate

With the data obtained it was then possible to propose values for $g(u)$ in equation 4.8. Because the expression for $g(u)$ has no explicit dependence on velocity, it is necessary to average the resulting cross sections over a Maxwellian velocity distribution. We arrive at an expression for this multiplier using

$$g(u) = \frac{\int_{-\infty}^{\infty} f_M v \sigma_{eff}(v, \Omega) d^3v}{\int_{-\infty}^{\infty} f_M v \sigma_{eff}(v, \Omega = 2) v} \quad (4.18)$$

where the integration is based on the data points for σ_{eff} at each intensity.

The integration indicated was performed numerically at temperatures of 80, 100 and 200 eV. The results of the high intensity runs are normalized to the $\Omega = 2.0$ run. It was assumed that these results could provide a benchmark against which to measure the high intensity runs because it was firmly established by Vick *et al.* [23] that at this intensity $g(u)$ is approximately 1.

The plasma parameters used were taken to mirror those established by Vick *et al.* and were: $Z = 10$, $T_e = 100$ eV (80 and 200 eV as well), $\omega_p/\omega_0 = 0.1$ and $\omega_0 = 7 \times 10^{15}$ Hz. The temperatures were chosen at this level also because here the thermal velocities lie below the oscillatory velocity and the majority of particles in the distribution lie in the regions of interest.

In order to increase the accuracy of the result which is based on approximately 10 points for each intensity, it was necessary to extrapolate the curves between the known points. That allowed for the integration to be done over equal intervals. In the temperature regions investigated the Maxwellian curves (as indicated in Fig.(4.5)) have the majority of particles about the regions where the the proposed modification to the effective cross section exits. For higher temperatures the bulk of electrons increase drift velocities thus a Maxwellian distribution for $T = 200$ eV has significant portions of electrons that occupy both $v < v_{osc}$ and $v > v_{osc}$. Hence there are contributors to the integral from the region where our modification applies and where the data conformed to the low field results.

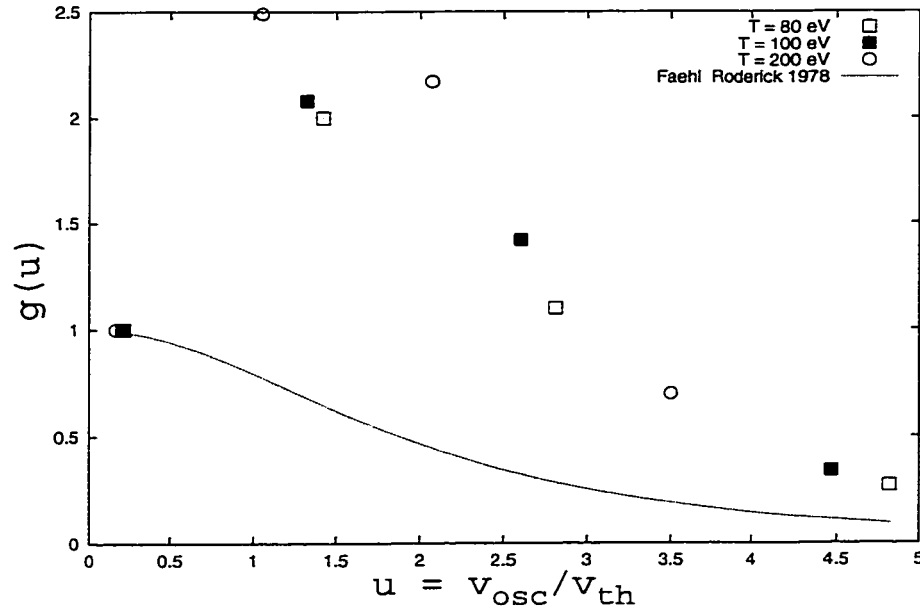
Tables 4.1 and 4.2 summarize the variables investigated in this study that correspond to the above mentioned laser plasma parameters, and the resulting values for $g(u)$.

Ω	Intensity W/cm^2	v_{th}/v_E	u	g(u)
0.2	1.05×10^{17}	0.94	4.47	0.34
0.3	3.55×10^{16}	1.08	2.60	1.42
0.5	8.97×10^{15}	1.28	1.32	2.08
2.0	2.25×10^{14}	2.03	0.21	1.00

Table 4.1: This table indicates the different parameters examined for the effective cross section, and the associated values for $g(u)$ after averaging the results over a Maxwellian distribution for the $T = 100$ eV case. Note the increase in $g(u)$ above unity.

As these tables indicate there exists a region where the modifier to the effective collision frequency is greater than unity. The results above show that it becomes more pronounced as the centre of Maxwellian is shifted into the region where the effective cross section was obtained with values greater than the low

Ω	$T = 80 \text{ eV}$			$T = 200 \text{ eV}$		
	v_{th}/v_E	u	$g(u)$	v_{th}/v_E	u	$g(u)$
0.2	0.84	4.82	0.27	1.33	3.50	0.70
0.3	1.08	2.81	1.10	1.52	2.07	2.17
0.5	1.14	1.42	2.00	1.81	1.05	2.49
2.0	1.81	0.22	1.00	2.87	0.17	1.00

Table 4.2: The results averaged over Maxwellians with $T = 80$ and 200 eV .Figure 4.9: The results for $g(u)$ plotted against a simple approximation.

field result. However as intensity further increases the value for $g(u)$ again drops below unity. Essentially this indicates a region where the IB heating rate should exceed the rate predicted by the low field result. However, because these results are seen to relax to the low field fit at higher velocities this increased heating rate will be short lived. It would appear that as v_{th} passes v_{osc} the heating rate will compare to that of previous predictions. Further for higher laser intensities,

this region of increased heating will not exist at all. As described by Vick *et al.* there will be a notable decrease of $g(u)$ from unity. Studies by Faehl and Roderick [24], Silin [7], Schlessinger and Wright [25], and Dawson and Oberman [6] predict that $g(u)$ will follow a curve reasonably approximated by

$$g(u) = \left(1 + \frac{u^2}{6}\right)^{-3/2}. \quad (4.19)$$

Our results are plotted against this expression in Fig.(4.9). This was suggested by Faehl and Roderick who argued that the classical expression for ν_{ei} could be modified simply by using a more suitable effective velocity where the electron's kinetic energy incorporates an averaging over the laser period.

$$\frac{1}{2} \langle mv^2 \rangle = \frac{3}{2}T + \frac{1}{4}mv_{osc}^2, \quad (4.20)$$

The region of increased effective cross section in our study will inhibit this heating rate from decreasing as rapidly the curve above would indicate.

Chapter 5

The Particle-Simulation Model

5.1 Introduction

The final goal of any kinetic model of a fully ionized plasma is to accurately describe the interactions between the charged particles. In general these interactions are comprised of two types: long range collective interactions, and short range, binary collisions. The Debye length has been established as the scale of reference separating the two. In plasma particle simulations the two interactions are usually treated in two separate, uncoupled processes. The long range interactions are dealt with by the Vlasov-Maxwell equations, while the short range collisions are traditionally described by the Landau collision operator, Eq. (1.49). The end result is then a superposition of the two processes.

In a particle simulation, the computation cycle is broken into discrete timesteps denoted as Δt . During each step charges and currents are accumulated on a grid, and the fields are calculated. Then the forces are computed at the particle positions and the particles are pushed. Finally, the collisions occur, leading to the velocity scattering. This work has concentrated on the treatment of the collisions through the modification of a binary model proposed by Takizuka and Abe [18].

Also a great deal of insight was gained by a similar development presented by Ma *et al.* [20].

The intent of this chapter is to summarize this model and the modifications we incorporated as well as introduce its relative performance and establish a base for the heating tests that were later performed using this model. This chapter will conclude with a discussion of how the transport cross section proposed in chapter 3 was incorporated into this Monte Carlo kinetic particle code and its subsequent effects on the heating rate when a short pulse laser is introduced to the system.

5.2 Model

To simulate the collisions in the plasma, a Monte Carlo method is applied to a system of binary paired particles. Our model is confined to 1D spatial and 3D velocity space. To explain the details of the algorithm it should first be broken into its constituent steps.

Constituent Steps of the Algorithm

1. The simulation system is established in one spatial dimension which is then divided into a number of smaller domains, or spatial cells. The cell size is subject to the constraint that any change in the properties of the plasma must be insignificant across it. Typically a Debye length is used.
2. The initial position and velocity of each particle are set up in accordance with the distributions of the proposed initial state of the plasma.
3. The particle motion is calculated using the finite-size particle method over a discrete time step Δt . The time step itself is constrained to insignificance

compared with the mean relaxation time. The particle motion and the collision processes are taken to be mutually independent over Δt .

4. The particles are assigned random partners within the cell of respective location, effectively pairing them for the collision process. It should be noted that the finite separation of particles within a cell is neglected by this model. During this process there are three uncoupled pairings possible: ion-ion, electron-ion and electron-electron. The ion-ion interactions are generally neglected however because their high mass and low velocity make their contributions to the evolution of the system insignificant on the time scales studied.
5. The algorithm then calculates the changes in velocities of the particles due to the elastic binary collision over the time step Δt . The particles are then assigned new velocities and moved accordingly.
6. For the duration of the run, the system is advanced in timestep increments of Δt . Steps 3 through 5 are repeated in succession as prescribed.

5.2.1 Pairing the Particles

Our model incorporates both electron-electron collisions and electron-ion collisions. As mentioned above these two separate collisions are taken to be uncoupled. The pairing process for the electron-electron collisions follows as a simplified version of the electron-ion case. Thus I shall limit the description below to the case of the electron-ion collision from which the electron-electron algorithm can be easily determined. There are three distinct steps to the pairing process our model utilizes.

(i) We assume the system contains an identical number of particles (N_0) for each species. In the first step, we associate a two dimensional array with

each particle of each species. This allows us to ascertain which cell a given particle is in, based on its location in the domain of the system, and enumerate which number particle it is in that particular cell. For example, the expression $\mathbf{iploci}(52,2) = 200$ would indicate that the second ion in cell 52 is ion number 200, $\mathbf{iploce}(27,8) = 93$ would indicate that the eighth electron in cell 27 is electron number 93. The array values are assigned merely by using a cycled set of test conditions. Additionally this step inherently yields the total number of particles of each species in each cell.

(ii) We next randomize the particles inside each cell. The intention here is to pair the first ion with the first electron, second ion with second electron, *etc.* As noted above, the finite separation distances between particles within each cell are neglected by this model. Thus, as long as the arranged particles are inside a cell, their order is unimportant for pairing. However, to incorporate the stochastic nature of the scattering process, the particle ordering inside each cell is then randomly sorted. Table 5.1 outlines a typical case for an individual cell. The particles are originally sorted as found on the left, but the algorithm systematically repositions the particles randomly. To accomplish this we use a random number generator that outputs a number between one and the number of particles in the cell, then checks it against a list of previously selected numbers (analogous to pulling numbers from a hat) and then assigns the particle a position accordingly.

(iii) Once the pairing has been assigned the algorithm enters the scattering loop. Due to the stochastic nature of the system, however, there is no guarantee that the total number of particles of each species will be the same. Or, in the case of electron-electron scattering, there exists the problem of an odd number of electrons being found in a cell. Methods of treating this condition are outlined in [18] and [20], however we have found excellent results through a more straight

Initial Order		Random Arrangement	
electrons	ions	electrons	ions
200	199	203	202
201	200	206	204
202	201	205	199
203	202	202	201
204	203	204	203
205	204	201	200
206		200	

Table 5.1: This table demonstrates the technique used to randomly order the particles in in a particular cell. The actual numbers used are the identification numbers of the particles in the entire system and for simplicity they are aligned in ascending numerical order on the left. The right columns correspond to their positions after the randomization process. The particles are then paired with their horizontal neighbours. Note that there is a good possibility that there will be an unequal total number of particles from each species.

forward scheme that remains true to the binary collision process. Takizuka and Abe [18] suggest a pairing process that collides odd particles with ones that have already collided, but this implies a tertiary (or even higher order) collision process. Ma *et al.* [20] on the other hand suggest moving particles into adjoining cells, but this method was found to be tediously impractical.

Our solution was simply to insert a test condition at the beginning of the scattering loop. The code checks each cell for the difference between ion and electron numbers. If there is a difference, the excess particles are allowed to continue on their trajectory without undergoing a collision for that particular

time step. There are three reasons we can get away with this. First, the spatial particle distribution is relatively isotropic throughout the system and thus the probability of obtaining a very large difference is small. Second, the system redistributes itself each cycle and therefore it is unlikely a significant difference will repeat. Third, Δt is on the order that for a single collision to be completed in its entirety, one hundred scattering cycles must be run. Hence the error from one step would be negligible (*i.e.* one percent per unpaired particle).

Finally, the remaining particles are paired in descending order, and then they undergo a velocity transformation prescribed by the details of a binary collision discussed below.

5.2.2 Details of the Collision

The fundamental system that we start with is that of a Lorentz gas with the limiting case of cold, infinitely massive ions. We then have electrons free to move in three-dimensional velocity space. They undergo Coulomb interactions with the ions and hence experience small angle collisions. In this model, energy is conserved and thus the end result of the collision is a rotation of the total velocity vector in velocity space. An arbitrary rotation is depicted in Fig.(5.1).

Because energy is conserved in the collision, the magnitude of the total velocity vector in this space remains the same. Hence the result of the collision is expressed as a function of two variables, θ and ϕ , where

θ describes the scattering angle and obeys a Gaussian distribution, and

ϕ describes the polar angle and is uniformly distributed on the interval $(0, 2\pi)$.

Thus the algorithm computes and returns these angles. To accomplish this, we require $P(\theta, \phi)$, which is defined as the probability distribution for an e-i

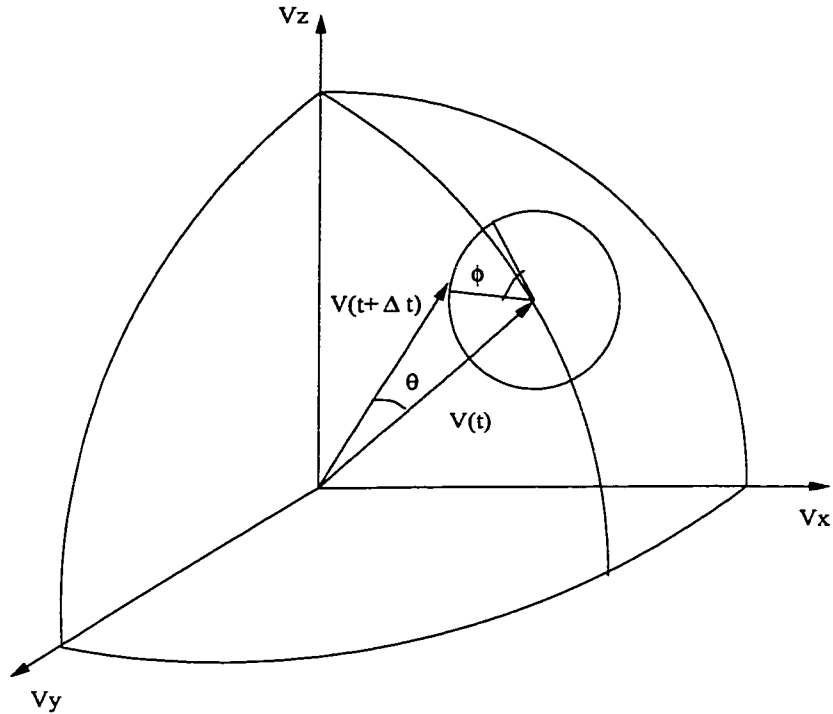


Figure 5.1: This sketch illustrates the Lorentz model rotation of the total velocity vector in velocity space as a result of the collision between the electron and ion. The polar angle ϕ obeys a uniform distribution whereas the scattering angle θ is restricted to a Gaussian distribution.

collision resulting in a rotation of the total velocity vector about θ and ϕ after a given time Δt .

By definition the angles are independent of each other and therefore $P(\theta, \phi)$ is a separable function

$$P(\theta, \phi) = P(\theta) P(\phi), \quad (5.1)$$

which is why the two angles can be examined separately. ϕ is assumed to have a uniform distribution from 0 to 2π , so this would result in the form

$$P(\phi) = \frac{1}{2\pi} \int_0^\phi d\phi'. \quad (5.2)$$

Computationally, it is easy to find a random number generator that will return a value R_1 confined to the interval $(0,1)$ with a uniform distribution. Therefore to produce the required uniform distribution on $(0,2\pi)$ for each collision, the polar angle ϕ is assigned a value

$$\phi = 2\pi R_1 \quad (5.3)$$

The scattering angle presents a more involved problem. Fundamentally, it is assumed that the particle motion in the plasma results from a random walk and thus exhibits Brownian motion. It has been established that the general distribution of the scattering angle should have a Gaussian form, but the particulars of the form need to be determined. Following the derivation presented in [26] the mean and standard deviation are determined from the diffusion equation

$$\frac{\partial P(\theta)}{\partial t} = D \frac{\partial^2 P(\theta)}{\partial \theta^2} \quad (5.4)$$

where D is the self-diffusion coefficient, given by the transport collision frequency ν_{ei} . First, to find the mean we multiply both sides of equation 5.4 by θ and integrate over theta

$$\int_{-\infty}^{\infty} \theta \frac{\partial P(\theta)}{\partial t} d\theta = D \int_{-\infty}^{\infty} \theta \frac{\partial^2 P(\theta)}{\partial \theta^2} d\theta \quad (5.5)$$

The left hand side becomes

$$\frac{\partial}{\partial t} \int_{-\infty}^{\infty} \theta P(\theta) d\theta = \frac{\partial}{\partial t} \langle \theta \rangle . \quad (5.6)$$

The right hand side can be broken up through an integration by parts

$$D \int_{-\infty}^{\infty} \theta \frac{\partial^2 P(\theta)}{\partial \theta^2} d\theta = D \theta \frac{\partial P(\theta)}{\partial \theta} \Big|_{\theta=-\infty}^{\theta=\infty} - D \int_{-\infty}^{\infty} \frac{\partial P(\theta)}{\partial \theta} d\theta. \quad (5.7)$$

Because $P(\theta = \pm\infty) = 0$ and the spatial derivatives of $P(\theta)$ at $\pm\infty$ are also zero the first term vanishes. The remaining integral becomes $D[P(\theta = \infty) - P(\theta =$

$-\infty)$] which is also zero. Thus

$$\frac{\partial}{\partial t} \langle \theta \rangle = 0, \quad (5.8)$$

which means $\langle \theta \rangle$ is a constant, independent of time. The system requires that $\theta = 0$ as an initial condition, thus $\langle \theta \rangle = 0$ for all time.

To calculate the mean square value ($\langle \theta^2 \rangle$) a similar procedure is followed. First the diffusion equation is multiplied by θ^2 and then integrated

$$\int_{-\infty}^{\infty} \theta^2 \frac{\partial P(\theta)}{\partial t} d\theta = D \int_{-\infty}^{\infty} \theta^2 \frac{\partial^2 P(\theta)}{\partial \theta^2} d\theta. \quad (5.9)$$

The left hand side results in the expression $\frac{\partial}{\partial t} \langle \theta^2 \rangle$. The right hand side is completed with two integrations by parts as above.

$$D \int_{-\infty}^{\infty} \theta^2 \frac{\partial^2 P(\theta)}{\partial \theta^2} d\theta = D \theta^2 \frac{\partial P(\theta)}{\partial \theta} \Big|_{\theta=-\infty}^{\theta=\infty} - D \int_{-\infty}^{\infty} 2\theta \frac{\partial P(\theta)}{\partial \theta} d\theta. \quad (5.10)$$

With the first separation into parts the first term is again zero by the argument presented above. The second term goes through the “by parts” integration one more time.

$$-D \int_{-\infty}^{\infty} 2\theta \frac{\partial P(\theta)}{\partial \theta} d\theta = -2D \left(\theta P(\theta) \Big|_{-\infty}^{\infty} - \int_{-\infty}^{\infty} P(\theta) d\theta \right) \quad (5.11)$$

Finally the first term here goes to zero again, but by definition the second term must go to unity. Thus we arrive at the expression

$$\frac{\partial}{\partial t} \langle \theta^2 \rangle = -2D. \quad (5.12)$$

And given that $\theta(0) = 0$ we can integrate and find

$$\langle \theta^2 \rangle = 2Dt. \quad (5.13)$$

Thus for a random walk in the scattering angle θ governed by the diffusion equation where the self diffusion coefficient is the transport collision frequency,

over a time period Δt the mean square of the scattering angle will be described by

$$\langle \theta^2 \rangle = 2\nu_{ei}\Delta t. \quad (5.14)$$

With this established, an expression for the scattering angle over a time period Δt can be determined. I will begin with the assumption of a Gaussian probability density and further assume that by the Coulomb nature of the collisions this model describes that only positive values of θ are physically possible,

$$P(\theta) = Ae^{-\frac{\theta^2}{2\langle \theta^2 \rangle}} \quad \theta \geq 0 \quad (5.15)$$

and the probability density is then zero for the disallowed range where $\theta < 0$. Here A is the normalization constant. Using

$$\int_{-\infty}^{\infty} P(\theta)d\theta = 1, \quad (5.16)$$

A was determined to have the value

$$A = \frac{1}{\sqrt{\pi} \langle \theta^2 \rangle} = \frac{1}{2\sqrt{\pi}\nu_{ei}\Delta t}. \quad (5.17)$$

To determine the scattering value for θ the nonuniform Gaussian distribution must be mapped onto a uniform distribution. This is accomplished using the cumulative distribution function $C(\theta)$. By definition,

$$C(\theta) \equiv \int_{-\infty}^{\theta} P(\theta')d\theta'. \quad (5.18)$$

The cumulative distribution function can be generated by a uniform random number generator, represented by R_2 . Therefore

$$R_2 = \int_{-\infty}^{\theta} P(\theta')d\theta'$$

$$\begin{aligned}
&= \int_0^\theta \frac{1}{2\sqrt{\pi}\nu_{ei}\Delta t} e^{-\frac{\theta'^2}{4\nu_{ei}\Delta t}} d\theta' \\
&= \frac{2}{\sqrt{\pi}} \int_0^\theta e^{-\mu^2} d\mu \\
&= \operatorname{erf}(\theta),
\end{aligned} \tag{5.19}$$

which is the error function. Numerically the error function can be approximated as

$$\operatorname{erf}(\mu) \approx 1 - e^{-2\mu}. \tag{5.20}$$

Hence

$$R_2 = 1 - e^{-\frac{\theta^2}{2\nu_{ei}\Delta t}}, \tag{5.21}$$

which leads to a value for θ when solved for θ that occurs after a time step of Δt .

$$\theta = [2\nu_{ei}\Delta t \ln(1 - R_2)]^{\frac{1}{2}} \tag{5.22}$$

5.2.3 Changes in Velocity

Having established Eq.(5.3) and Eq.(5.22), I shall describe briefly how the velocities of the paired particles change due to a collision. In the laboratory frame, the relative velocity between the particles is defined as

$$\vec{u}(t) = \vec{v}_e(t) - \vec{v}_i(t) = (u_x, u_y, u_z, t). \tag{5.23}$$

The post collision velocities are then given by

$$\vec{v}_e(t + \Delta t) = \vec{v}_e(t) + \frac{m_{ei}}{m_e} \Delta \vec{u} \tag{5.24}$$

$$\vec{v}_i(t + \Delta t) = \vec{v}_i(t) - \frac{m_{ei}}{m_i} \Delta \vec{u}, \tag{5.25}$$

where m_{ei} is the reduced mass of the electron-ion system and $\Delta\vec{u}$ is the change in the relative velocity of the particles due to the collision. To define our velocities in spherical coordinates we state

$$\vec{u}_x = \vec{u} \sin\psi \cos\gamma, \quad (5.26)$$

$$\vec{u}_y = \vec{u} \sin\psi \sin\gamma, \quad (5.27)$$

$$\vec{u}_z = \vec{u} \cos\psi, \quad (5.28)$$

which defines the angles ψ and γ . $\Delta\vec{u}$ is then given by the deflection through angles θ and ϕ as given above. Thus components of $\Delta\vec{u}$ are given by

$$\begin{aligned} \Delta\vec{u}_x &= \frac{u_x(t)}{u_\perp(t)} u_z(t) \sin\theta \cos\phi - \frac{u_y(t)}{u_\perp(t)} u(t) \sin\theta \sin\phi - u_x(t) (1 - \cos\theta), \\ \Delta\vec{u}_y &= \frac{u_y(t)}{u_\perp(t)} u_z(t) \sin\theta \cos\phi + \frac{u_x(t)}{u_\perp(t)} u(t) \sin\theta \sin\phi - u_y(t) (1 - \cos\theta), \\ \Delta\vec{u}_z &= -u_\perp(t) \sin\theta \cos\phi - u_z(t) (1 - \cos\theta). \end{aligned} \quad (5.29)$$

where

$$u = \sqrt{u_x^2 + u_y^2 + u_z^2}, \quad (5.30)$$

$$u_\perp = \sqrt{u_x^2 + u_y^2}. \quad (5.31)$$

It should further be noted that in the case where $u_\perp = 0$, the above expression reduces to

$$\Delta\vec{u}_x = u(t) \sin\theta \cos\phi, \quad (5.32)$$

$$\Delta\vec{u}_y = u(t) \sin\theta \sin\phi, \quad (5.33)$$

$$\Delta\vec{u}_z = -u(t) (1 - \cos\theta). \quad (5.34)$$

5.3 General Results of Standard Tests

In order to test the kinetic behavior of this model, we performed simulations to evaluate its performance against the analytical predictions of test particle theory as outlined by Spitzer [28] and Trubnikov [29]. In such a theory we assume the existence of a test particle which is assumed to have no effects on the medium, and a medium with a of temperature T_i with a Maxwellian velocity distribution

$$f_i(v) = n_i \left(\frac{m_i}{2\pi T_i} \right)^{\frac{3}{2}} e^{-\frac{m_i}{2T_i} v^2}. \quad (5.35)$$

As a result of collisions with the medium, the test particle experiences diffusion in velocity space, or relaxation.

5.3.1 Drift Velocity Slowing

We first considered the slowing down rate ν_s . Here, electrons were initially given a shifted Maxwellian distribution in the x dimension of velocity space with a mean velocity v_{dx0} and temperature $T_{e(0)}$.

$$f_e(v) = n_e \left(\frac{m_e}{2\pi T_{e0}} \right)^{3/2} e^{-\frac{m_e}{2T_{e0}(\bar{v}-v_{dx0})^2}} \quad (5.36)$$

It is then known [28, 29] that the evolution of v_{dx} with time goes like

$$\frac{dv_{dx}}{dt} = -\nu_s v_{dx} \quad (5.37)$$

where

$$\nu_s = \frac{1}{4} \mu \left(\frac{\epsilon}{T_{e0}} \right) \left(\frac{T_{e0}}{\epsilon} \right)^{3/2} \nu_0. \quad (5.38)$$

This introduces the parameters $\epsilon = \frac{1}{2} m_e v_{dx0}^2$, (5.38) and

$$\begin{aligned} \mu(x) &= \frac{2}{\sqrt{\pi}} \int_0^x e^{\xi} \xi^{1/2} d\xi \\ &= \frac{2}{\sqrt{\pi}} \left[-\sqrt{x} + \frac{\sqrt{\pi}}{2} \operatorname{erf}(\sqrt{x}) e^x \right] e^{-x}. \end{aligned} \quad (5.39)$$

Where $erf(x)$ is the error function and ν_0 is the electron-ion collision frequency ($\nu_0 = n_i v \sigma_{Ruth}$). Further simulation parameters are $m_e/m_i = 0.01$, $T_e/T_i = 1$, $\nu_0 \Delta t = 0.0001$, and the number of particles was 51 200. (Note that the system was shown to have less numerical noise for runs with 512 000 or more particles, but sufficient results were obtained using the above number.)

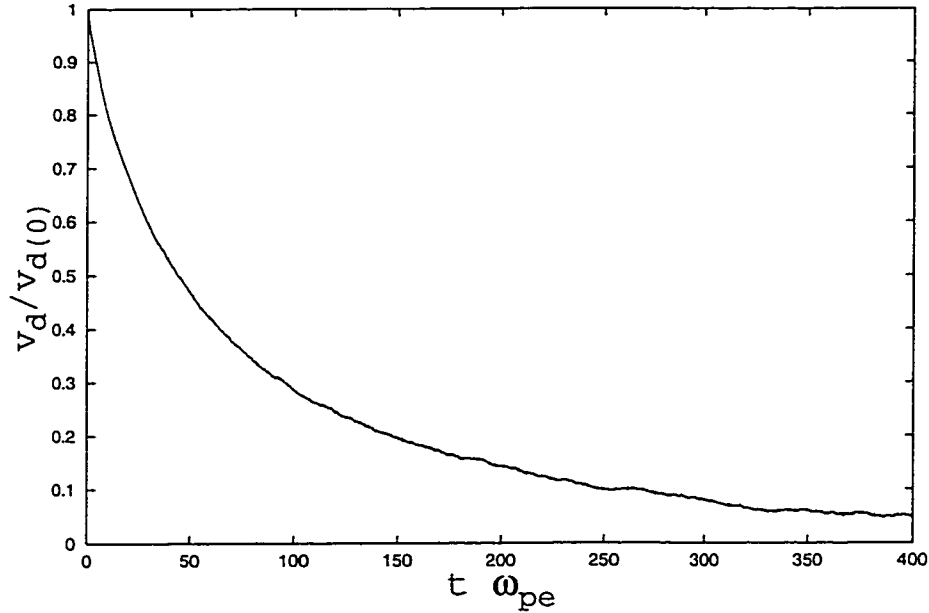


Figure 5.2: This figure is an example of the velocity relaxation for a shifted Maxwellian initial distribution. This particular run looked at an initial parameter of ϵ/T_{e0} of 0.5, with a collision frequency $\nu_0 = 0.05$. The system was run until the drift velocity reached $1/e^3$ of its initial value. The resulting curve conforms well to the expected logarithmic decay.

Fig.(5.2) illustrates a typical example of a slowing run performed with an initial velocity shift defined by $x = \epsilon/T_{e0} = 1/2(v_{dx0}/v_{th})^2 = 0.5$. The collision frequency ν_0 was set at 0.05. The run was allowed to go on until it reached about five percent of its initial value. From this point the curve was linearized and then analyzed using linear regression to determine the slowing rate ν_s .

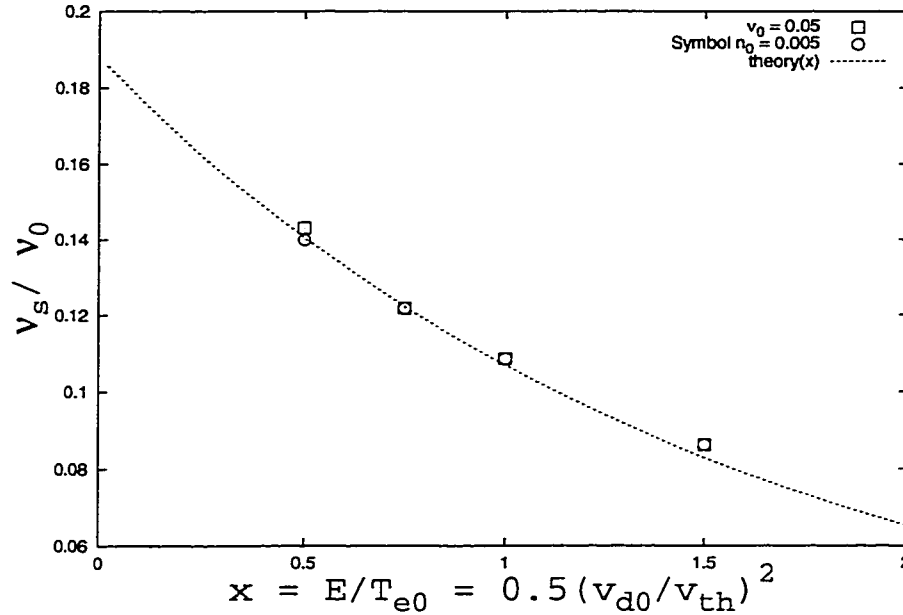


Figure 5.3: Slowing tests were performed for $x = 0.5$ through 1.5 using both collision frequencies of 0.05 and 0.005 ω_{pe} . The resulting points came within six percent at maximum of the analytical result.

In Fig.(5.3), we see the cumulative results of similar tests. These were taken over the range of initial drift velocities defined with $x = 0.5$ to 1.5, and with collision frequencies of 0.05 and 0.005 ω_{pe} . The results conformed well to the analytical predictions, with a maximum deviation of six percent.

5.3.2 Thermal Isotropization

The next investigation examined the evolution of a system with an initial thermal anisotropy. To accomplish this, we first established a difference between the longitudinal (T_{\parallel}) and transverse (T_{\perp}) temperatures. Such a system is known to relax to an isotropic Maxwellian in a process known as thermal isotropization [28, 29]. As above, this relaxation can be predicted analytically and thus should

approximately conform to

$$\frac{d}{dt}(T_{\parallel} - T_{\perp}) = -\nu_{iso}(T_{\parallel} - T_{\perp}), \quad (5.40)$$

where ν_{iso} is related to the collision frequency by

$$\nu_{iso} = \frac{8}{5\sqrt{2\pi}}\nu_0. \quad (5.41)$$

Here it should be noted that the collision frequency is calculated using the relation $T = 1/3(T_{\parallel} + 2T_{\perp})$. In this investigation T_{\parallel} lies in the x direction, while $T_{\perp} = 1/2(T_y + T_z)$ is in the y-z plane.

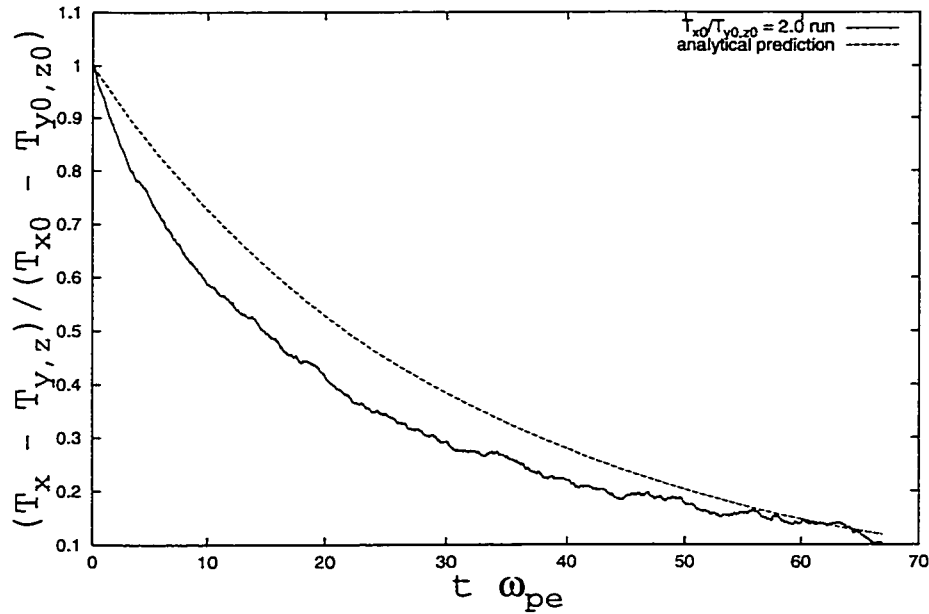


Figure 5.4: In this run the code was initialized with $T_{\parallel}/T_{\perp} = 2$. Again we examined the run for 51200 particles at a collision frequency of $\nu_0 = 0.05 \omega_{pe}$. The curve came within five percent of the analytical prediction.

Fig.(5.4) depicts the results of a 51200 particle run where the initial anisotropy was established at $T_{\parallel}/T_{\perp} = 2$. The collision frequency was set at $\nu_0 = 0.05 \omega_{pe}$. The anisotropy was tracked as a difference between T_x and the $T_{y,z}$ average as

it fell from its original value to below ten percent. Again the logarithmic curve was linearized and put through a regression analysis which resulted in a value of $\nu_{iso} = 0.0301$, which compared to the prediction of 0.0319 has a deviation of only five percent.

5.3.3 Temperature Relaxation

The next test considered the initial condition where the temperature of one species (the electrons T_e) was greater than the temperature of the other (the ions T_i .) Once again test particle theory predicts that the temperature difference should decrease logarithmically with time and equilibrate approximately as

$$\frac{d}{dt}(T_e - T_i) = -2\nu_{eq}(T_e - T_i) \quad (5.42)$$

with

$$\nu_{eq} = \frac{8}{3}\sqrt{\pi} \left(1 + \frac{m_e T_i}{m_i T_e}\right)^{3/2} \nu_0. \quad (5.43)$$

I have included Fig.(5.5) as an example of the relaxation of temperature. In this run 5120 particles were used and the temperature of the ions was modified such that $T_{e0}/T_{i0} = 2$. the dashed line represents the analytical prediction of equation 5.43. Once again the data was linearized and a regression analysis showed that the simulation resulted in a six percent discrepancy from the theoretical curve. It should also be noted here that the previous tests were investigated with the assumption of cold, infinitely massive ions, and therefore the code performed with stationary ions. However, for this test the ions were given non-zero velocities.

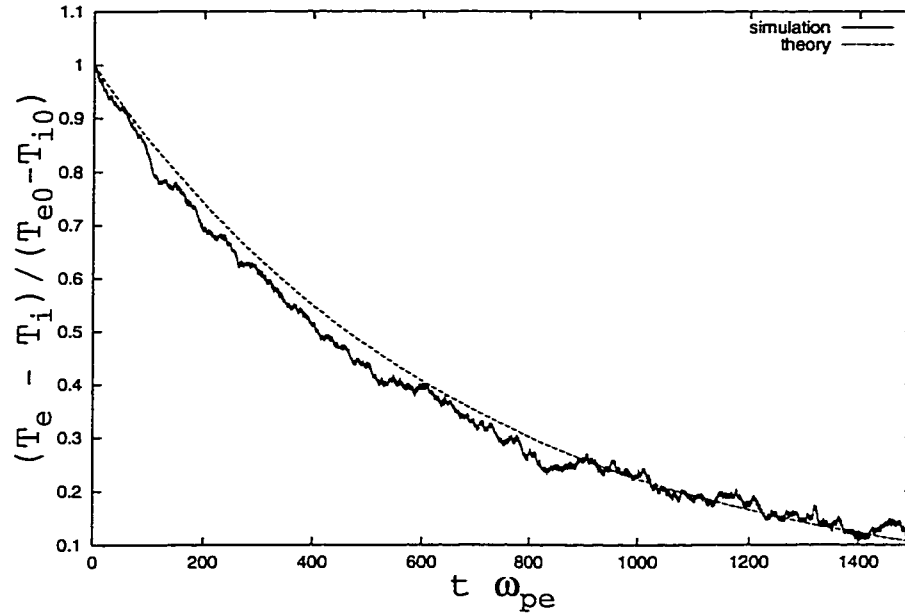


Figure 5.5: This graph illustrates a typical 5120 particle run where the initial temperatures were established such that $T_{e0}/T_{i0} = 2$. Again the result conformed well to the analytical prediction for ν_{ei} with a deviation of only six percent.

5.3.4 Entropy

As one final test for the code, the entropy of the system is investigated. To do this we examine the state function predicted by the Boltzmann H theorem

$$H = \int d^3v f_1(\vec{v}, t)_1(\vec{v}, t), \quad (5.44)$$

as it applied to each species. It is related to the thermodynamic entropy S through

$$S = -k_B H, \quad (5.45)$$

where k_B is the Boltzmann constant, $1.38 \times 10^{-23} J/K$. Following the arguments developed in Liboff [30] we know that $dS/dt \geq 0$, indicating that the entropy of a system is always increasing, and the equality holding for an equilibrium. In fact, looking at the Boltzmann equation it can be stated that for an arbitrary

initial distribution function f , $S(t)$ increases monotonically until $f'_2 f'_1 = f_2 f_1$ whereafter it remains constant.

To model this behavior, a system was chosen with an initially constant velocity distribution, *i.e.* all particles were given a velocity of v_{th} at the beginning of the simulation and the system was observed to relax from that ordered state. Fig.(5.6) follows the x component of the distribution function as it evolved in time.

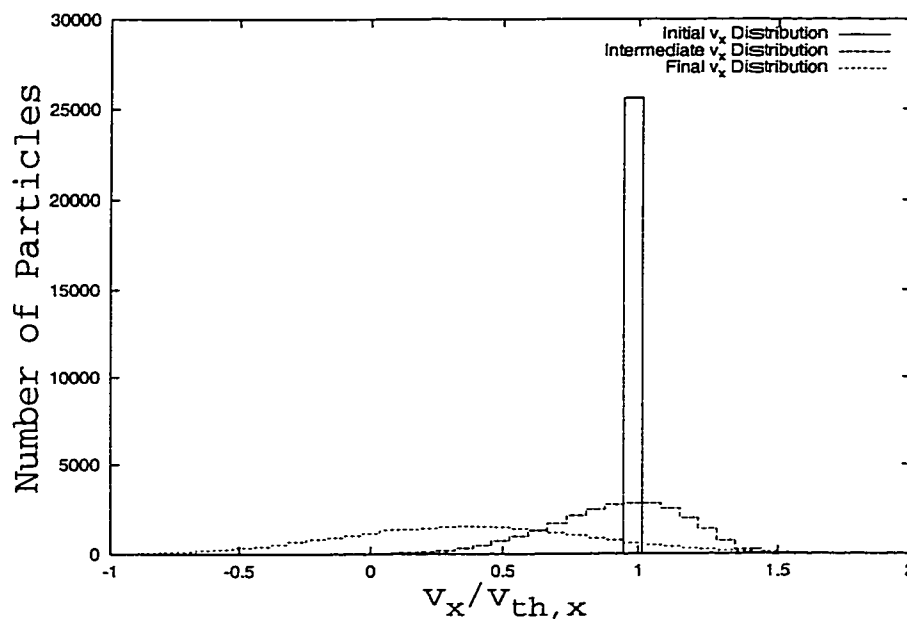


Figure 5.6: This figure depicts the x direction velocity distribution evolving from its initial state where all particles were issued a velocity equivalent to the thermal velocity down to a roughly Maxwellian distribution. The entropy in this case should increase until the system comes into equilibrium where it should level off to an approximately constant value.

The total entropy and that of each particle species (electrons and ions) is shown in Fig.(5.7). It was measured in units of Boltzmann's constant k_B . As predicted, the change in entropy is always positive and as the system nears its

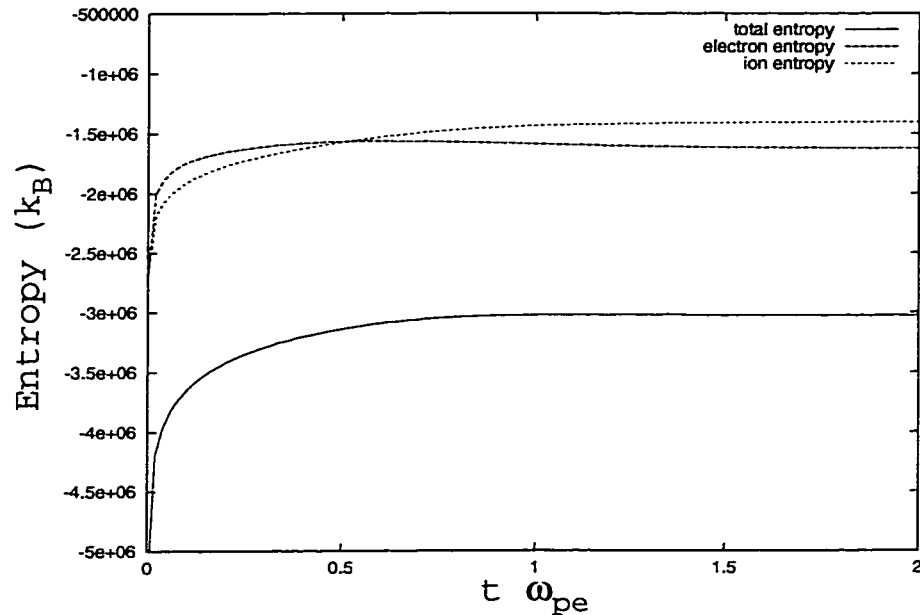


Figure 5.7: The entropy in units of k_B for both electrons, ions and the total of the system is plotted against time as the system is allowed to evolve from a constant velocity distribution to a rough Maxwellian as depicted above. The change in entropy over time is always positive and very quickly reaches a constant state in this 51200 particle test run.

equilibrium state, the total entropy approaches a constant value.

5.4 Notes on the Parallel Set Up

In order to speed up the computation time of this kinetic code we spent some time rewriting it so that it would be able to run in parallel using the message passing and FORTRAN paradigm (MPI). The basic idea behind parallel computing is that in an ideal situation, N processors will be able to complete a task in $1/N$ the time it would take for a single processor to perform it.

The approach of this simulation was to divide the problem across N proces-

sors which would run an equal number of the total particles. Thus a simulation involving x number of particles would ideally be able to be performed in the time it would take to perform a simulation of x/N particles. The collisions were performed and velocities and location data were tracked separately on each processor. At the end of each time step however certain macroscopic quantities such as temperature were collected and distributed accordingly through the system. In that way each processor was allowed information describing the macroscopic behavior of the other processors which was the difference between this and N independently run simulations of x/N particles. It bears noting that particles on different processors could not interact directly with each other, *i.e.* a particle on processor one could not collide with and scatter off of a particle on processor four. Thus although at any given time a cell may contain y particles, only y/N particles are available to be paired with each other on each processor. Therefore, it was necessary to ensure that this parallel technique was only applied when the number of particles was large enough that the pairing-scattering process would not result in any significant errors due to too few particles. Roughly speaking this implies a condition that an even distribution of the x/N particles through the domain on a given processor must result in a minimum of ten particles of each species in any particular cell.

It should be mentioned that originally this problem was approached by allocating a particular domain in the spatial region to each processor. So during the initialization process, processor number one was given the first x/N particles which all lay at one end of the simulation domain. Processor two received the next x/N particles which were placed beside those of the first processor, and so on. The result was a spatial anisotropy between the particles on each processor which led to some errors because spatial isotropy was implicitly assumed at the beginning of the study. Efforts were made to allow for particles to cross between

processors, however this treatment met with limited success because it placed a new test in the computation cycle which identified the boundary of each processor. Eliminating the presence of a particle that crossed this boundary on one processor and creating it on its adjacent partner proved so intensive that the time gained by the parallel set up was lost attempting to account for all the transitioning particles. The final solution to the problem was to redistribute the particles isotropically over the entire spatial simulation domain for each individual processor. Again this limited the communication to the macroscopic level, but the original goal of increasing the speed of the simulation was accomplished.

5.5 Heating Runs

With the kinetic portion of the PIC code developed the next step involved incorporating the laser field. An oscillating force based on the magnitude and frequency of the field was added so that the particles would be driven by the incorporation of the laser and heating properties of the system could be observed. At each time step the velocity due to the acceleration from the laser field was calculated and added to the total velocity of the electrons. The process was duplicated for the ions as well along with an option that allowed for the ions to be locked in place.

Because of the incorporation of the laser field it was necessary to now revisit Eq. (5.22),

$$\theta = [-2\nu_{ei}\Delta t \ln(1 - R_2)]^{\frac{1}{2}}. \quad (5.46)$$

Note that here the electron-ion collision frequency refers specifically to the transport collision frequency from chapter 3 because it considers elastic collisions only. Since the collision frequency is related to the transport cross section by the re-

lation

$$\nu_{ei} = n_i \sigma_{tr} v, \quad (5.47)$$

we can incorporate the modification proposed in Chapter 3, Eq.(3.25) by writing

$$\nu_{ei} = n_i \frac{\sigma_R}{1 + \Delta'(\Omega, v)} v. \quad (5.48)$$

It is important to note however that the velocity here is not the total velocity of the particle, but the drift velocity of the particle, or the velocity that would be observed in a frame oscillating with the laser frequency ω_0 . The reason for this is that equation 3.25 was formulated based on the initial input velocity averaged over all phases of the laser field. The drift velocity was the only component of the total velocity that survived the averaging process. Because of the stochastic nature of this Monte Carlo simulation, the initial drift velocity is all that is needed. The condition that is then placed on the algorithm is that at the beginning of the scattering process, the drift velocity must be extracted. The final scattering angle is then given by

$$\theta = \left[2 A' \left(\frac{v_{th}}{v_{osc}} \right)^3 \left(1 + \alpha(\Omega) \left[\frac{v_{dr}}{\Omega v_{osc}} \right]^{\beta(\Omega)} \frac{1}{\Omega^2} \left[\frac{v_{osc}^2}{v_{osc}^2 + v_{dr}^2} \right] \right)^{-1} \Delta t \ln(1 - R_2) \right]^{\frac{1}{2}}, \quad (5.49)$$

where A' is as defined in equation 3.9 multiplied by the ion density term.

The incorporation of this scattering angle into the particle code then yields a Monte Carlo simulator capable of describing the effects of an intense laser field heating a plasma. It should be noted however that this does not account for the inelastic collisions as the collision process is still assumed to be elastic. What this model does account for are effects from large angle scattering that previous models ignored.

There is still ongoing work in this study, now that this result has been implanted in the described particle code. I shall conclude this chapter with a brief example of some of the preliminary results.

The inverse bremsstrahlung heating was the first property of the system we examine using the code. The model considers a plasma with $Z=1$ and an initial temperature of $T_e = 1.0$ keV. The laser was assumed to have a frequency of $6.0\omega_{pe}$. Fig.(5.8) shows the results of heating runs where laser intensities were defined by $v_{osc}/v_{th} = 1.2$ (graph a) and 12.2(graph b). For both intensities the initial heating rate is significantly larger when the large angle scattering effects are for (curve 1) than with the conventional model (curve 2). The inset uses a dashed line to show the initial slope of the electron temperature of the modified curve. It is suspected that the electron distribution function, which was originally established as a Maxwellian, quickly redistributes itself, depleting the low velocity particles as depicted in Fig.(5.9). Because of the redistribution, at later times the heating rate decreases below that which is known for low intensity fields.

Fig.(5.9) provides examples of the electron distribution function both initially (curve 2) and soon after the simulation begins at $t\omega_{pe} = 100$ (curve 1) as evidence for the velocity redistribution. Graph a illustrates the function for $v_{osc}/v_{th} = 0.17$ while for b shows the higher intensity with $v_{osc}/v_{th} = 12.2$. Both clearly indicate the presence of a depletion of low velocity electrons. It is suspected that this is due to the extreme scattering that low velocity electrons experience. The “hole” as it has been deemed, has been shown to remain for a long time until the electron thermal velocity becomes sufficiently larger than the thermal velocity, at which time the electron-electron collisions smooth it out.

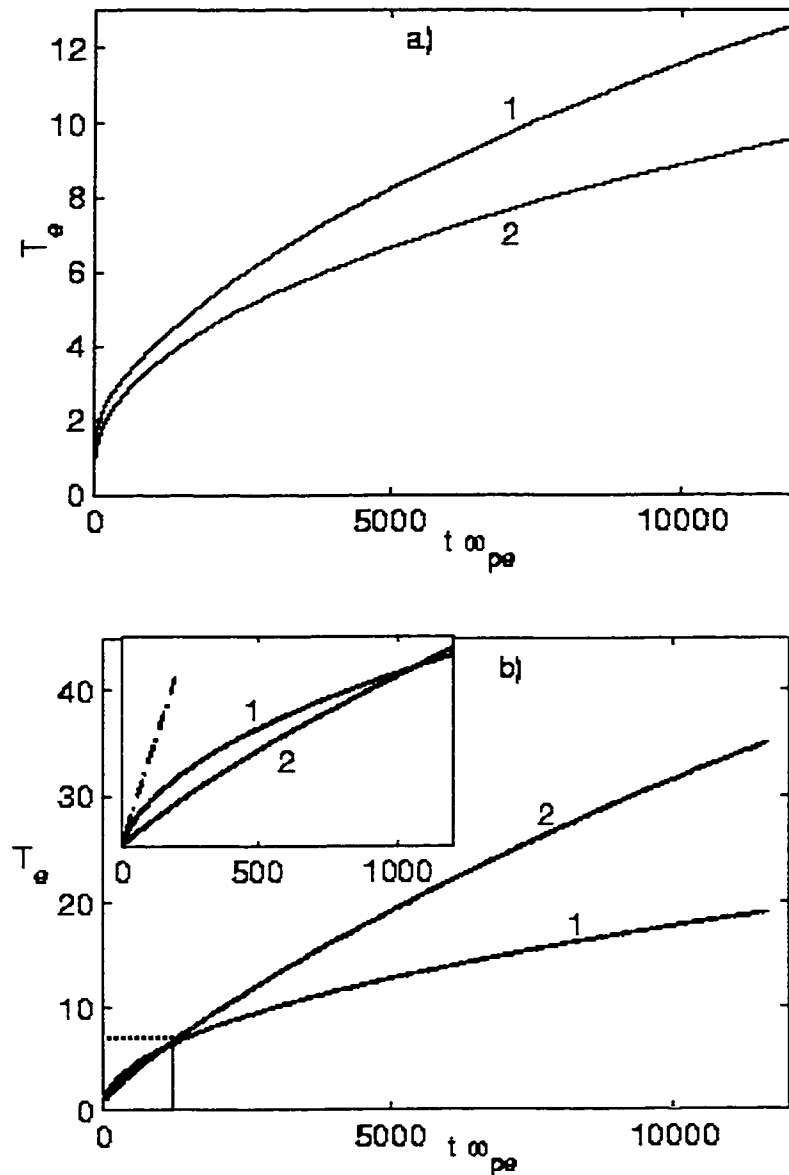


Figure 5.8: Evolution of the electron temperature over time due to IB heating. The laser intensity is defined by the parameter $v_{osc}/v_{th}(0) = 1.2$ (graph a) and 12.0 (graph b). Both graphs show curves with the modified transport cross section (1) and the original Rutherford cross section (2) implementing in the scattering algorithm. The inset graph presents the initial heating rate as depicted by the dashed tangent line, which significantly exceeds the usual one.

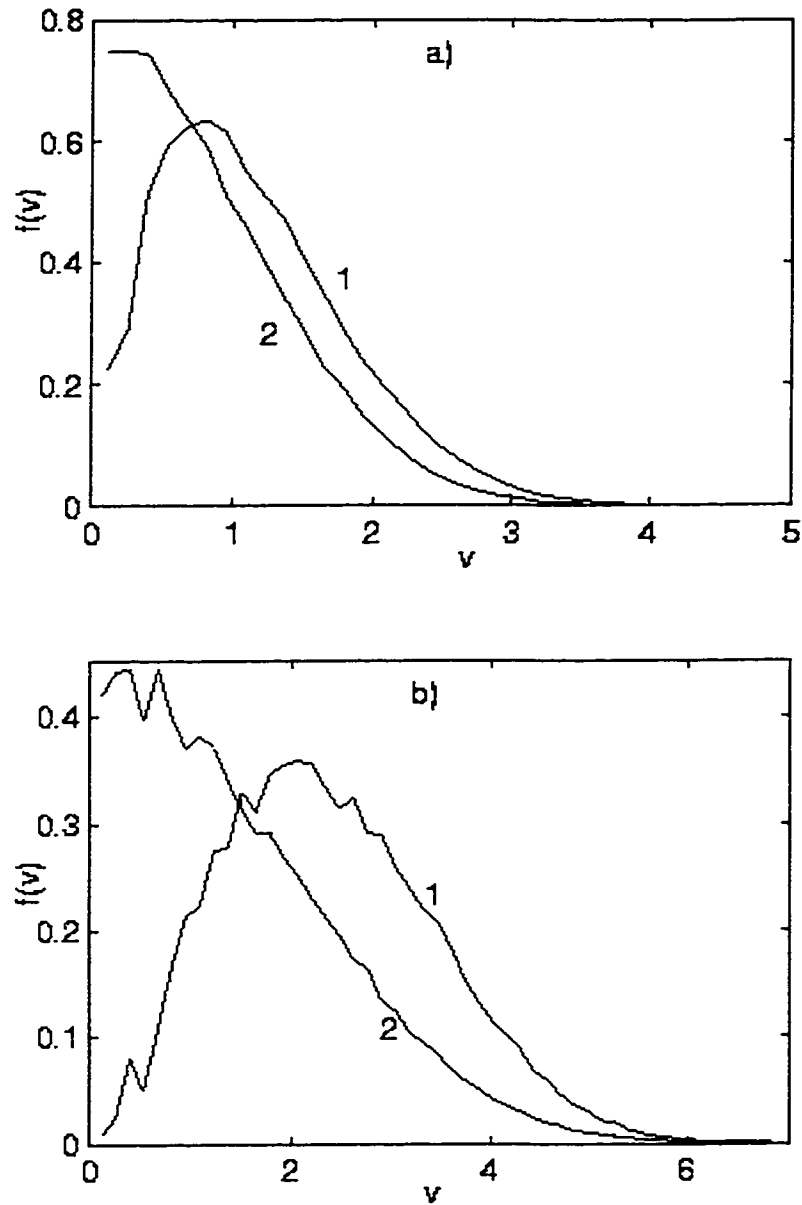


Figure 5.9: The electron distribution function at $t\omega_{pe} = 100$, for $v_{osc}/v_{th} = 0.17$ (graph a) and 12.0 (graph b). Again the curve 1 on each graph represents the function obtained with the modified cross section while curve 2 displays the classical form. It is apparent that very quickly after the laser is turned on, the modified algorithm shows a redistribution from the initial Maxwellian to a shifted state greatly depleting the low velocity electrons.

Chapter 6

Summary and Conclusions

In summary this study has considered the problem of the effects of an intense laser field on the scattering dynamics of electron-ion collisions in a plasma. Conventional plasma kinetic theory relies on the assumption of dominant small angle collisions. This is a fundamental theoretical assumption in the derivation of the Landau collision operator. This study has shown that the presence of an oscillating laser field, when introduced to the classical Rutherford scattering problem significantly alters the conventional model's predictions about IB heating and transport processes.

The first phase of this project is the construction of a program to simulate the trajectory of an electron incident on a stationary ion (modeling a collision in the centre-of-mass frame) in the presence of a linearly polarized, oscillating electric field. The model is constrained to a non-relativistic plasma where the magnitude of the electric field is large, but generally confined to the restriction that the quiver amplitude is less than the average inter-ion distance. This is to restrict the investigation to a binary collisional process. Further the ion's electric field was modified to be cut off at a Debye length to account for field screening effects normally present in a plasma, as well as at the deBroglie wavelength of

the electron to account for quantum diffraction effects. A fourth order symplectic integration algorithm is chosen to calculate the electron path based on the solution of the Hamilton equations of motion, because of its ability to preserve volume in phase space, reducing errors in energy and momentum conservation over the more popular Runge-Kutta technique.

With this model, we were able to resolve behaviors discussed by Fraiman *et al.* [12, 13] and Decker *et al.* [8]. We observe examples of large angle scattering induced by the laser field which included both scattering due to a classical trapping of the electron in the ion's field, and a correlation effect where the laser field forces the electron back towards the ion after the initial interaction multiple times hence multiplying the effect of the original scattering interaction. In effect this leads to chaotic scattering of the electron with extreme sensitivity to the phase of the laser field.

The next phase of the project set out to examine what implications such behavior would have on the macroscopic behavior of the laser plasma interaction. Specifically we looked at the differential transport (σ_{tr}) and effective (σ_{eff}) cross sections which characterized the loss of directed particle velocity and energy transfer respectively.

$$d\sigma_{tr} = \langle 1 - \cos \phi \rangle d^2\rho \quad (6.1)$$

$$d\sigma_{eff} = \frac{2}{v_{osc}^2} \langle v_{out}^2 - v_{in}^2 \rangle d^2\rho \quad (6.2)$$

Here the angular brackets indicate averaging over the initial phase of the laser field, while $d^2\rho$ identifies an element of area on the launch grid, a plane perpendicular to the initial launch velocity.

Predictions for the transport cross section in the case of a parallel launch (where the electron's initial velocity is parallel to the linearly polarized laser field vector) have been obtained using the Born approximation [9] which assumes small angle scattering. The simulations at such an orientation came within a fifty

percent deviation of the predictions proposed by Shvets and Fisch [9]. In this case there was a general increase in the transport cross section centered about v_{osc} compared to the prediction of the classical Rutherford cross section. The size of this deviation was shown to increase with intensity.

For orientations where the field was set perpendicular to the launch velocity, the transport cross section was shown to be generally smaller than the Rutherford curve.

Defining a large angle as $\pi/3$, we looked at the number of particles that contributed to the transport cross section that scattered through a large angle. The results showed that for velocities lower than v_{osc} the transport cross section is almost entirely made up of electrons that experience such behavior. The largest number of large angle scattering electrons was observed for the parallel launch alignment.

Functional dependence on the laser intensity and particle kinetic energy have been found for the overall transport cross section after averaging over all possible field alignments. This was examined for laser intensities from 10^{15} to $10^{17} W/cm^2$. This resulted in an expression for the transport cross section as a function of both initial drift velocity and laser intensity. The final curve looked like

$$\sigma_{tr} = \frac{\sigma_R}{1 + \Delta'(\Omega, v)}, \quad (6.3)$$

where

$$\Delta'(\Omega, v) = \alpha(\Omega) \left[\frac{v}{\Omega v_{osc}} \right]^{\beta(\Omega)-2} \frac{1}{\Omega^2} \left[\frac{v_{osc}^2}{v_{osc}^2 + v^2} \right], \quad (6.4)$$

and

$$\begin{aligned} \alpha(\Omega) &= 1.21e^{-9.89\Omega}, \\ \beta(\Omega) &= 2.00e^{-0.71\Omega^2 - 0.87\Omega}. \end{aligned} \quad (6.5)$$

Again σ_R is the classical Rutherford differential scattering cross section. The above fit reduces to the Rutherford case in the limit of low laser intensity. On the other hand, in the limit of increasing laser intensity, I , the cross section scales like $I^{-3/4}$. This proposed fit is consistent with our data to within a ten percent deviation.

The effective cross section was also calculated averaging over the different orientations of the laser field. For the case of the parallel launch (and orientations in that vicinity) we observed regions of negative energy gain. However when averaged over all orientations it was found that the net gain of kinetic energy of the electrons was always positive.

Low intensity models show that the IB heating rate is directly proportional to the effective collision frequency which is directly related to the effective cross section. The results of this study illustrate that for high intensities, there is a sharp drop in the value of the effective cross section for velocities below v_{osc} . There is also a small, but significant region where the effective cross section is greater than predicted by the low intensity result. It is proposed for the region $v < v_{osc}$ the effective cross section can be approximated by

$$\sigma_{eff} = \frac{8\sqrt{(2\pi)} 5}{3} \frac{1}{2(\alpha'(\Omega)v + v^2)}, \quad (6.6)$$

where

$$\alpha'(\Omega) = 0.0087 \Omega^{-14/3}. \quad (6.7)$$

Note that here I have used the notation α' to avoid confusion with Eq.(6.5) although in chapter four the term is denoted α . This form would indicate that for low velocities there is a $1/v$ dependence which translates into an effective collision frequency independent of drift velocity. This effect makes sense as, in this region, the oscillatory velocity would be the dominant influence on the collisions. With $\alpha'(\Omega)$ having the dependence on $\Omega^{-14/3}$ the collision frequency scales as $E^{-7/2}$.

A numerical integration of the effective cross section over a Maxwellian velocity distribution gives a prediction for the relative modification to the low field IB heating rate. Previous work has shown that as laser intensity increases, the heating rate will drop off from unity like $1/v_{osc}^3$. Our results show a region when temperature is low (on the order of 100 eV) where the heating rate will actually increase, possibly by as much as a factor of 2.5.

A particle simulation code was developed for the purpose of heating investigations in the presence of a linearly polarized laser field. A series of standard tests showed excellent conformation to Spitzer relaxation theory. Then it was shown how the scattering angle in such a code can be modified to incorporate the altered transport cross section in the presence of a high intensity laser. Thus heating at high frequencies can be examined incorporating elastic collisions without any assumptions about small angle collision dominance. Preliminary results of such investigations were presented.

In conclusion, it has been shown that the incorporation of a linearly polarized electric field into a classical Rutherford scattering model has dramatic consequences on the inverse bremsstrahlung heating and transport processes of a laser heated plasma. These effects are attributed to the chaotic scattering of the electrons and their influence on the transport and effective differential cross sections which govern the dissipation of directed particle velocity and IB energy transfer in the plasma respectively.

Bibliography

- [1] R.D. Jones and K. Lee, Phys. Fluids **25**,12 (1982)
- [2] A.B. Langdon, Phys. Rev. Lett. **44**, 575 (1980)
- [3] L. Boltzmann, Wein, Ber. **66**, 275 (1872)
- [4] L. Boltzmann, *Lectures on Gas Theory* (S. Brush transl.) Univ. California Press, Berkeley, 1964
- [5] L. Landau, Phys. Z. Sowj. Union. **10**, 154 (1936)
- [6] J. Dawson and C. Oberman, Phys. Fluids **5**, 517 (1962)
- [7] V. Silin, Sov. Phys. JETP **20**, 1510 (1965)
- [8] C.D. Decker, W.B. Mori, J.M. Dawson, and T. Katsouleas, Phys. Plasmas **1**, 4043 (1994)
- [9] G. Shvets and N.J. Fisch, Phys. Plasmas **4**, 428 (1997)
- [10] G.J. Pert, J. Phys. B **12**, 2756 (1979)
- [11] L. Wiesenfeld , Phys. Lett. A **144**, 467 (1990)
- [12] G.M. Fraiman, V.A. Mirinov, and A.A. Balakin, JETP **88**, 254 (1999)

- [13] G.M. Fraiman, V.A. Mirinov, and A.A. Balakin, *Phys. Rev. Lett.* **82**, 319 (1999)
- [14] J. Candy and W. Rozmus, *J. Comp. Phys.* **92**, 230 (1991)
- [15] J. Candy, *Nonlinear Dynamics of Particles in Wave Fields* MSc. Thesis, University of Alberta (1990)
- [16] Setsuo Ichimaru, *Statistical Plasma Physics*, **1**, 10 (Addison-Wesley, Don Mills Ontario, 1995)
- [17] L.D. Landau and E.M. Lifshitz *Mechanics 3ed. Course of Theoretical Physics 1*, pp49 (Pergamon Press, Toronto 1976)
- [18] T. Takizuka and H. Abe, *Comput. Phys.*, **25**, 205-219, 1977.
- [19] R.E. Kidder, in *Physics of High Energy Density*, edited by P. Caldirola and . Knoepfel (Academic, New York, 1971), pp.306, 1977.
- [20] S. Ma, R. Sydora and J. Dawson, *Comp. Phys. Comm.*, **77**, 190-206, 1993.
- [21] T. Johnston and J. Dawson, *Phys. Fluids* **16**, 722 (1973)
- [22] G. Pert, *Phys. Rev. E* **51**, 4778 (1995)
- [23] D. Vick, C. Capjack, V. Tikhonchuk and W. Rozmus, *Comments Plasma Phys. Controlled Fusion* **17**, 2, 87-98 (1996)
- [24] R. Faehl and N. Roderick, *Phys. Fluids* **21**, 793 (1978)
- [25] L. Schlessinger and J. Wright, *Phys. Rev A* **2**, 1934 (1979)
- [26] H. Gould and J. Tobochnik, *An Introduction to Computer Simulation Methods*, ed.2, (Addison-Wesley, Don Mills, 1996.)

- [27] R. Balescu, *Equilibrium and Nonequilibrium Statistical Mechanics* pp389 (John Wiley Sons, Toronto, 1975)
- [28] L. Spitzer, Jr., *Physics of Fully Ionized Gases*, Chap. 5, Interscience, New York, 1956
- [29] B. Trubnikov, *Reviews of Plasma Physics*, **1**, pp 105, Consultants Bureau, New York, 1965
- [30] R. Liboff, *Introduction to the Theory of Kinetic Equations*, pp 238-242, John Wiley and Sons, Toronto, 1969
- [31] I. Shkarofsky, T. Johnston, and M. Bachynshi, *The Particle Kinetics of Plasmas*, pp. 237, Addison-Wesley, Don Mills, 1966